Smartphone Jaw Tracking to Quantitatively Model Tooth Contact

by

Kieran Armstrong

A thesis submitted in partial fulfillment of the requirements for the degree of

Master of Science
in
Rehabilitation Science

Faculty of Rehabilitation Medicine

University of Alberta

Abstract

Surgical design and simulation uses Computer Aided Design (CAD)/Computer Aided Manufacturing (CAM) software to virtually plan for jaw reconstructive surgery. One part of the process includes the design of a dental prosthesis with the use of an articulator. The articulator is limited in its ability to recreate patient specific jaw motion.

This thesis presents a smartphone application to track jaw motion photometrically. The jaw motion was used to virtually recreate a bench-top model of a patient's occlusal kinematics and dynamics with biomechanical simulation.

The jaw tracking system uses a 3D printed tracking harness that interfaces with the surface of the maxillary and mandibular teeth. Each tracking harness has a dodecahedron attached to it with 12 binary fiducial markers mounted to its faces. A 3D model of each dodecahedron tracking harness was made to calculate the position of each binary fiducial marker's centre and corner points. The smartphone application detects the visible centre and corner points to solves a Perspective-n-Point (PnP) problem that estimates the mandible's pose relative to the maxilla.

The experimental results showed that the smartphone application was capable of achieving static position and orientation accuracy of $<$ 1mm and 5°. The smartphone application repeatably tracked jaw motion along an arced path with a dynamic accuracy $<$ 1mm up to 20mm of jaw opening. Past 20mm of opening, the reported dynamic accuracy was $<$ 2mm. The smartphone application was also capable of tracking a left, right, and protrusive excursion. The occlusal contact between the teeth was successfully recreated with biomechanical simulation kinematically (no occlusal forces) and dynamically (occlusal forces).

Preface

This thesis is an original work by Kieran Armstrong. No part of this thesis has been previously published.

Acknowledgements

I would like to express my gratitude to my supervisor, Dr. Daniel Aalto who was always there to encourage and support me through success and failure. His attitude towards solving problems gave me the confidence to never give up.

I would like to also express my deepest gratitude to my co-supervisors Dr. Martin Osswald and Dr. Jana Rieger for their guidance and suggestions during my academic journey. I was so lucky to have two experts at the top of their field to consult about the specifics of rehabilitation medicine and jaw reconstructive surgery. Additionally, I would like to thank Dr. Johan Wolfaardt and Dr. Gordon Wilkes for all of the foundational work they have done in medical reconstructive sciences. Their work encouraged me to apply my background in engineering to the field of reconstructive sciences, and I hope one day my work may be used to improve the treatment of patients diagnosed with head & neck cancer.

Thank you to the Institute for Reconstructive Science in Medicine (iRSM) for allowing me access to their state-of-the-art workspace, rapid prototyping tools, software, imaging equipment, and articulators. I always felt welcome and supported by all the staff. Thank you to Fari Karimi-Boushehri, and Lindsay McHutchion for always being willing to share their expert knowledge. A special thank you to Carolyn Kincade for her commitment to supporting my project. All of the 3D modelling, manufacturing, and design suggestions she made improved the quality of my work.

I would like to thank all of the people on the 6th floor of the Clinical Sciences Building. Noor Al-Zanoon, Rinde Johansson, Emilie Robertson, Jumana Joury, Dr. Gabriela Constantinescu, and Dylan Scott for reminding me to take a break for lunch and enjoy the journey.

Thank you to Dr. John Lloyd, Dr. Ian Stavness, Dr. Antonio Sanchez, and Dr. Amir Abdi at the University of British Columbia for all of their support to help resolve technical challenges related to computational biomechanics and computer graphics. Additionally, I would like to thank Gaspard Zoss at ETH Zurich and the Digital Humans Group at Disney Research for being so willing to discuss his research and provide suggestions on how to improve mine.

Finally, to my family thank you all for of you love and support. To my wife Zoe, thank you for believing in me and always being there to bring me up when I was down. Thank you to my parents Fraser and Judy Armstrong, Laurie Pelkie, and Clare Downing for your love, wisdom, and support.

Contents

1 Introduction **1**

1.1 Objective 2

1.2 Contributions 2

1.3 Thesis Organization 4

2 Literature Review **6**

2.1 Restoration of Chewing Function After Head & Neck Cancer 6

2.1.1 Impact on Quality of Life 7

2.1.2 Prosthetic Treatment after Jaw Reconstruction 7

2.1.3 Virtual and Occlusion Driven Jaw Reconstruction . . . 8

2.1.4 Surgical Procedure 11

2.2 Prosthesis Design 11

2.2.1 Mechanical Articulator 12

2.2.2 Virtual Articulator 14

2.3 Mandibular Motion Tracking 15

2.4 Low Cost Mandibluar Tracking Approaches 18

2.5 Virtual Simulation of Occlusal Interactions 20

2.6 Summary 22

3 Methods **23**

3.1 System Overview 23

3.2 Computer Vision Software Package Selection 24

3.3 iPhone® Application User Interface 27

3.4 Intra-oral Scanning 30
3.5 Tracking Harness Design 30
3.6 Dodecahedron Registration 34
3.7 AprilTag Detection 36
3.8 Tracking Harness Pose Estimation 39
3.9 Maximal Intercuspation Calibration Step 47
3.10 Benchtop Evaluation of Accuracy 47
3.10.1 Experiment 1 47
3.10.2 Experiment 2 50
3.10.3 Experiment 3 50
3.11 Virtual Simulation of Occlusal Interactions 51
3.11.1 Kinematic Simulation 52
3.11.2 Dynamic Simulation 53

4 Results **55**
4.1 Benchtop Evaluation of Accuracy 55
4.1.1 Experiment 1 56
4.1.2 Experiment 2 58
4.1.3 Experiment 3 61
4.2 Virtual Simulation of Occlusal Interactions 63
4.2.1 Kinematic Simulation 64
4.2.2 Dynamic Simulation 69

5 Discussion **71**
5.1 Benchtop Evaluation Accuracy 71
5.1.1 Experiment 1 71
5.1.2 Experiment 2 72
5.1.3 Experiment 3 73
5.1.4 Comparison to Other Tracking System 75
5.2 Virtual Simulation of Occlusal Interactions 77
5.2.1 Kinematic Simulation 77

5.2.2 Dynamic Simulation 78
5.3 Rehabilitation Applications 79
5.4 Limitations and Future Work 82

6 Conclusion **87**

References **90**

Appendix A Raw Pose and Angle Error Distribution Results **100**
A.1 Experiment 1 101
A.2 Experiment 2 110

Appendix B Relevant Head & Neck Anatomy **119**
B.1 Jaw 119
B.2 Hyoid 120
B.3 Mastication Muscles 121
B.3.1 Primary Mastication Muscles 121
B.3.2 Secondary Mastication Muscles 123
B.4 Temporomandibular Joint 123
B.5 Dentition 124
B.6 Occlusion 126
B.7 Mandibular Kinematics 128

Appendix C Position and Orientation Representation **131**
C.1 Description of Position 131
C.2 Orientation and Rotation 132
C.2.1 Rotation Matrices 132
C.2.2 Euler Angles 134
C.3 Homogeneous Transformations 135

List of Tables

3.1 Computer Vision Software Package Selection 26
3.2 AVCaptureSession Parameters 27

4.1 iPhone® Static Accuracy at a Camera Angle of 0° (Tripod) . 57
4.2 iPhone® Static Accuracy at a Camera Angle of 30° (Tripod) . 57
4.3 iPhone® Static Accuracy at a Camera Angle of 60° (Tripod) . 58
4.4 iPhone® Static Accuracy at a Camera Angle of 0° (Hand) . . 60
4.5 iPhone® Static Accuracy at a Camera Angle of 30° (Hand) . 60
4.6 iPhone® Static Accuracy at a Camera Angle of 60° (Hand) . 60
4.7 iPhone® Dynamic Tracking Accuracy 62

B.1 Posselt's Envelope of Motion Boarder Positions 130

List of Figures

2.1 Semi-Adjustable Articulator 13

3.1 Jaw Tracking System Overview 24
3.2 iPhone® Application Overview 28
3.3 AVCaputureSession Image Collection Process 29
3.4 Intra-oral Scan Registration 31
3.5 Tracking Harness Concepts 32
3.6 Tracking Harness Marker Concepts 33
3.7 Tracking Harness Final Design 34
3.8 Tracking Harness Registration 35
3.9 Dodecahedron Iterative Closest Point Registration 36
3.10 AprilTag Faces 37
3.11 AprilTag Example 38
3.12 Perspective and Point Diagram 40
3.13 Jaw Coordinate Frame 43
3.14 Dodecahedron Faces 44
3.15 Corresponding Image and Model Points 45
3.16 System Frame Transformations 46
3.17 Static Accuracy Error Definition 48
3.18 Static Accuracy Experimental Setup 50
3.19 Dynamic Accuracy Experimental Setup 52

4.1 iPhone® Application Static Accuracy (Tripod) 56
4.2 iPhone® Application Static Accuracy (Hand) 58
4.3 30 Cycles of 10mm Opening 61
4.4 30 Cycles of 20mm Opening 61

4.5 30 Cycles of 30mm Opening 61
4.6 30 Cycles of 40mm Opening 62
4.7 Excursion Displacements 64
4.8 Left Lateral Excursion Contacts 65
4.9 Right Lateral Excursion Contacts 66
4.10 Protrusive Excursion Contacts 67
4.11 Left Lateral Excursion Contacts with Dynamics Simulation . . 69

A.1 Pose Estimation Error Distribution at 80mm and 0° (tripod) . 101
A.2 Pose Estimation Error Distribution at 80mm and 30° (tripod) 102
A.3 Pose Estimation Error Distribution at 80mm and 60° (tripod) 103
A.4 Pose Estimation Error Distribution at 100mm and 0° (tripod). 104
A.5 Pose Estimation Error Distribution at 100mm and 30° (tripod) 105
A.6 Pose Estimation Error Distribution at 100mm and 60° (tripod) 106
A.7 Pose Estimation Error Distribution at 120mm and 0° (tripod) 107
A.8 Pose Estimation Error Distribution at 120mm and 30° (tripod) 108
A.9 Pose Estimation Error Distribution at 120mm and 60° (tripod) 109
A.10 Pose Estimation Error Distribution at 80mm and 0° (hand) . . 110
A.11 Pose Estimation Error Distribution at 80mm and 30° (hand) . 111
A.12 Pose Estimation Error Distribution at 80mm and 60° (hand) . 112
A.13 Pose Estimation Error Distribution at 100mm and 0° (hand) . 113
A.14 Pose Estimation Error Distribution at 100mm and 30° (hand) 114
A.15 Pose Estimation Error Distribution at 100mm and 60° (hand) 115
A.16 Pose Estimation Error Distribution at 120mm and 0° (hand) . 116
A.17 Pose Estimation Error Distribution at 120mm and 30° (hand) 117
A.18 Pose Estimation Error Distribution at 120mm and 60° (hand) 118

B.1 Jaw and Temporomandibular Joint Anatomy 120
B.2 Hyoid Bone Anatomy 120
B.3 Mastication Muscles 122
B.4 Occlusal View of Dentition 126
B.5 Molar Tooth Anatomy Situated in Connective Tissue 127
B.6 Posselt's Envelope of Motion Boarder Positions 129

C.1 Locating an Object's Position and Orientation 132
C.2 Compounding Frames 136

Glossary

AR Augmented Reality

ART Alberta Reconstructive Technique

CAD Computer Aided Design

CAM Computer Aided Manufacturing

CBCT Cone Beam Computer Tomography

CPU Central Processing Unit

CT Computer Tomography

DICOM Digital Imaging and Communications in Medicine

DoF Degrees of Freedom

FEM Finite Element Method

FPS Frames Per Second

GPU Graphics Processing Unit

ICP Intercuspal Position

JRR Jaw Relation Registration

P*n*P Perspective-n-Point

RGB Red Blue Green

STL Stereolithography

TMJ Temporomandibular Joint

UDP User Datagram Protocol

VISP Visual Servoing Platform

VR Virtual Reality

Chapter 1

Introduction

Surgical design and simulation is rapidly advancing as CAD and CAM technologies continue to improve. Restorative prosthodontics combines CAD/CAM and analog methods to model, design, and evaluate dental prosthesis function. Being well established, CAD/CAM software is inevitably replacing analog steps of the treatment process[1]–[3].

Rapid prototyping and 3D printing used in conjunction with virtual design software are important tools for building a dental prosthesis [4]. The benefits over traditional wax melting and moulding is design freedom, higher accuracy prototypes, and faster design cycles [5]. Even though designed virtually, the dental prosthesis often has to be 3D printed to evaluate function. This is because current CAD/CAM software used in restorative prosthodontics is limited in its inability to accurately recreate occlusal dynamics (tooth collisions) virtually [6], [7]. While some do consider occlusal dynamics, most are based on the mechanical constraints of the articulator, a physical device that holds the stone casts of oral impressions to reproduce collisions of the teeth during chewing. The articulator recreates a limited representation of patient specific jaw mechanics and may negatively impact the function of a patient's final dental prosthesis [8].

Biomechanical modelling, computer vision, and motion tracking is advancing the ability to recreate and analyse patient specific jaw motion and occlusal dynamics virtually [9]–[11]. But still, the articulator remains the current clinical standard to evaluate dental prosthesis prototype fit and function. There are many different reasons for recreating jaw motion and occlusal dynamics virtually, but in the context of digital prosthodontics two motivations are:

- to evaluate and predict dental prosthesis prototype function by accurately capturing a person's specific jaw motion [9], and
- to minimize the material used and time spent on manufacturing and designing a dental prosthesis prototype [12].

1.1 Objective

The objective of this thesis is to develop a mobile smartphone application to track mandibular motion and use it to virtually recreate a bench-top representation of a patient's occlusal kinematics and dynamics with biomechanical simulation.

1.2 Contributions

The contributions of this thesis include: (1) the creation of an all-in-one, widely available, and low cost optical jaw tracking mobile application solution, (2) the implementation of a real-time and virtual jaw tracking visualization interface over WiFi, (3) the development of a low cost, patient specific 3D printed jaw tracking harness concept, and (4) a demonstration of how the smartphone application can be used to drive the virtual simulation of occlusal contacts kinematically (without occlusal forces) and dynamically (with occlusal forces).

Smartphone Mandibular Motion Tracking

The smartphone application, invented in the context of this work, estimates the real-time position and orientation or 6 Degrees of Freedom (DoF) pose of the mandible and maxilla relative to a camera. More advanced motion capture systems do exist, however, a smartphone application does not require access to expensive equipment, specially trained operators, and mandible motion data can be collected anywhere. In recent years, advancements in Augmented Reality (AR) technology within smartphones has improved drastically and is enabling performance similar to commercial multi-capture systems [13]–[15].

Consequently, we implement a 6 DoF object tracking algorithm on the Apple® iPhone® Xs. The application works by detecting binary fiducial markers mounted to the tracking harness attached to the mandible and the maxilla, and then their poses are estimated with respect to (w.r.t.) the iPhone's® camera. The poses are estimated by solving a PnP problem that minimizes the distance between camera observed points on the tracking harness and their corresponding positions in the 3D world. Solving this problem in real-time, we are capable of achieving a sub-millimetre accuracy pose of the mandible w.r.t. the maxilla.

3D Printed Jaw Tracking Harness

We designed a 3D printed tracking harness for the jaw tracking application to detect and estimate the pose of the mandible w.r.t. the maxilla. The tracking harness can be customized to fit any person and can be easily adapted to work with a real restorative dentistry case.

Real-time Jaw Tracking Visualization

We added a real-time jaw tracking visualization module to the open source biomechanical modelling software platform ArtiSynth [16]. We implement a

User Datagram Protocol (UDP) over a local WiFi network to transmit tracking data from the iPhone® to the visualization module to update the 6 DoF pose of 3D maxilla and mandible tooth models.

Virtual Simulation of Occlusal Contact

1. **Kinematic Simulation:** We adapt an existing module in ArtiSynth to simulate occlusal contacts kinematically. Poses are recorded with the jaw tracking visualization module and used to update the pose of the mandible. Contact patterns are represented by tracing the points at which the teeth collide. Collisions are modelled by the contours that mesh interpenetration creates between the maxilla and mandible teeth.

2. **Dynamic Simulation:** We again use the ArtiSynth module to simulate occlusal contact, but only the initial and final pose of the mandible are used to drive the motion. The pose of the mandible is linearly interpolated between its initial and final position. Collisions are modelled with ArtiSynth collision detection, the maxilla teeth apply reactionary forces to the mandible teeth as the pose of the mandibular teeth is guided by the surface of the maxillary teeth with 6 DoF.

1.3 Thesis Organization

The following chapters provide a review of using surgical design and simulation for the restoration of chewing function after head and neck cancer, of methods used for dental prosthesis design, of jaw tracking methods, and virtual recreation of mandibular kinematics and dynamics. Chapter 3 presents the components of the smartphone application, the methods used to evaluate the smartphone's pose estimation accuracy, and a description of how we use the smartphone data to virtually recreate a benchtop patient's occlusal kinematics and dynamics. Chapter 4 presents the results of the smartphone's static and

dynamic pose estimation accuracy and the contact pattern results of a left, right, and protrusive excursion kinematically and dynamically. Chapter 5 discusses the results, compares the performance of the smartphone application to other jaw tracking systems, describes applications in rehabilitation, limitations, and directions for future work. Finally, Chapter 6 summarizes the thesis contributions and provides further concluding remarks. Appendix A provides the raw data of the smartphone pose estimation algorithm's static accuracy, Appendix B includes an overview of relevant head and neck anatomy, and Appendix C describes the mathematical notation used to represent position and orientation within this thesis.

Chapter 2

Literature Review

This chapter reviews literature related to current tools and methods used in surgical planning and large dental prosthesis design for jaw reconstruction patients. The review is divided into 5 sections. First, Section 2.1 reviews the restoration of chewing function after head and neck cancer, general jaw reconstructive surgery, and the specifics of occlusion driven jaw reconstruction. Second, Section 2.2 provides an overview of the mechanical articulator's history, the progression to the virtual articulator, and the limitation of recreating patient specific jaw motions with the articulator for analysis of dental prosthesis function. Third, Section 2.3 presents an examination of jaw tracking systems organized by their basic functional principle. Fourth, Section 2.4 reviews some low cost alternatives to more established jaw tracking systems. Finally, Section 2.5 reviews methods used to virtually model and simulation occlusal kinematics and dynamics.

2.1 Restoration of Chewing Function After Head & Neck Cancer

In this section, we discuss head and neck cancer, its impact on a person's oral function and quality of life, treatment with jaw reconstructive surgery, and review of a detailed jaw reconstructive surgery technique driven by occlusion.

2.1.1 Impact on Quality of Life

Head and neck cancers include cancers of the nasoppharynx, oropharynx, hypopharynx, larynx, oral cavity, sinuses, and the tongue. More than 4,300 Canadians will develop one of these cancers and 1,610 will die from it in 2020 [17]. The most common type of cancer is squamous cell carcinoma, which develops within the nose, mouth, and throat. The three main treatment options are radiation, surgery, and chemotherapy. In general, one or a combination of the treatment options are used based on the clinical scenario. The result can mean large resections of head and neck tissue and loss of chewing, swallowing, and speaking ability [18].

When tumours are removed from the head and neck region there can be devastating impacts on a person's quality of life. In addition to the losing varying degrees of physical function, psychological and nutritional factors are also impacted. Patients may have difficulty maintaining a healthy diet and they must adjust to their new physical appearance [19]. These are two changes to a person's life that can be terribly overwhelming to adjust to and are among the most challenging lifestyle changes to overcome [20].

2.1.2 Prosthetic Treatment after Jaw Reconstruction

Mirovascularized fibula free flap jaw reconstructive surgery was first introduced in the late 1980s and is a well established treatment for head and neck cancer patients [21], [22]. For patients that require the restoration of a functional dentition, vascularized bones provide better blood supply to surrounding bone with much less oral contamination compared to non-vascularized bones [23], [24]. Another advantage of the free fibula flap is that subcutaneous tissue containing elements of the skin can be left on the bone and integrated better with the surrounding tissue.

Finally, the length, shape, and structural properties of the fibular free flap allow surgeons to tailor reconstructions to the needs of an individual patient better than in the past [25].

With the solid foundation that the microvascularized fibula provided, more attention was put on the restoration of chewing function using a dental prosthesis [26]–[28]. From this surgical advancement, Brånemark *et al*. [29] proposed and demonstrated that titanium screws could be securely implanted into the vascularized fibula and support a dental prosthesis during mastication. He demonstrated that titanium could fuse with the bone in a process called osseointegration. This development created opportunities for patients that had undergone jaw reconstructive surgery to receive a stable and functional dental prosthesis supported by osseointegrated implants [26], [30].

Modern mirovascularized fibula free flap jaw reconstructive surgery now combines the use of advanced imaging technologies, virtual modelling software, and rapid manufacturing to virtually plan for surgery and create case specific surgical tools to carry out the plan within the operating room [31]. Virtual surgical planning or surgical design and simulation is now routinely used in fibula free flap jaw reconstruction. Surgical design and simulation has reduced time in the operating room, increased accuracy of procedures, and improved both the aesthetic and functional outcomes after treatment for patients [32], [33].

2.1.3 Virtual and Occlusion Driven Jaw Reconstruction

State-of-the-art jaw reconstruction aims to optimize bone placement by utilizing occlusal based planning and osseointegrated implants for dental rehabilitation [34]–[36]. Surgical design and simulation tools have made it possible to directly transfer a virtual jaw reconstruction plan to the operating room allowing the use of immediate osseointegrated implants within one procedure called

the Alberta Reconstructive Technique (ART) [37], [38]. To better understand the ART procedure and surgical design and simulation in general, we provide an overview that outlines the steps to image anatomical structure, perform a Jaw Relation Registration (JRR), carry out virtual surgery, and manufacture case specific tools used in the operating room to carry out the reconstruction.

Imaging Anatomical Structure

Imaging of the head and neck region is required to build a virtual model. Computer Tomography (CT) uses multiple x-ray images from different angles to reconstruct 3D volumetric images. CT machines move along the area being imaged to create image slices that usually range from 1-10 millimetres in thickness and then the image slices are stacked together to build a 3D model of anatomy using Stereolithography (STL) and Digital Imaging and Communications in Medicine (DICOM) software such as Geomagics (3D Systems, Rock Hill, SC), Slicer 3D (Harvard, Cambridge, MA), or OsiriX (Geneva, Switzeralnd). CT is well suited to image bone because it provides high spatial resolution and the high frequency x-rays are absorbed well by bone.

For head and neck anatomy, Cone Beam Computer Tomography (CBCT) is often used because it is relatively low cost and administers a relatively low dose of potentially harmful radiation [39] [40]. CBCT also has sub-millimetre accuracy making it well suited for imaging the complex anatomy of the head and neck region [41].

Jaw Relation Registration, Impressions, and Virtualization

Jaw Relation Registration (JRR), is the spatial relationship between the maxilla and the mandible. One method to record the JRR in an edentulous (no teeth) case, is to take impressions of the soft tissue of the maxillary and mandibular arches and make an occlusal rim to later record maximal Inter-

cuspal Position (ICP) (Appendix B.5) [42]. Next, a device called a facebow is used to record the distance and angle of the mandibular condyles to the lower middle incisor to estimate the occlusal plane (tooth contact plane) [43]. The impression of the maxillary and mandibular arch are then made into stone casts and mounted and physically aligned on a semi-adjustable articulator (Section 2.2).

To digitize the JRR, the maxillary and mandibular casts are laser scanned individually and then scanned again while mounted on the articulator. Using STL editing software such as Geomagics (3D Systems, Rock Hill, SC), the free casts can be aligned virtually with the correct spatial relationship of the mandible to the maxilla recorded on the articulator.

Virtual Surgery

At this point, a virtual model of the pre-operative anatomy (mandible, maxilla, hyoid, fibula, and dentition) has been obtained. First, virtual resection planes of the jaw are established based on clinical judgement [37] and a virtual resection is performed. In the resection area that impacts the teeth, a virtual occlusion is designed based on the dentition and then the position of osseointegrated implants is established based on the virtual occlusion. Finally, the fibula is virtually cut, positioned to support the osseointegrated implants, and fit to the dimensions of the planned deficit of the mandible.

3D Printed Surgical Tools

Once the virtual surgery is complete it is then used to reverse engineer the required surgical design tools for the procedure and are 3D printed into physical tools. The surgical tools include a resection cutting guide for the jaw and a fibula implant installation drilling guide. The surgical resection guide is used to reproduce the resection planes of the jaw in the operating room. The fibula

implant installation drilling guide includes a fibula cutting guide and transfer template of the cut fibula. The transfer template is used for positioning the cutting guide in the correct spatial relationship to the skull.

2.1.4 Surgical Procedure

In phase I of ART, the resection of the fibula is performed with the help of the resection cutting guide. The fibula is resected (retaining its vascular pedicles) and the implant drilling guide is used to position the osseointegrated dental implant fixtures. Next, the fibula is cut with the cutting guide, and abutments are connected to the fixtures along with the occlusal transfer template to align the bony segments of the fibula. The fibula along with the transfer template is positioned in the facial resection area and then placed in the correct spatial relationship. This is done with the help of the implants and the occlusal transfer jig. Once positioned correctly, the template and abutments are disconnected, the heads of the implants capped, and skin flap from the fibular flap is used to cover the reconstruction.

Phase II of ART begins once the wound has healed and the implants are osseointegrated with the fibula graft. Finally, at phase II the dental implants in the fibular fixture are exposed, healing abutments are attached, and the process of fabricating a dental prosthesis is commenced.

2.2 Prosthesis Design

The key to a successful jaw reconstruction is having a fully functional dental prosthesis [26]. As mentioned in the previous section, surgical design and simulation has been successful at restoring most of a patient's chewing function with advanced methods such as occlusal driven jaw reconstruction. In most cases, the articulator is the standard device used to assess and model the chewing function of small and large dental restorations [44]. The articulator

attempts to reproduce natural sliding and grinding motions of the teeth to provide feedback to designers about what teeth are colliding too much or too little during these dynamic movements. This feedback is used to adjust the position of teeth until the contact between the upper and lower teeth is optimized for the best chewing performance.

In this section, we review the history of the mechanical articulator, the progression toward the virtual articulator, and the limitations associated with both in the context of prosthesis design for occlusal driven jaw reconstruction.

2.2.1 Mechanical Articulator

The first developments of the articulator date back to 1756. Phillip Pfaff created a plaster extension on the distal portion of a mandibular cast to spatially relate a maxillary cast to a mandibular cast [45]. The only function of this articulator was to record the maximal ICP. Since then, the articulator has become the most commonly used device in medicine and dentistry to recreate tooth contacts or occlusal dynamics [46], [47].

The understanding of jaw physiology and movement has increased significantly focusing on accurately reproducing mandibular movement [46]. To achieve this, engineers and dental scientists focused on developing devices to measure the mandibular condylar angle, improve cast mounting techniques, and study the natural path that the mandibular condyles and lower midincisor take during different mandibular motions [48]. Different articulators have been designed to replicate the complex motion of the mandible. According to Weinberg *et al.* [49], articulators can be classified into four categories:

- **Arbitrary (Simple-Hinge):** Allows for opening and closing of the mouth about a transverse axis that passes through each condyle.
- **Positional (Fixed Condylar Path):** Allows for opening, closing, and

protrusive movements along the horizontal condylar path.

- **Semi-Adjustable:** Allows for opening, closing, inclination of condylar path, Bennett angle, and incisal path (Figure 2.1).

- **Fully-Adjustable:** Allows for opening, closing, the inclination of the condylar path, Bennett angle, Fischer angle, incisal path, and inter-condylar distance.

The semi-adjustable and fully-adjustable articulators can represent mandibular motion well enough to be used for large dental prosthesis restorations. That being said, the fully-adjustable articulator is not widely accepted due to is the complex mounting procedure and high cost. The semi-adjustable articulator has a less complex mounting procedure, is cheaper, and is partially able to reproduce occlusal morphology making it the instrument of choice for most dental restorations [50].

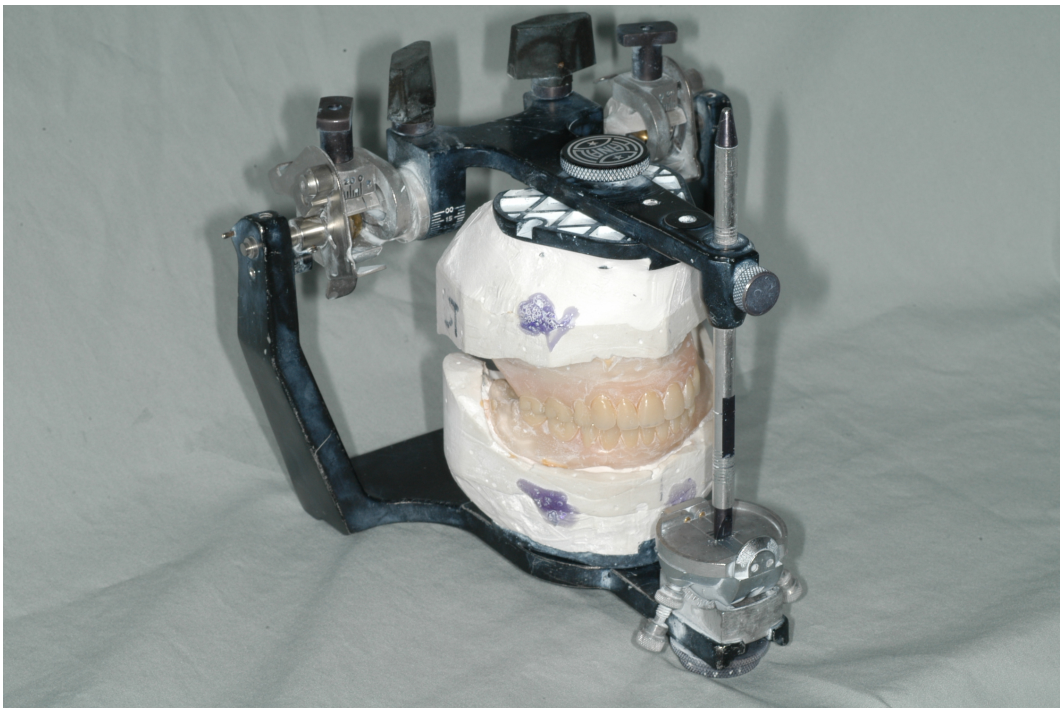

Figure 2.1: Semi-adjustable articulator.

Semi-adjustable articulators are used differently by clinicians and specific use for restoration varies based on opinion and application [51]. However, it is safe to say most professionals in the field of dentistry would agree that the semi-adjustable articulator is limited in its ability to reproduce Temporomandibular Joint (TMJ) kinematics and that the TMJ plays a prominent role in mastication and functional occlusion [52].

2.2.2 Virtual Articulator

With the push to virtualize the dental prosthesis design procedure, many pieces of research have put forth solutions for virtually modelling semi-adjustable articulator kinematics [12], [53], [54]. Currently, there are two main types of virtual articulators, completely adjustable and mathematically simulated articulators [55].

Both the completely adjustable and mathematically simulated virtual articulators require a registration step that typically consists of physically capturing and then virtualizing the spatial relationship between the mandible and maxilla. This is often either done by laser scanning of dental casts mounted to a semi-adjustable articulator or with an intra-oral scanner that uses optical imaging to directly create 3D models of the maxilla and mandible teeth [56].

The completely adjustable articulator records and reproduces the exact movement paths of the mandible with jaw tracking (Section 2.3) [12]. Whereas, mathematically simulated virtual articulators calculate jaw motion based on the programmable parameters of the mechanical articulator. Once the motion is defined the movements of the mandible are animated and the points of occlusion are visualized on a computer [56].

The clear benefit of completely adjustable articulators over mathematically simulated ones is that they capture patient specific jaw motion. This can help provide clinicians individualized information about a patient that could

influence the options they have for treatment [55]. Additionally, in the virtual environment, it is possible to calculate magnitude, direction, and area of applied loads. This may provide insight for things such as dental prosthesis strength, potential failure points, forces on the bone-implant interface, and predictions about how long the prosthesis is expected to last [9], [57], [58].

2.3 Mandibular Motion Tracking

Many different methods have been used to track the motion of the mandible the skull. The motivation for tracking the mandible spans several different fields that include studying chewing, speech, swallowing, and human biomechanics. In this section, we review mandibular motion tracking techniques from a virtual prosthesis design perspective.

Photometric

Photometric methods use a single camera or number of cameras to track the position of markers fixed to the face or jaw. Luce *et al*. [59] first introduced the photometric method in 1889. They used one camera and a stationary photometric plate. Bright silver beads were fastened to a wood pin at the lower middle incisor and other beads near the condyles. During lateral excursions, Luce *et al*. took photos continuously and the light reflected from the beads would record a line on a photometric plate. This method has developed over time and several authors have employed variations of the types of markers and their reflective nature. For example, de Rudd *et al*. [60] used indicator spheres coated in fluorescent paints and photographing was carried out in a dark room with the use of ultraviolet radiation to produce fluorescence.

With the improvement of camera and computer technology, the photometric method has been able to improve drastically. Cameras such as Kinect® (Windows, Microsoft Corp., Bellevue, Washington, USA), Optotrak® Certus

(NDI Inc., Canada), GoPro® (San Mateo, California, USA) all have been used to accurately track jaw motion. Abdi *et al*. [61] demonstrated that high accuracy of occlusal contact can be obtained with a precise registration method between virtual tooth models and their real counterpart. The system uses the geometric principle, that for any given infinite tetrahedral there only exists one spatial position for a sphere to rest. Using physics based visualization software ArtiSynth (University of British Columbia, Vancouver, British Columbia, Canada), Abdi demonstrated that with his registration method and the Optotrack system he was able to achieve a reported 3D accuracy of $100um$.

Tanaka *et al*. [62], demonstrates the photometric technique with the Kinect® V1 camera which was used to collect Red Blue Green (RGB) and depth data to obtain 28 virtual markers on the facial profile to estimate mandible position with no physical markers on the face. This demonstrates the advancement of photometric methods as camera and computer vision technology is now capable of estimating the 3D position of a point with a depth dimension. Within a clinical context, markerless tracking is valuable because it does not inhibit the occlusal surface making it a viable solution for virtual prosthesis design. The limitation of photometric techniques is that frame processing is computationally expensive, requires camera calibration, and error increases when tracking a small number of points.

Optoelectronic

Optoelectronic systems consist of a light emitting diode (LED), a position sensor within a camera, and a computer with a camera view interface. Generally, two cameras are placed perpendicular to each other with one capturing frontal plane motion and the other capturing sagittal plane motion. LED markers are positioned on the skull and the teeth. The upper skull markers define the head frame coordinate system and relative motions of the mandible can

be calculated. Optoelectronic systems (JAWS-3D, mac reflex) are one of the preferred methods to study mandibular motion due to their high accuracy and improving user interfaces for data collection [63].

Ultrasonic

Relatively new, ultrasonic systems utilize ultrasonic collectors attached to a head coordinate frame and emitters attached to the mandible (JMA from Zebris GmbH). The JMA system determines the mandibles relative position by calculating the time for ultrasonic pulses sent from emitters to reach collectors. The 3D mandibular motion is then recreated by aligning a triangular plane between the condyle points and the base pose of the JMA system. This triangular plane is then is used to set the target position of the mandible. The reported accuracy of this system is sub-millimeter [64] [24].

Magnetometry

Magnetometry works by utilizing changes within an electromagnetic field that occur when a small magnet moves relative to a sensor to track mandibular motion. An advantage of magnetometry systems is that they do not require line of sight from a camera sensor. They have been used for many years to track jaw motion because they are self-calibrating, easy to use, do not interfere with mandibular motion, and reasonably accurate [65] [66] [67]. Using magnetometry to record mandibular motion can be problematic because the sensors may fall off during the recording process.

Roentgenographic

Roentgenographic methods synchronize the excitation of radiation with a camera shutter to capture long exposure images. The radiation imaging is only active when the camera shutter is open to reduce radiation exposure to the head and neck region. Chen *et al.* [68] propose a method based on single plane

fluoroscopy image and low radiation CBCT capable of accuracy of 1.0 ± 1.4mm for all translation and $0.2 \pm 0.7^{\circ}$ for all rotations. The method was validated with roentgenographic analysis at static positions and during open-close movements. The advantage of the roentgenographic method is that it does not rely on transoral devices, can accurately capture *in-vivo* mandibular motion, and may be useful to assess patient with missing or unstable teeth. The disadvantage is, however low dose, radiation may be harmful and thus should be taken into careful consideration [69].

2.4 Low Cost Mandibluar Tracking Approaches

Low cost alternatives to commercial tracking systems have always been an area of research in AR, robotic, and computer vision fields. Recently these methods have been translated to dentistry and medicine because of their low cost, usability, and portability. Additionally, with the continued improvement of computing power, the speed of optical tracking algorithms, object detection, and 6 DoF pose estimation, the development of low cost mandibular tracking systems has become realistic.

Authors have used planar fiducial markers that can be individually detected and their pose estimated within the images that a camera captures in real-time. Planar fiducial markers were first used in AR and robotic applications[70]–[73] and a number of well established libraries exist [74], [75]. Most of the libraries output the position of each detected marker's corners from which their 6 DoF pose can then solved with PnP algorithm's making use of the projection perspective camera model [76].

Some systems fix planar fiducial markers with a custom brace fabricated or glued directly to the teeth. These systems demonstrate that sub-millimetre mandibular tracking is attainable and can compete with commercial tracking systems [10], [77], [78]. The disadvantage of these systems is that some of the

braces presented inhibit the natural collisions between the teeth, require more than one camera, and an offline calibration for each camera. Additionally, some of the data required for tracking involves CBCT, facial scanners, specialized alignment schemes, and custom designed micro-electronics.

The other approach for using fixed planar fiducial markers is to reconstruct the known 3D geometry of an object and estimate its pose relative to a camera(s). Notably, Zoss *et al.* [15] use a 3D printed cube with square fiducial markers on each face oriented such that one camera can see 2-3 fiducial markers on the cube. With two cubes fixed to the upper teeth and lower teeth, 32 markers can be synchronized between cameras and their average pose is calculated to achieve higher precision and robustness.

Other mandibular motion tracking systems do not use markers, and instead to track the pose of the mandible measure multiple points on the face with a depth camera or use machine learning approaches. Depth cameras work by calculating the time to reflect infrared light sent from an emitter to a sensor [62]. Machine learning approaches work by training a non-linear mapping from points on the skin to the jaw pose of several people [79]. The other approach is to fit transformations of the teeth with a 3D non-linear model that parameterizes the full range of motion of the TMJ [80].

Markerless tracking of mandible motion is valuable for evaluating tooth collisions because nothing inhibits natural tooth interactions, it does not rely on a person having teeth, and no specialized equipment is required increasing its accessibility. The challenges that these systems face are: they require the completeness of large amounts of training data, which may not always be available, they rely on deformations of the skin making it difficult to detect small mandible movements, and they require high frame rates and depth enabled camera hardware.

2.5 Virtual Simulation of Occlusal Interactions

The virtual simulation of occlusal interactions can either be done kinematically or dynamically. Both methods do require imaging and registration of the spatial relationship between the maxilla and the mandible. In this section, we review how occlusal interactions can be modelled kinematically and dynamically.

Kinematic Simulation

Kinematic based methods for modelling and simulation of occlusal contact are dependent on the 3D shape of virtualized tooth models and a target trajectory that is either mathematically derived from a mechanical articulator or mandibular motion tracking system [53] [81]. If a jaw tracking system is not used the casts must be virtualized in different poses to calculate dynamic movements between these positions. Contact is simulated between the upper and lower teeth visually by inspecting points that the meshes of the virtual models interpenetrate or with processing software that can calculate contour contacts between the two models.

Dynamic Simulation

Dynamic based methods include the mass and inertial properties of virtualized tooth models or in other words their rigid body dynamics. Typically, the properties of a rigid body can be calculated in a dynamic simulation based on its surface geometry assuming a constant density. Some sources estimate the mass and inertia parameters of anatomy and are freely available [82]. The advantage of rigid body based methods for modelling occlusal dynamics is that forces can be calculated and applied based on mesh interpenetration. This helps to more closely represent the dynamics of occlusion and tooth interactions when compared to kinematic simulations.

Several multi-body physics software platforms are capable of simulating the interactions of multiple rigid bodies (ex. SolidWorks Rock Hill, South Carolina, USA, COMSOL Multiphyiscs® Stockholm, Sweden, OpenSim, Palo Alto, California, USA, ArtiSynth Vancouver, BC, Canada) of which two have been increasingly visible to the biomedical community - OpenSim and ArtiSynth. Collision handling in ArtiSynth works by finding the interpenetration between geometries, determining the nearest point of the opposing geometry, and then calculating respective reaction forces based on the mass, inertia, and external forces applied on each body.

Stavness *et al.* [11], demonstrated the feasibility of combining intra-oral scanning and rigid body occlusal dynamic simulation with ArtiSynth. A mechanical articulator and its casts were laser scanned at a maximal ICP initial pose and left lateral, right lateral, and protrusive final positions. The pose of a virtual mandibular dental cast was calculated at its initial and final positions relative to the virtual maxillary dental cast. In the simulation, the mandibular dental cast was then translated in a straight line from its initial pose to each final pose. During the translation, contact between the maxillary and mandibular casts was calculated, rotating and translating the mandibular cast as it would in the real world. One version of the simulation incorporated the condyle programming angles that exist on an articulator and one that did not. There was a slight deviation between the trajectories and ArtiSynth was able to accurately reported contact points when compared to its physical counterpart.

The other notable method for dynamic simulation of occlusal interactions is the Finite Element Method (FEM). The FEM was originally developed for structural and mechanical analysis of engineered materials opposed to biological tissue. Commercial software packages such as ANSYS® (Canonsburg, PA, USA) and COMSOL Multiphyiscs® (Stockholm, Sweden) are very slow and

not ideal for modelling dynamic simulations in real-time. However, Benazzi *et al*. [83], presented a method for occlusal contact detection between a pair of upper and lower pre-molars and the simulation results showed the stress pattern on teeth with extremely high accuracy. The FEM is of extreme interest within the restorative dentistry community because they can model and simulate forces and stress throughout the teeth and onto supporting structures such as implants. This is very valuable because more accurate predictions on the life of dental prostheses can be made by performing cycle loading to evaluate failure and fatigue. However, the computational cost of the FEM is extremely high and is not feasible for real-time dynamic simulation.

2.6 Summary

Based on this literature review, there is evidence to support the positive outcomes of using surgical design and simulation techniques for facial and jaw reconstructive surgery. Virtually based and occlusion driven jaw reconstruction is the next step for optimizing chewing function of a dental prosthesis. However, the current tools used for dental prosthesis design and assessment are limited in their ability to accurately recreate patient specific jaw motion. Accessibility to jaw tracking technology and virtual simulation of occlusal interactions provides an opportunity to be combined for patient specific dental prosthesis design. Therefore, we present the development of a mobile smartphone application for mandibular jaw tracking to recreate patient specific occlusal kinematics and dynamics within a virtual environment.

Chapter 3

Methods

3.1 System Overview

The proposed tracking system in this thesis requires a virtual 3D model of the upper and lower teeth and an iPhone® . Due to the computational demands of this computer vision problem, it is recommended to use an iPhone® 8 or later. In this work, an Apple iPhone® Xs with a 64-bit Central Processing Unit (CPU) is used to track mandibular motion. On the back, it has a 12MP camera with a wide-angle lens ($f/1.8$ aperture) and a telephoto lens ($f/2.4$ aperture). On the front it has a 7MP TrueDepth® ($f/2.2$) camera. The iPhone® Xs wide-angle and telephoto camera on the back is capable of capturing 720p, 1080i, and 4K video at 24, 30, and 60 Frames Per Second (FPS), while the TrueDepth® camera on the front is limited to 1080i at 30 FPS.

The second component of the jaw tracking system is a 3D model of the teeth or oral anatomy. These models can be acquired with an intra-oral scanner or with tradition wax impression virtualized with a laser scanner. To track the rotation and position of the teeth relative to the iPhone® camera a person specific tracking harness can be designed in CAD/CAM software to match the geometry of the upper and lower teeth. Each tracking harness has a dodecahedron mounted to it in any position that must not result in a collision between the maxilla and mandible dodecahedrons at maximal ICP. Once the

model has been designed to fit with the teeth virtually, it is 3D printed and 12 unique binary fiducial markers are mounted to each face of the maxilla and mandible dodecahedrons.

The final component of the jaw tracking system is the iPhone® application we have developed. We implement image processing software in the application to detect the unique binary fiducial markers from real-time camera images. The software then matches the corners of each tag with the 3D model of the tracking harness to compute the observed pose of the tracking harnesses relative to where the camera is in 3D space.

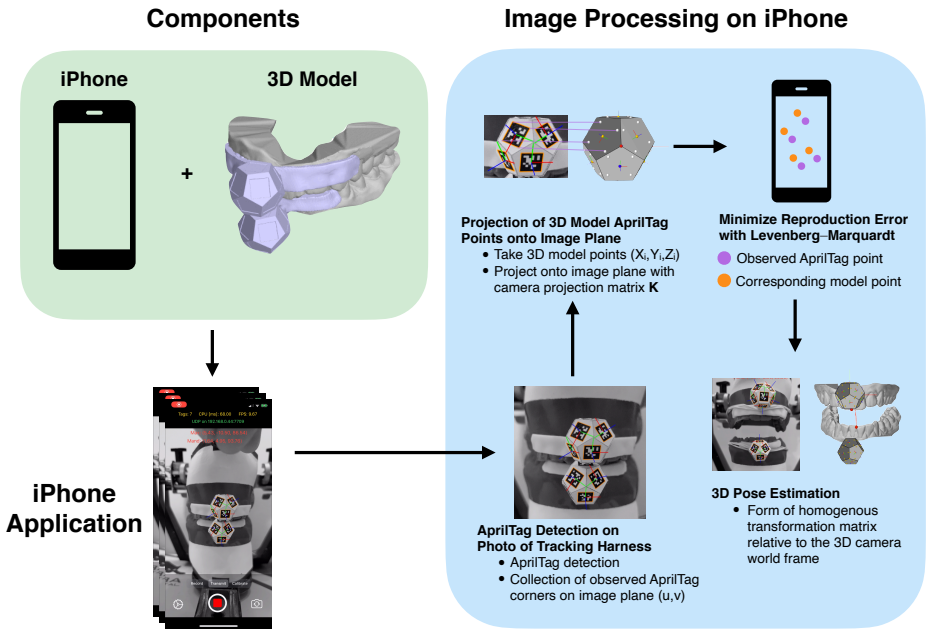

Figure 3.1: Jaw tracking system overview.

3.2 Computer Vision Software Package Selection

Several computer vision software packages were considered to implement the algorithms required to track the 6 DoF position and orientation of the jaw.

To determine which software package to select a list of requirements was put together and evaluated with a weighted decision method [84]. Five requirements and respective weights were identified to evaluate potential software libraries to use for the technical implementation of jaw tracking. Each library was rated with a score (S) from 0-10 and a value (V) calculated by multiplying the assigned decision weight.

The justification for the assigned weights and scores in Table 3.1 are listed below:

1. **Cross-platform (0.15):** With the future of this development in mind, it would be ideal if the core software can be easily transferred to run on other mobile phones or personal computers. A score of 10 indicates that this library is highly likely to work with almost any modern mobile phone or computer.

2. **Well established (0.2):** Several open source computer vision libraries are continually being updated by collaborators. To avoid issues with software stability, a well maintained and established library is key for development. A score of 10 indicates that this library is either commercial or well maintained by a group of developers instead of widespread collaborators.

3. **Modular (0.4):** The highest weighted requirement because it is important to have a library that can support many computer vision operations such as image processing, segmentation, 3D mathematics, optimization schemes, and photometric tracking. A score of 10 indicates that this library has all of the listed operations and more.

4. **Documentation (0.15):** A software library with poor documentation makes it extremely difficult to use for development. A score of 10 indi-

cates that this library has exceptionally well maintained documentation, demo code, tutorials, and examples.

5. **Support (0.15)** With good documentation there must be support from the core developers of the library to help solve implementation problems and provide clarification. A score of 10 indicates that there a great online support presence and users are encouraged to reach out for help.

			Apple		**VISP**		**OpenCV**		**OpenTL**	
Requirement		**Weight**	**S**	**V**	**S**	**V**	**S**	**V**	**S**	**V**
1	Cross-platform	0.15	0	0	10	1.5	10	1.5	10	1.5
2	Well established	0.2	10	2	10	2	10	2	7	1.4
3	Modular	0.4	6	2.4	8	3.2	7	2.8	2	0.8
4	Documentation	0.15	10	1.5	10	1.5	8	1.2	5	1
5	Support	0.15	8	1.2	9	1.35	8	1.2	5	0.75
Total value				7.1		**9.55**		8.7		5.45

Table 3.1: Computer vision software package comparison and ranking.

From the results in Table 3.1, Visual Servoing Platform (VISP) scored first with a total value of 9.55. VISP is a modular c++ cross-platform library that allows for prototyping and developing applications using visual tracking and servoing techniques that are up-to-date with current computer vision research [85]. It provides a set of visual features that can be tracked using real-time image processing and computer vision algorithms. It integrates with OpenCV, one of the more popular open source image processing and computer vision software packages [86]. This is ideal because, within VISP, OpenCV modules can be used if a feature does not exist without cumbersome setup.

Apple computer vision and image processing toolkits (ARKit, SceneKit, Vision, CoreImage, MLKit) have very similar tools when compared to VISP. Apple's tools are the obvious choice for simple tracking and AR applications because the libraries are optimized for Apple hardware. However, it is propri-

etary software and the inner workings of the algorithms are not public making it difficult to customize the software for specific computer vision applications.

OpenTL was an interesting competitor because it is specifically dedicated to tracking problems. However, it is very new compared to VISP and seems to be not robust enough to develop the proposed mandibular tracking system.

3.3 iPhone® Application User Interface

The iPhone® application we designed provides a user interface for the user to collect tracking data of the mandible and maxilla in real-time. There are two main views (Figure 3.2), the first is the camera view and the second is the settings view. In this section, we describe the high level software implementation of each view and its functionality.

Camera View

The camera view consists of a UIImageView to display images captured by the camera with Apples AVFoundation framework. Within AVFoundation, a AVCaptureSession can be configured to include a capture device, image resolution, pixel buffer format, capture speed, and focus mode. In this work, the following AVCaptureSession parameters in Table 3.2 can be programmed:

Table 3.2: Default configuration for AVCaptureSession.

Capture Device	.builtInDualCamera		.builtInTrueDepth
Image Resolution	.hd1280x720	.hd1920x1080	.hd4K3840x2160
Pixel Buffer Format	.kCVPixelFormatType_32BGRA		
Capture Speed	30 FPS	60 FPS	
Focus Mode	Manual	Auto	

Please refer to Apples most recent documentation for configuring an AVCaputreSession with AVFoundation (`https://developer.apple.com/documentation/`)

Once the capture session is configured, an event is fired every time that AVCaptureSession receives an image from the camera in the specified pixel buffer format (Table 3.2). This buffer is converted into a UIImage and sent to

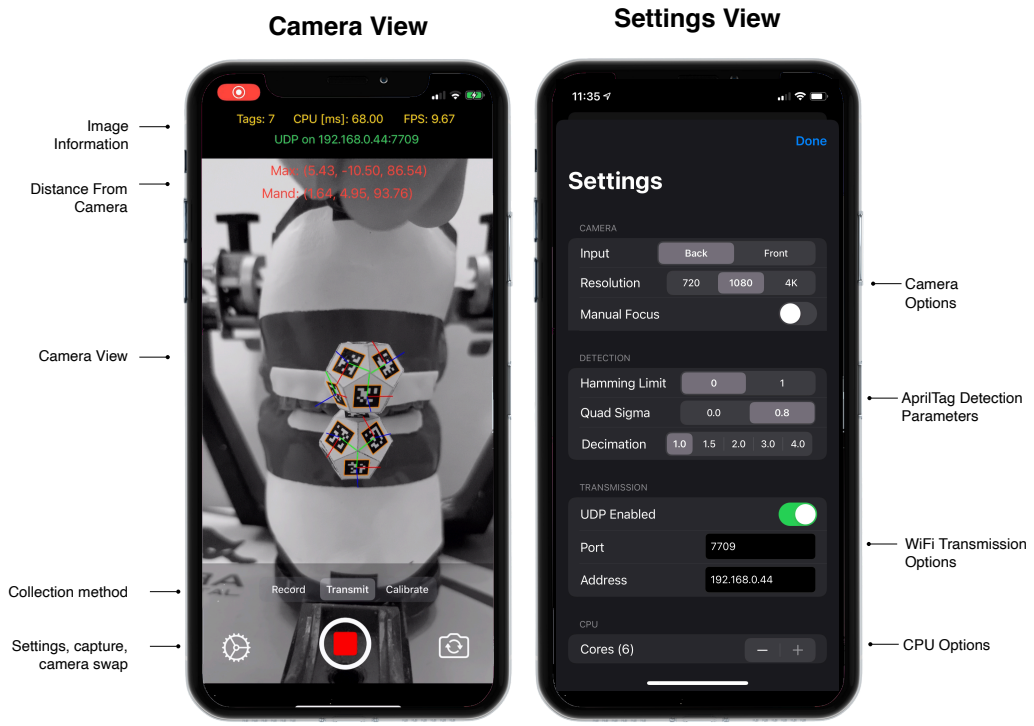

Figure 3.2: Overview of the iPhone® application camera and settings view. The camera view includes: image information, estimated distance of the maxilla and mandible dodecahedrons to the iPhone's® camera, and controls for recording and transmission. The settings view includes options to: adjust camera image capture resolution, AprilTag detection parameters, UDP options, and CPU utilization.

VISP for image processing and pose estimation. Once complete, the detected AprilTags are rendered on the image and returned to the UIImageView for display (Figure 3.3).

The camera view also provides debugging information about the number of AprilTags detected, the time to compute the pose of the dodecahedron on each tracking harness, and the current FPS. Additionally, the UDP connection label turns green when the iPhone® is connected to a computer for data transmission. The label is only green when connected to a computer and is transmitting data to a user specified IP address and port.

The iPhone® application has two capture modes, record and transmit. The record button will save jaw tracking information locally to the iPhone®

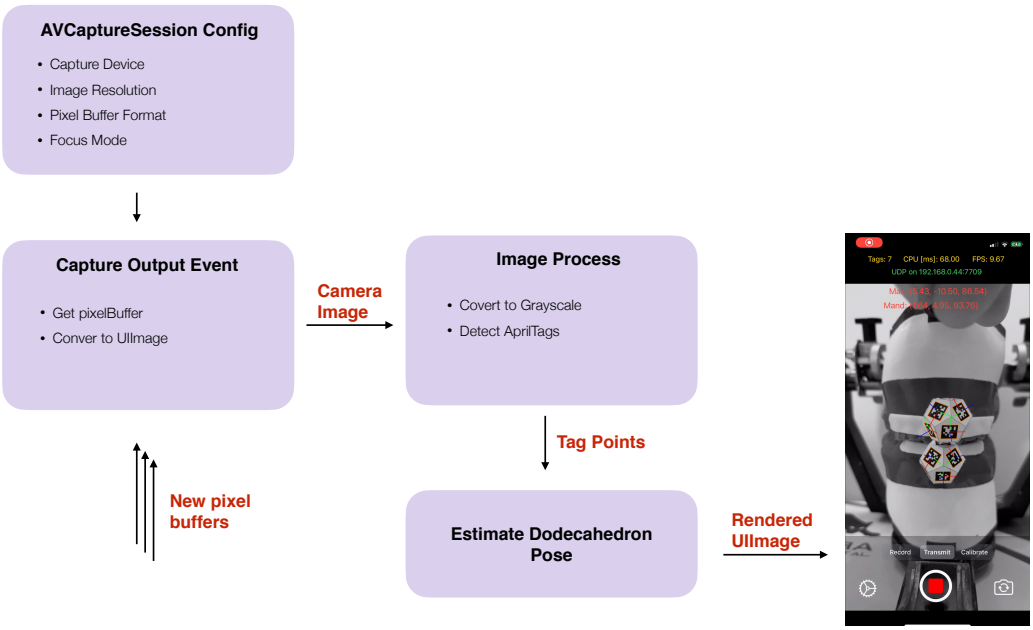

Figure 3.3: AVCaputureSession image collection process. First, the AVCaptureSession is configured with the parameters in Table 3.2, captured images trigger an event, the image is sent for image processing, the tag points are sent to VISP for pose estimation, the UIImage is rendered onto the iPhone® screen, and a new pixel buffer is captured by the iPhone® camera to repeat the process.

within the Files application. When data capture ends, the user is prompted to enter a name for the data file and it will save the named data file in an automatically generated folder specific to the tracking application in Files. The transmit mode sends data over a local WiFi network to a personal computer that is running a UDP server. The technically inclined user is free to program their own server to post-process data or can use that real-time mandibular motion visualization software built for this thesis in ArtiSynth.

Settings View

The settings view allows the user to adjust camera parameters, AprilTag detection parameters, WiFi transmission settings, and the number of CPU cores that then iPhone® can allocate to VISP. The camera input can be changed from the front or back, the resolution set to 720p, 1080i, or 4K, and the cam-

era focus can be set to manual or auto. In manual mode, a slider appears to adjust the focal point of the lens.

The AprilTag detection parameters include a hamming limit, quad sigma value, and decimation value. The hamming limit is a binary detection parameter for finding fiducial tags, the quad sigma value is an adjustment parameter for noisy camera data, and the decimation value is used to tune the accuracy of AprilTag detection. These parameters are discussed with further detail in Section 3.7.

3.4 Intra-oral Scanning

One 3D scan of the mandibular teeth and one of the maxillary teeth were obtained using an iTero® Element 2 intra-oral scanner (Align Technology Inc., Or-Yehuda, Israel) at a resolution of 34.20 pts/mm^2. A 3rd and separate registration scan of the buccal surface of the mandibular and maxillary teeth was then completed to align the virtual maxillary and mandibular teeth to the scan of the teeth in their maximal ICP. Each 3D mesh geometry was then exported to STL format and used to design the tracking harnesses in the STL editing software Geomagics (3D Systems, Rock Hill, SC). The design of the tracking harness is not limited to Geomagics and can be completed in any STL editing software.

3.5 Tracking Harness Design

The design process was based on trial, error, inspiration from previous authors [13], [15], and guidance from an experienced dental technologist. With this in mind, the mounting method and marker shape was guided by the following design constraints:

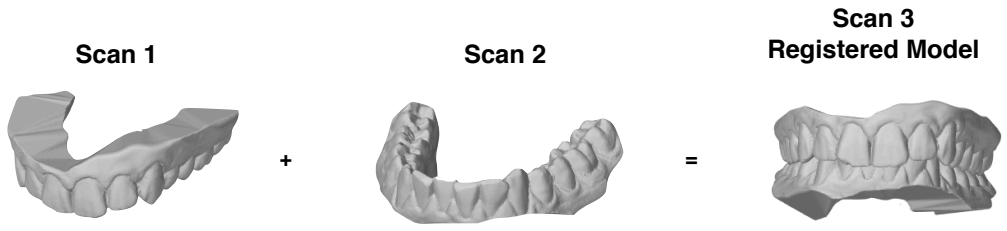

Figure 3.4: Scan 1 is of the maxillary teeth, scan 2 of the mandibular teeth, and scan 3 of the maxillary and mandibular teeth in their maximal ICP relationship.

1. The tracking harness must not interfere with the occlusal surface of the teeth because the overall aim of this development is to simulate and ultimately analyse occlusal dynamics.

2. Since the tracking system is limited to a single camera, it must be able to see as many ApirlTags as possible from a single camera.

3. The size of the marker should be as small as possible to allow for easy positioning.

Mounting Method

Figure 3.5 shows the progression of the mounting method of the markers to the teeth surface. For concepts 1, 2, and 3 the idea was to 3D print the tracking harness and the use a dental grade plastic suck down to generate a negative (Figure 3.5B). The negative would conform to a person's oral anatomy and then be cut out so that there was no material inhibiting the occlusal surface. The marker structure then could be attached to pin slots with a locating feature.

The issue with this method was once the centre of the suck down negative was removed it was incredibly flimsy, which is not ideal for tracking.

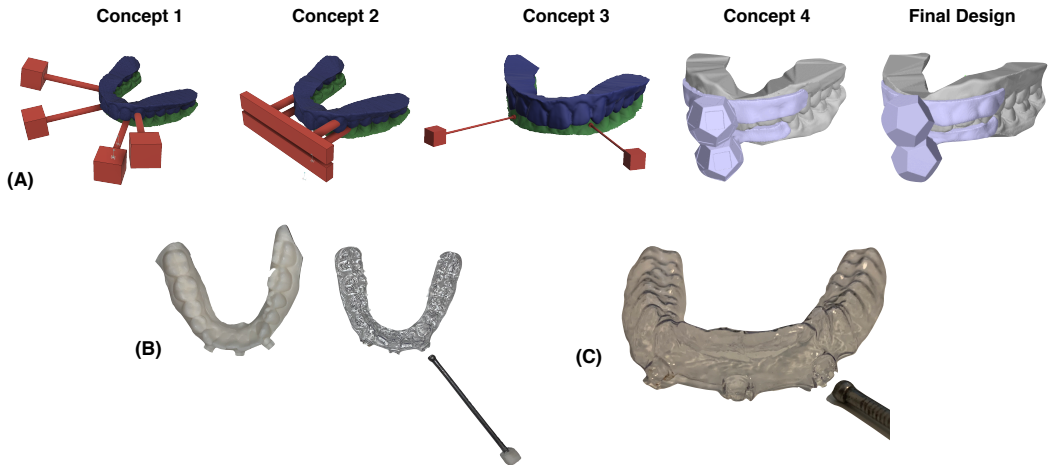

Figure 3.5: (A) Tracking harness design progression. (B) A preliminary mounting method with a suck down negative. (C) A closeup view of the suck down negative and interface to a marker structure concept.

If the harness moves around while in motion a poor estimate of its pose w.r.t. the camera will result, therefore this mounting method was not ideal.

Ultimately, the chosen concept for mounting the tracking harness to the teeth was concept 4 (Figure 3.5A). In CAD design software the buccal surface of the upper and lower teeth was offset from their initial maximal ICP pose and the dodecahedron tracking marker fixed to it. The tracking harness fits extremely well and almost is fixed without any adhesive. However, to minimize movement of the tracking harness during chewing, a minimal amount of dental adhesive can be use or appliance designed with small clasps to hook around the cusps of the teeth. One strength of this design is that the tracking harness designer can fit any existing oral anatomy such as an implant or pre-existing dental prosthesis.

Marker Shape

Typically, cube markers are used in photometric tracking applications, however with a single camera oftentimes pose ambiguity occurs and makes it difficult to

estimate the most likely pose of the marker [13]. To avoid this problem angled faces that are visible to the camera are helpful, and comparing the shape of the AprilTag to some different platonic solids (Figure 3.6A) the face of the dodecahedron fits a square binary fiducial well because the size of the tag can be made much bigger, which is key to accurate detection.

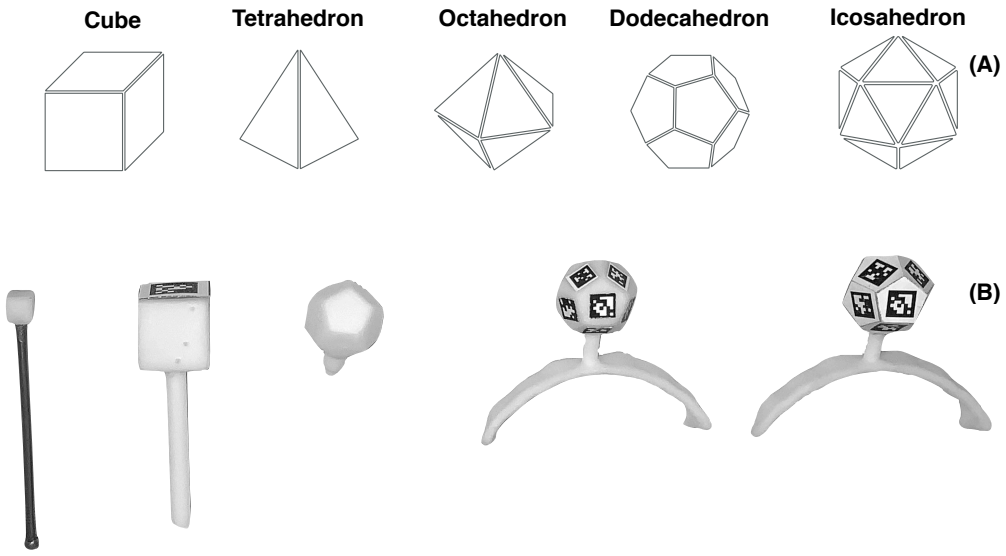

Figure 3.6: Tracking harness marker concepts. (A) platonic solids considered for the marker shape, and (B) fabricated version of the tracking harness and marker interfaces.

Figure 3.6B shows two versions of the dodecahedron marker. The one second from the right has a square locating feature that the AprilTag sits in to ensure that its position would be consistent from one tracking harness to another. The AprilTag was printed out as a smaller square and fit inside. The other (far right) has a flat face that the AprilTag was mounted to. Each AprilTag was printed out as a pentagon to match the dimensions of the dodecahedron face. The locating feature was unfortunately difficult to reproduce and limited by the 3D printer resolution. Therefore, the flat face was selected to avoid any bending or folding of the AprilTag.

Final Design

The final tracking harness design (Figure 3.7) includes the dodecahedron marker and 3D printed buccal surface fit. The two dodecahedrons have a side length of 12.7mm and are positioned so that the camera can see at least 3 tags on each from any camera view. Each tracking harness was 3D printed with a Form 2 SLA (formlabs, Somerville, Massachusetts) and 12 unique binary fiducial markers (AprilTag) were laser printed at 600 dpi and die-cut out of an adhesive and non-reflective paper, with the boarders aligned to the faces of the dodecahedron. The printed AprilTags were then mounted to the dodecahedron faces. The orientation of the AprilTags was chosen so that the Y-axis approximately intersected with a vertex on the dodecahedron face and the X-axis was approximately parallel to one of the edges.

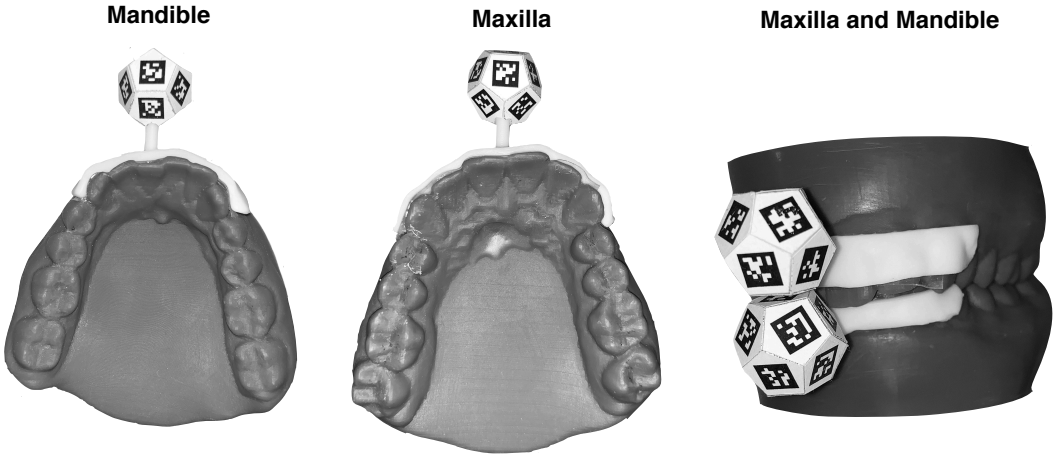

Figure 3.7: Tracking harness final design.

3.6 Dodecahedron Registration

To help reduce computational complexity, a coordinate frame attached 3D virtual model of each dodecahedron was aligned with the pose of the dodecahedron at the end of each tracking harness (Figure 3.8) with an iterative closest point algorithm programmed in ArtiSynth.

Only the pose of the dodecahedron w.r.t. the maxilla and mandible virtual models are required to track mandibular motion.

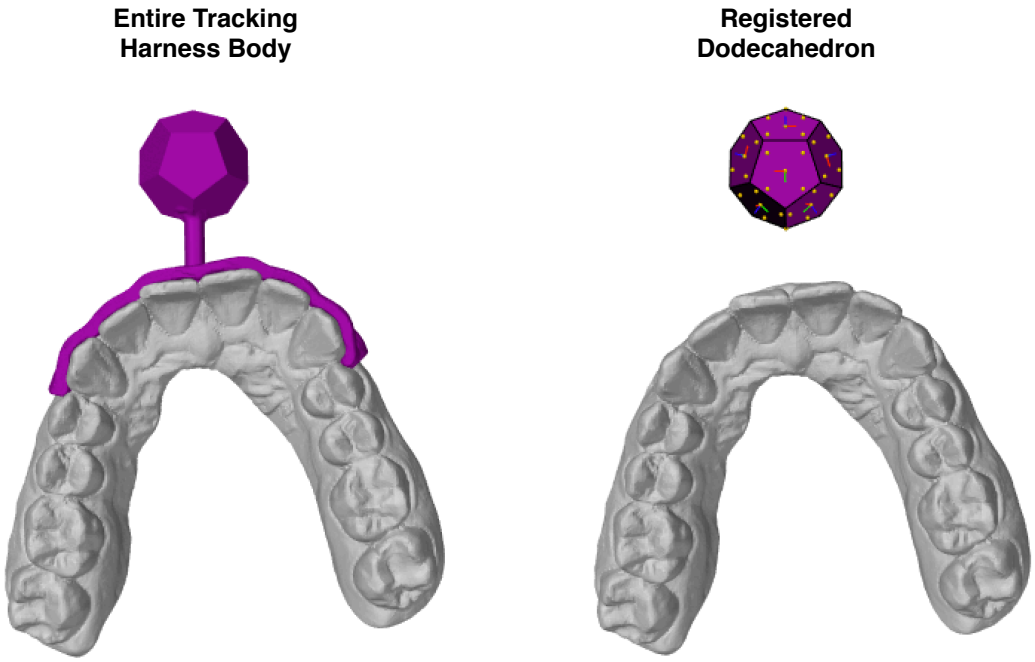

Figure 3.8: Tracking harness registration.

An iterative closest point algorithm automatically identifies corresponding pairs of points within a source and target geometry (Figure 3.9). Once identified, the iterative closest point algorithm minimizes the distance between all of the point pairs within each geometry until the minimum is reached and convergence is achieved. To execute the iterative closest point registration, we used ArtiSynth's built in functionality and prepare an interface to perform the registration. First, the target and source are loaded into ArtiSynth as meshes. The target mesh is the position and orientation of the dodecahedron w.r.t. the tracking harness coordinate system. The initial pose of the source or separated dodecahedron model was at the world origin of ArtiSynth. Next, the user performed a drop and drag transform to position the dodecahedron model as close as possible to the tracking harness's dodecahedron as an initial guess for the minimization problem. Otherwise, there is a possibility that the

iterative closest point registration converges to the wrong transformation and does not align the vertices of the dodecahedron correctly. Upon convergence, the respective rotation and translation are recorded and saved to a text file that is subsequently used in the jaw tracking visualization module.

Figure 3.9: Dodecahedron iterative closest point registration.

3.7 AprilTag Detection

The AprilTag detection (APRIL Robotics Laboratory, University of Michigan, MI) system has two parts: the tag detector and the coding system [87]. The AprilTag system is used to identify the upper and lower dodecahedrons (Figure 3.10). There are a number of different tag families, Tag36h11, TagStandard41h12, TagStandard52h13, TagCircle21h7, TagCircle49h12, and TagCustom48h12. The prefix refers to the number of encoding bits and the suffix refers to the minimum Hamming distance for each family. In this work, we use tag family Tag36h11 based on the suggestion of the APRIL Robotics Laboratory (University of Michigan, MI, USA).

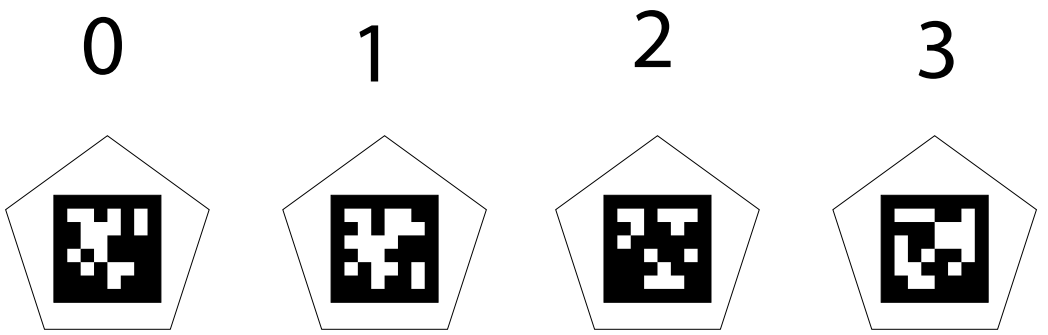

Figure 3.10: Examples of AprilTag 36h11 tag family. Left to right tag 0, tag 1, tag 2, and tag 3.

Coding System

The coding system works based on modified lexicography [88]. In text format, lexicography is easy to understand because a dictionary is sorted in lexicode or alphabetical order. The method can be extended to a binary representation where all of the words in the dictionary can be represented in a binary format. To find a codeword in a dictionary D each code word has a size n (number of bits) and a minimum Hamming distance d. Where the dictionary D of tags is defined as:

$$D = \begin{bmatrix} id = 0, bits = 1010\,1111\,1 \\ id = 1, bits = 1010\,1011\,1 \\ \vdots \\ id = x, bits = 1100\,1100\,1 \end{bmatrix}. \tag{3.1}$$

Assume that the tag in Figure 3.11 has an 9 bit payload, $id = 1$ and the search criteria is a minimum Hamming distance $d = 1$. To calculate d, a bitwise XOR comparison is completed against each entry in the dictionary D to find the closest code words to a tags payload. For example, the bitwise XOR comparison for tag 0 with tag 1 would be completed as follows:

$$\begin{array}{ll} 1010\,1111\,1 & id = 0 \\ \underline{1010\,1011\,1} & \underline{id = 1} \\ 0000\,0100\,0 & \text{bitwise XOR, where } d = 1 \end{array} \tag{3.2}$$

The Hamming distance is 1 because there is only one entry in each code that is different. If there were two bit position that were not the same the Hamming distance would increase to 2. This calculation finds potential matches for tag 1 and then the comparison is refined to determine an exact match. This method is simple, efficient and is considered to be optimal for this type of search problem [89].

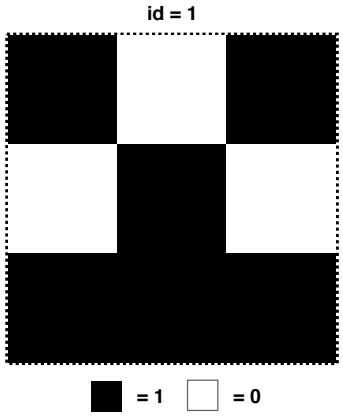

Figure 3.11: Example of a 9 bit fiducial marker tag with a minimum hamming distance of 1.

Detection System

The AprilTag detection system works by collecting a camera image and first converting it into a black and white image. Next, an adaptive threshold technique [90] is applied to find the minimum and maximum values of the pixels within a specific region. The specific regions that have high contrast values are kept and the rest of the image is excluded. A union-find algorithm [91] then masks the edges of the shapes that make up the AprilTag segmenting the edges that border the same black and white region. Finally, calculated quads

(outline of tag) are fit to the image to match the border of the AprilTag and poor fitting quads are discarded on each camera frame.

The quad decimate parameter is used to specifying the accuracy of tag detection and in this work we provide the user with an option in the iPhone® application to choose from a range of 1 (most accurate) to 4 (least accurate). The quadSigma parameter sets the level of Gaussian blur and helps interpret noisy or quickly moving images. More Gaussian blur will blur the image more, but in a noisy image, this might help with AprilTag detection. A value of 0 indicates a stationary tag and a value 0.8 applies a blur to the image. Finally, the Hamming limit (0 or 1) works by setting the goal for the detection algorithm and is set to 0 to get the most optimal AprilTag detection.

3.8 Tracking Harness Pose Estimation

In this section, we formulate the problem for the tracking harness pose estimation. First, we define the prospective projection model of a camera in this context, next we define the jaw coordinate system, then the dodecahedron coordinate system, and finally, we describe the implementation used to estimate the maxilla and mandible dodecahedron pose. The mathematical notation for describing the position and orientation of a rigid body in space within this thesis is defined in Appendix C.

Perspective Point and Projection Camera Model

Given a tracking object target J_t in the jaw frame $\{\mathrm{J}\}$, the goal is to recover the target(s) 6 DoF rotation and translation parameterization w.r.t. a calibrated camera coordinate system $\{\mathrm{C}\}$.

The 6 DoF pose parameterization of J_t is estimated by obtaining a set of expected 3D points in the jaw frame {J}, ${}^{J}\mathbf{x}_i = [x_i, y_i, z_i]^\top$ where the number of points $n \geq 3$ and a set of the 3D points corresponding camera image points in $\mathcal{I}_C$, ${}^{\mathcal{I}}\mathbf{u}_i = [u_i, v_i]^\top$ as illustrated within Figure 3.12.

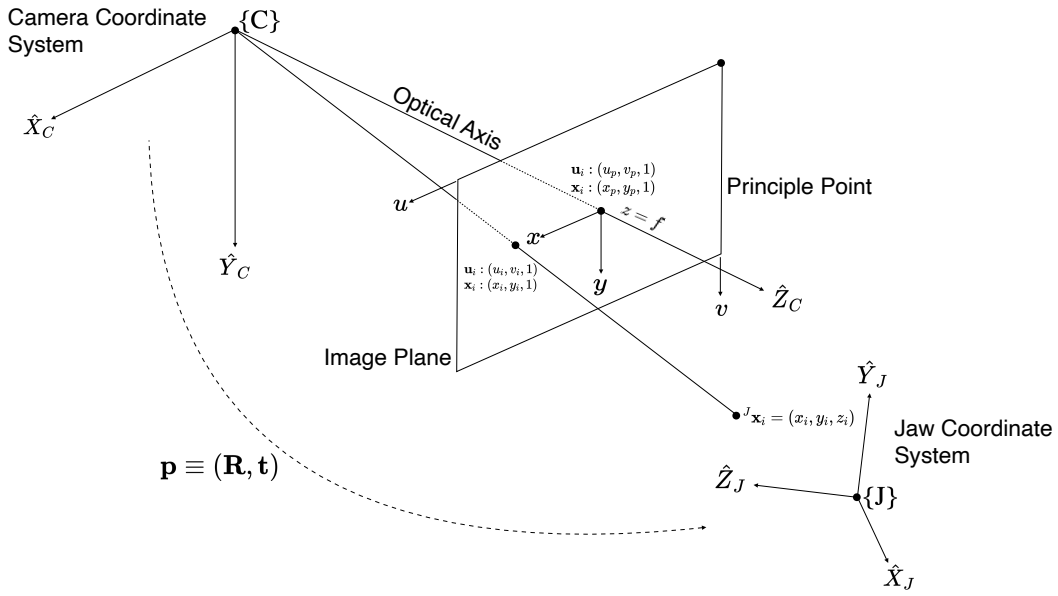

Figure 3.12: The prospective projection camera model. ({J}, $\hat{X}_J, \hat{Y}_J, \hat{Z}_J$) is the jaw coordinate system, ({C}, $\hat{X}_C, \hat{Y}_C, \hat{Z}_C$) is the camera coordinate system, ${}^{J}\boldsymbol{x}_i$ is a 3D point and ${}^{\mathcal{I}}\boldsymbol{u}_i$ is the same point projected onto the image plane of the camera $\mathcal{I}_C$.

The relationship between a point within the jaw frame and its corresponding Cartesian position on an image plane $\mathcal{I}_C$ is made based on the physical properties (intrinsic parameters) of a camera lens where, the f is the focal length and ${}^{\mathcal{I}}\mathbf{u}_p = [u_p, v_p]^\top$is the principle point. The focal length of the camera is a measure of how strongly a lens converges or diverges light. In the prospective projection camera model the image plane is placed in front of the camera to avoid inverted images. Therefore, the focal length is positive because light converges to the origin of camera frame {C}. The tracking object (J_t) will appear smaller when light reflects off it in frame {J} and lands on the image plane. To compute the correct size of the tracking object, a similar

triangles ratio is solved to compute the intersection with the image plane from the ray originating at ${}^{J}\mathbf{x}_i = [x_i, y_i, z_i]^\top$ and the mapping ends up being:

$$ {}^{J}\mathbf{x}_i = [x_i, y_i, z_i]^\top \Longrightarrow {}^{\mathcal{I}}\mathbf{x}_i = \left[f\frac{x_i}{zi}, f\frac{y_i}{z_i}, f \right]^\top . \tag{3.3} $$

To account for the change in dimension (3D to 2D) the z coordinate is dropped and the mapping is represented in homogeneous coordinates instead of Cartesian coordinates as shown below:

$$ {}^{J}\mathbf{x}_i = [x_i, y_i, z_i, 1]^\top \Longrightarrow {}^{\mathcal{I}}\mathbf{x}_i = \left[f\frac{x_i}{zi}, f\frac{y_i}{z_i}, 1 \right]^\top $$

then expressed in matrix notation within the homogeneous coordinate system:

$$ \begin{bmatrix} {}^{\mathcal{I}_c}x_i \\ {}^{\mathcal{I}_c}y_i \\ 1 \end{bmatrix} = \begin{bmatrix} f & 0 & 0 & 0 \\ 0 & f & 0 & 0 \\ 0 & 0 & 1 & 0 \end{bmatrix} \begin{bmatrix} {}^{J}x_i \\ {}^{J}y_i \\ {}^{J}z_i \\ 1 \end{bmatrix} . \tag{3.4} $$

Changing the coordinate system from Cartesian to homogeneous coordinates is standard in computer vision and AR for modelling the effect of a camera and representing the image formation process.

Images in a digital camera are formed by the illumination of pixels and the position of the image in the pixel coordinates system (u, v) is calculated by relating the ratio between the focal length f, the pixel width l_x, and height l_y derived from the resolution of the camera image. The focal length to pixel width ratios p_x and p_y are:

$$ p_x = \frac{f}{l_x} \quad and \quad p_y = \frac{f}{l_y}, \tag{3.5} $$

its corresponding position ${}^{\mathcal{I}_C}\mathbf{x}_i$ in ${}^{\mathcal{I}_C}\mathbf{u}_i$ coordinates is:

$$u_i = u_p + x_i p_x \quad and \quad v_i = v_p + v_i p_y, \tag{3.6}$$

and then expressed in matrix notation we arrive at the camera intrinsic parameters matrix:

$$\mathbf{K} = \begin{bmatrix} p_x & 0 & u_p \\ 0 & p_y & v_p \\ 0 & 0 & 1 \end{bmatrix}. \tag{3.7}$$

Finally, with a known camera position and orientation to convert a point ${}^{J}\mathbf{x}_i$ in the jaw frame to a point ${}^{\mathcal{I}_C}\mathbf{x}_i$ on the image plane in (u, v) coordinates the problem is formulated as:

$$\begin{bmatrix} u_i \\ v_i \\ 1 \end{bmatrix} = \mathbf{K}[\mathbf{R} \mid \mathbf{t}] \begin{bmatrix} x_i \\ y_i \\ z_i \\ 1 \end{bmatrix}, \tag{3.8}$$

where

$$\mathbf{K} = \begin{bmatrix} p_x & 0 & u_p \\ 0 & p_y & v_p \\ 0 & 0 & 1 \end{bmatrix}, [\mathbf{R} \mid \mathbf{t}] = \begin{bmatrix} R_{11} & R_{12} & R_{13} & t_x \\ R_{21} & R_{22} & R_{23} & t_y \\ R_{31} & R_{32} & R_{33} & t_z \end{bmatrix} \tag{3.9}$$

are the camera intrinsic parameters matrix and the camera extrinsic matrix or in other words the augmented rotation and translation of the camera in 3D.

Jaw Coordinate System

The jaw coordinate system {J} is set in ArtiSynth to be aligned with maxilla dodecahedron coordinate frame {DMax}. The centroid of the maxilla dodecahedron is at the origin of the jaw coordinate system. The mandible dodecahedron's centroid is located at the origin of its coordinate system. The origin of the {Max} and {Mand} coordinate systems are attached to their centre of masses. The centre of mass was calculated based on the tooth model geometry and an estimated mass of $100g$ [11].

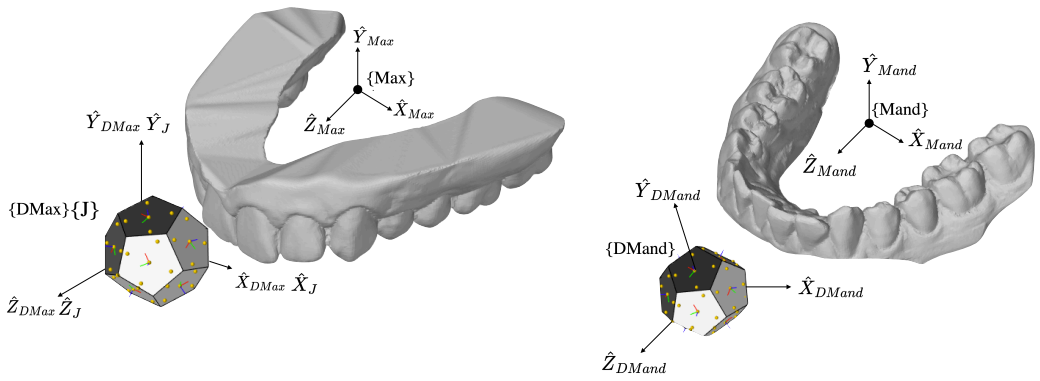

Figure 3.13: Position and orientation of {Max} and {Mand} with respect to {DMax} and {DMand}. The {DMax} origin is aligned with {J}.

Defining Dodecahedron Model

The dodecahedron model was built by setting $\hat{Z}_{DMax}$ and $\hat{Z}_{DMand}$ to pass through the vertex pointing towards the camera. This was done so that the camera z-axis unit vector ($\hat{Z}_C$) is orthogonal to the maxilla and mandible tracking harness and the camera can see at least 3 faces.

There are 12 faces on each dodecahedron and each face of the model has a number that is associated with an AprilTag that has the same number. The maxilla dodecahedron has faces $(F_0, F_1, ..., F_{11})$ and the mandible dodecahedron has faces $(F_{12}, F_{13}, ..., F_{23})$ where $F_0 = F_{11}$ and so on. The dodecahedron coordinate systems are identical, however, their face and AprilTag numbers are different to identify them within the camera image (Figure 3.14).

Obtaining Correlating 3D Points on Image Plane

To get the points in the camera image, the AprilTag detection algorithm (Section 3.7) is used by VISP to obtain a list of each tags centre point and respective corner points in (u, v) coordinates. These points are then converted into the Cartesian coordinates on the image plane with the intrinsic camera matrix by solving for x_i and y_i from Equation 3.10 below:

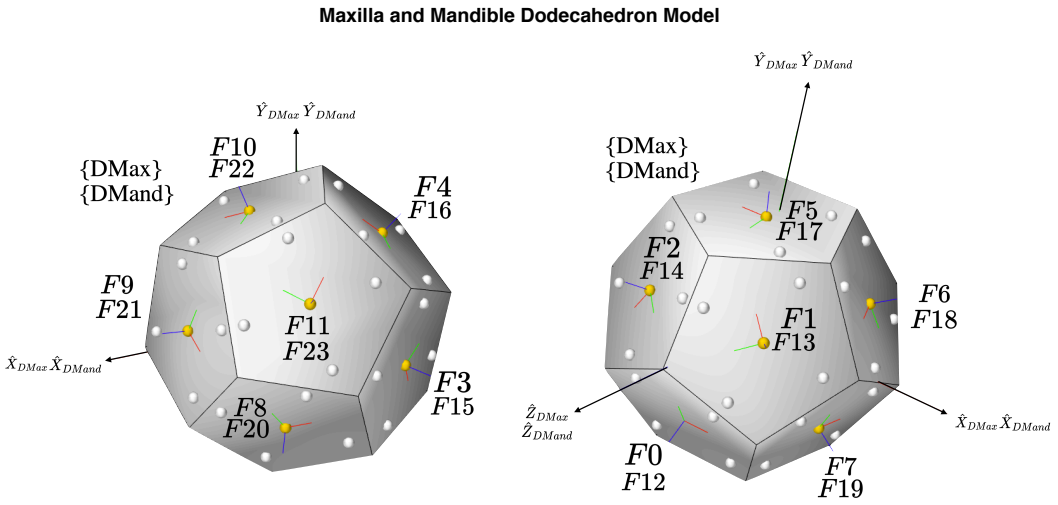

Figure 3.14: The identification of the maxilla and mandible dodecahedron's. Each face correlates with the same identification number of AprilTags. Thus, tag 1 is on face 1 of the maxilla. Tags and faces 0-11 are for the maxilla dodecahedron and tags and faces 12-23 are for the mandible dodecahedron.

$$x_i = \frac{u_i - u_p}{p_x}, y_i = \frac{v_i - v_p}{p_y}. \tag{3.10}$$

To get the corresponding corner and centre points within the 3D model, they are calculated beforehand by utilizing the geometry of the dodecahedron and the relationship to each face frame coordinate system. The homogeneous transformation matrix is calculated w.r.t. the dodecahedron coordinate system. From here, the homogeneous ${}^{Dx}\boldsymbol{P}_i : (X_i, Y_i, Z_i, 1)$ is extracted from the translation vector, where x is a place holder for the maxilla and mandible dodecahedron. The respective AprilTag corner point translation vectors are also computed to obtain a list of all the AprilTag corners and centre points w.r.t. the dodecahedron coordinate system. Figure 3.15 shows the AprilTag centre points for tag and face ids 0, 1, and 5 in the observed camera image (u, v) and the 3D dodecahedron model {DMax}.

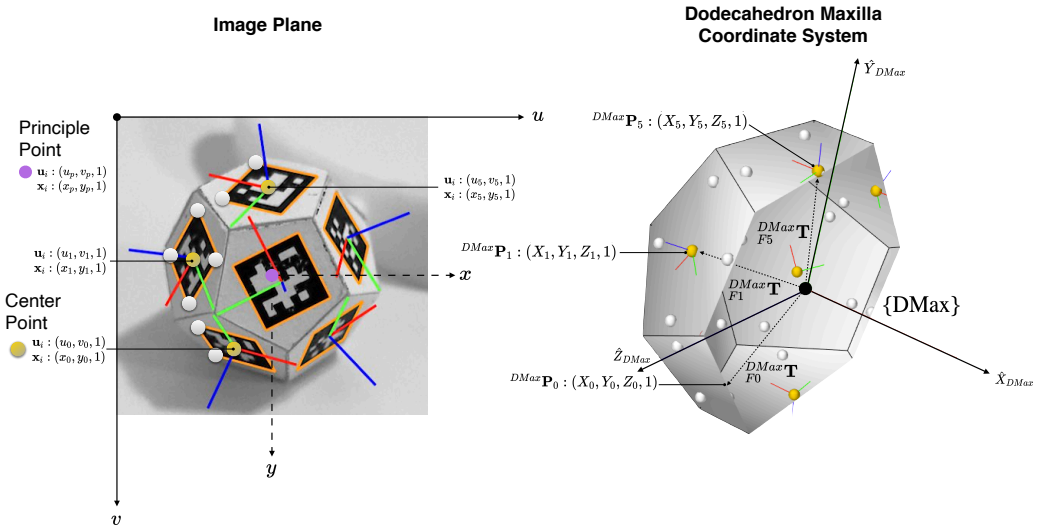

Figure 3.15: Corresponding image and model points.

Solving Perspective and Point Problem

To estimate the position and orientation of the maxilla and mandible dodecahedrons a PnP problem is solved by minimizing the error between the observed points on the camera image plane and the 3D points in the {J} frame. The goal is to adjust the camera pose so that a point projected onto the image plane is as small as possible. This generates a non-linear least squares problem and the transform w.r.t. {C} can be optimized based on its re-projection error. The error function is formulated as:

$$E_r({}^{\mathbf{C}}_{\mathbf{J_t}}\mathbf{T}) = \frac{1}{n}\sum_{i=1}^{n}\left((\hat{u}_i - u_i)^2 + (\hat{v}_i - v_i)^2\right) \tag{3.11}$$

where $\hat{\mathbf{u}}_i = [\hat{u}_i, \hat{v}_i]^\top$ is a list of all the observed points and $\mathbf{u}_i = [u_i, v_i]^\top$ is a list of the projected points all on the image plane $\mathcal{I}_C$. To solve this non-linear least squares problem we use the implementation of the Levenberg-Marquadt method in VISP [85].

Calculating the Mandible Pose w.r.t. the Maxilla

Once the approximate pose of the mandible and maxilla dodecahedrons is solved we are left with a estimated ${}^{C}_{DMax}\mathbf{T}$ and ${}^{C}_{DMand}\mathbf{T}$. From here we can calculate the position and orientation of the mandible dodecahedron w.r.t. the maxilla dodechedron:

$$ {}^{DMax}_{DMand}\mathbf{T} = {}^{DMax}_{C}\mathbf{T} \; {}^{C}_{DMand}\mathbf{T} \quad , \quad {}^{DMax}_{C}\mathbf{T} = {}^{C}_{DMax}\mathbf{T}^{-1}. \tag{3.12} $$

The minimization problem solves for the pose of the maxilla dodecahedron w.r.t. the camera, therefore to compute the pose of the mandible w.r.t. the maxilla we need to compute the inverse ${}^{C}_{DMax}\mathbf{T}^{-1}$ which provides the correct transformation. Since the {Max} and {Mand} coordinate systems are rigidly attached to {DMax} and {DMand} their position and orientation is updated based on the dodecahedron poses on every captured camera image. The coordinate frame transformations are illustrated below in Figure 3.16.

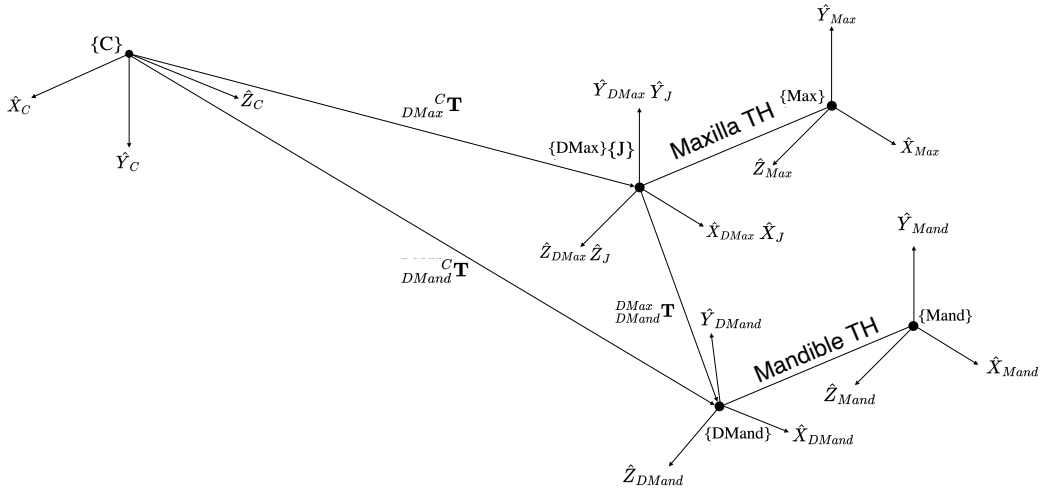

Figure 3.16: Coordinate frame transformation to determine the pose of the mandible w.r.t. the maxilla.

3.9 Maximal Intercuspation Calibration Step

Before recording jaw motion with the iPhone® tracking application we first perform a maximal ICP calibration step. The adjustment step repositions the registered mandibular tracking harness dodecahedron pose relative to the mandible coordinate system {Mand}. The purpose is to make sure potential error from the dodecahedron pose estimation does not impact the contact pattern at maximal ICP. A small error in the dodecahedron pose relative to the camera will result in a larger error of the mandible's pose and this step corrects for that.

First, we transmit tracking data from the iPhone® tracking application to the real-time visualization module in ArtiSynth. Next, we detach the mandible dodecahedron from the mandible coordinate system so that it is free to move. Once the iPhone® application produces stable AprilTag detection we reattach the mandible dodecahedron to the mandible coordinate system and visually verify that mandible posture is the same as the ground truth intra-oral scanned pose. This is very important because it makes sure that the mandible is the correct initial pose before recording jaw motion.

3.10 Benchtop Evaluation of Accuracy

3.10.1 Experiment 1

The first goal of experiment 1 is to determine if the camera angle and distance has an impact on the static accuracy of the iPhone® application. The second goal is to identify the angle and distance that the iPhone® tracking application produces the best static accuracy. This is important because it will help craft a recommendation for positioning the iPhone® to achieve the best tracking results.

To determine if camera angle and distance has an impact on the static accuracy of the iPhone® application we measured the accuracy at different camera angles (0°, 30°, and 60°) and corresponding distances (80mm, 100mm, and 120mm) while fixed to a tripod. At each angle and distance combination, we recorded data collected by the iPhone® to estimate the 3D position and orientation of the mandible dodecahedron w.r.t. the maxilla dodecahedron. Measurements from the iPhone® were collected for 5 seconds at each angle and each distance. The recording was repeated 5 times at each angle and distance. Measurements were taken at the 9 positions illustrated in Figure 3.18. Measurements could have been taken on the right side as well but were not because the dodecahedrons are symmetrical.

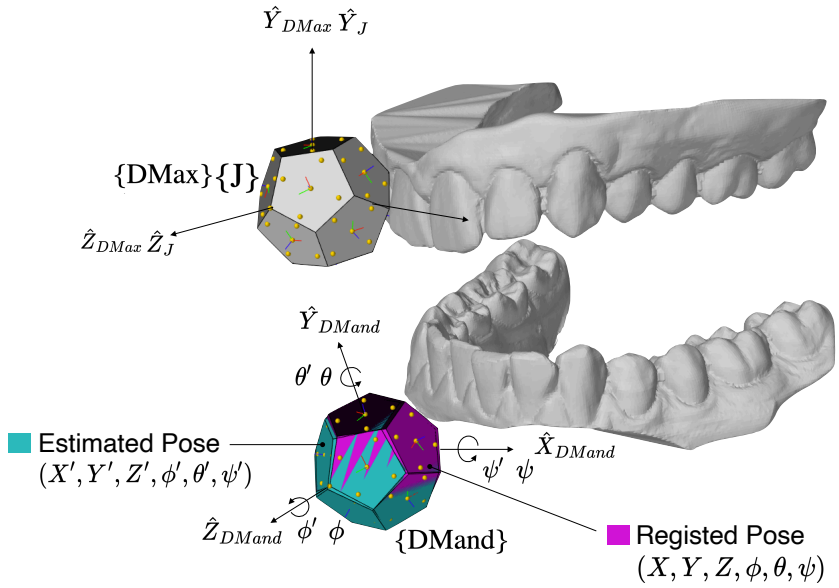

Figure 3.17: The static error is calculated by parameterizing the registered virtual model mandible pose $(X, Y, Z, \phi, \theta, \psi)$ and the estimated pose $(X', Y', Z', \phi', \theta', \psi')$ in terms of their positions and Euler angles. The error in the pose is calculated by the difference between registered purple dodecahedron pose and the estimated turquoise dodecahedron pose. The purple dodecahedron is superimposed onto the turquoise dodecahedron to illustrate the error between the registered dodecahedron and the estimated one.

To measure the static accuracy of the iPhone® tracking application, we use the pose of the mandible dodecahedron in its registered maximal ICP w.r.t. the {DMax} coordinate system from the intra-oral scan data as ground truth (${}^{DMax}_{DMand}\mathbf{T}$). We then take the difference between the iPhone® application's estimated pose of the mandible dodecahedron w.r.t. the {DMax} coordinate system (${}^{DMax}_{DMand}\mathbf{T}'$) to calculate the static pose error (Figure 3.17). This error is a measure of the iPhone® application's static accuracy.

More specifically, to calculate the pose error of the mandible dodecahedron w.r.t. the {DMax} coordinate system we paramaterize (${}^{DMax}_{DMand}\mathbf{T}$) into its (X, Y, Z) position and (ϕ, θ, ψ) orientation representation, and we also paramterize and (${}^{DMax}_{DMand}\mathbf{T}'$) into its (X', Y', Z') position and (ϕ', θ', ψ') orientation representation. The angles (ϕ, θ, ψ) and (ϕ', θ', ψ') are the Euler angles and the details of the specific parameterization are described in Appendix C. The angles are small, and therefore it is reasonable to use this parameterization to represent rotations about $(\hat{X}_{DMand}, \hat{Y}_{DMand}, \hat{Z}_{DMand})$ with angles (ϕ, θ, ψ) to measure the registered and iPhone® estimated orientation of the mandible dodecahedron without being concerned with an erroneous rotation error. Thus, the static error measures become:

$$\begin{bmatrix} X_{err} \\ Y_{err} \\ Z_{err} \end{bmatrix} = \begin{bmatrix} X' \\ Y' \\ Z' \end{bmatrix} - \begin{bmatrix} X \\ Y \\ Z \end{bmatrix} \; and \; \begin{bmatrix} \phi_{err} \\ \theta_{err} \\ \psi_{err} \end{bmatrix} = \begin{bmatrix} \phi' \\ \theta' \\ \psi' \end{bmatrix} - \begin{bmatrix} \phi \\ \theta \\ \psi \end{bmatrix}. \quad (3.13)$$

The mean and standard deviation position $(X_{err}, Y_{err}, Z_{err})$ and orientation $(\phi_{err}, \theta_{err}, \psi_{err})$ error of the mandible dodecahedron was then plotted to determine the effect of the various angles and distances tested on static accuracy.

3.10.2 Experiment 2

The goal and procedure for measuring the static accuracy of the iPhone® application are the same as in experiment 1. The only difference in the procedure is that we hold the iPhone® by hand at camera angles (0°, 30°, and 60°) and corresponding distances (80mm, 100mm, and 120mm). The purpose of this is to introduce noise into the system to see if it changes the best static accuracy result from experiment 1. By introducing noise into the system we can better understand how robust the iPhone® application is at jaw tracking jaw motion.

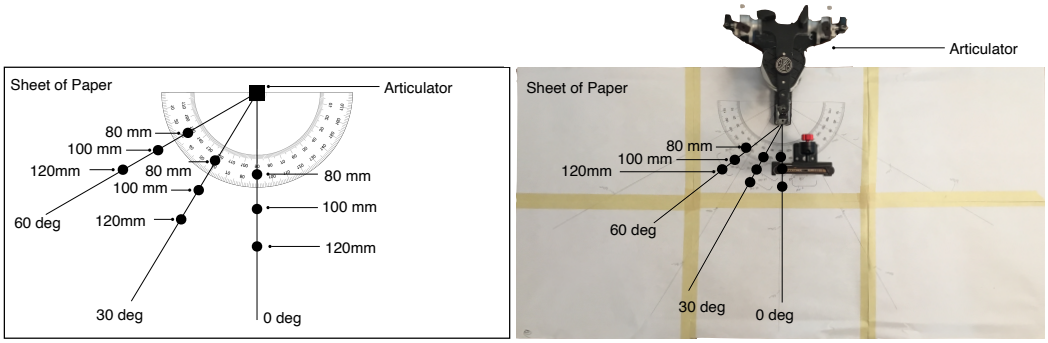

Figure 3.18: Static accuracy experimental setup.

3.10.3 Experiment 3

In experiment 3 we endeavour to determine if the iPhone® application can repeatably and accurately track the path of the mandible and maxilla dodecahedrons on a repeatable arced path.To do this, the maxilla and mandible tracking harnesses were mounted to the 3D printed casts on the semi-adjustable articulator we used in this work. The semi-adjustable articulator was used to complete 30 open-close cycles at distances of 10, 20, 30, and 40mm between the estimated maxilla and mandible incisor point. The semi-adjustable articulator rotates the maxilla about a fixed transverse axis that passes through the condyle joints creating a repeatable arced path as illustrated in Figure 3.19.

The operator manually opened and closed the articulator to each target opening distance. To notify the operator when the maximum opening distance was reached we calculate it in ArtiSynth and displayed the real-time values on a graph visible to the operator. After the 30 open-close cycles were completed, the arced trajectories were saved and then scatter plotted on the sagittal and coronal planes.

To measure the trajectory error, a linear regression was completed to fit a statistical model to the scatter plot points on each plane. With this model, we report the Pearson correlation coefficient, the 95% confidence interval of the regression line, the 95% prediction band of the data points, and the standard error which is the vertical distance from the regression line to the 95% prediction band.

We use the standard error as an approximate measure of dynamic accuracy because it has a distance unit attached to it, making it easier to interpret the results. Standard error quantifies the average deviation from the trajectory reflecting the consistency at which the camera can capture the motion as the maxilla model is repeatedly moving along its trajectory defined by the semi-adjustable articulator.

3.11 Virtual Simulation of Occlusal Interactions

To demonstrate how the iPhone® tracking application can be used to recreate occlusal interactions virtually, we simulate them kinematically (without occlusal forces) and dynamically (with occlusal forces). Both the kinematic and dynamic simulation use the mandible trajectory from the iPhone® application to move the mandible from an initial pose to a final pose. In the kinematic simulation, contact is visualized on the occlusal surface by detecting regions where the maxillary and mandibular teeth touch. Because of measurement

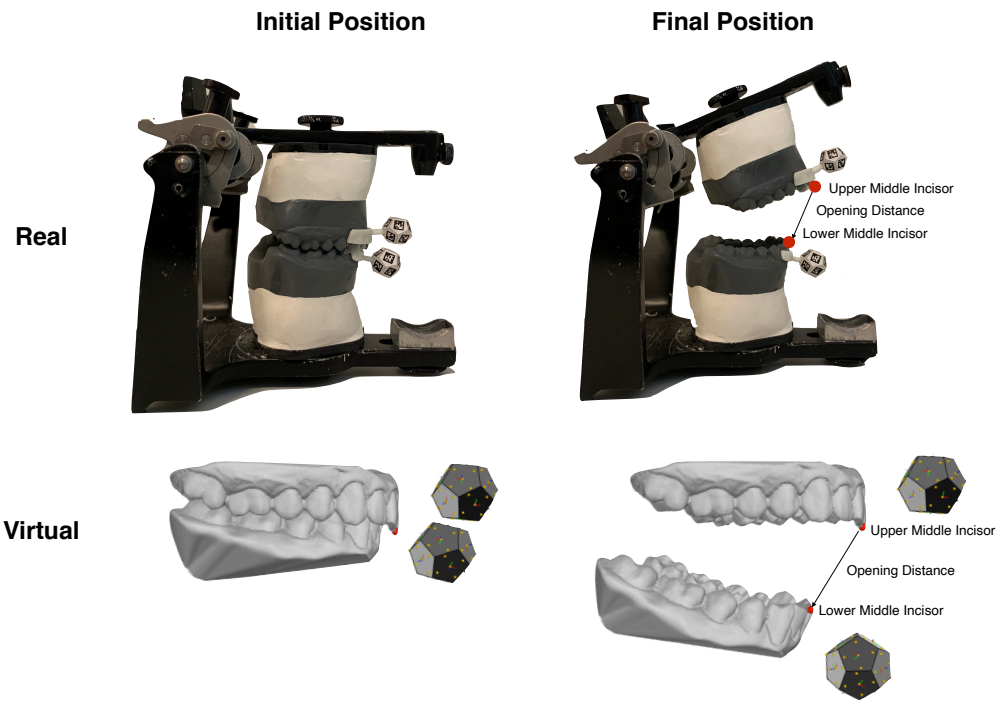

Figure 3.19: Dynamic accuracy experimental setup.

noise, the teeth may interpenetrate in the visualization. To prevent this from happening, a dynamic simulation detects when the opposing teeth collide and create reactionary forces that adjust the movement trajectories accordingly in the simulation. The basis for the kinematic and dynamic simulation is adapted from Stavness *et al*. [11].

3.11.1 Kinematic Simulation

The goal of simulating occlusal interactions kinematically (without occlusal forces in ArtiSynth) is to qualitatively analyze the contact patterns of three typical motions used to design a dental prosthesis. Three typical motions are performed on the semi-adjustable articulator: a left lateral excursion, a right lateral excursion, and a protrusive excursion. The initial pose of each excursion is at maximal ICP and the final pose is at an arbitrary point in the left lateral, right lateral, and anterior direction.

First, each excursion motion is captured with the iPhone® application and the real-time visualization module in ArtiSynth. Next, the captured excursion from the iPhone® application, the registered maxillary and mandibular meshes from the intra-oral scanner, and dodecahedron virtual models created in ArtiSynth are loaded into the kinematic simulation module in ArtiSynth.

Each recorded excursion is reproduced in ArtiSynth and the kinematic simulation calculates the region of mesh interpenetration between the teeth at each updated mandible pose. The kinematic simulation marks the region of interpenetration with a 3D point as the excursion motion moves to its final captured pose.

Once all three excursion motions have been completed and their resulting occlusal contact simulated kinematically in ArtiSynth, we plot the trajectory of the lower middle incisor on the sagittal, coronal, and superior planes. Additionally, we capture an image of the contact pattern of all three excursions at their final and initial poses. With the plotted trajectories and the contact patterns, we perform a qualitative analysis of the trajectory that aims to determine the cause for noise in the trajectory and help us to understand how realistic the created contact patterns are.

3.11.2 Dynamic Simulation

The goal of simulating occlusal interactions dynamically (with occlusal forces) in ArtiSynth is to determine if there is a difference in the contact patterns generated kinematically (without occlusal forces). Additionally, we aim to demonstrate the procedure for completing dynamic tooth contact simulation in ArtiSynth with the same iPhone® application tracking data.

Initially, in ArtiSynth the maxillary and mandibular tooth meshes interpenetrate at maximal ICP. For dynamic simulation with collision detection, the meshes must not interpenetrate for collision detection to work correctly. We follow the method to adjust for mesh interpenetration of Stavness *et al.* [11].

Next, as per Staveness *et al.* [11] we use the available collision detection tools in ArtiSynth to adjust the pose of the mandible teeth at maximal ICP. In the pre-processing step, the collision detection simultaneously accounts for different tooth penetration depths and minimizes the displacement of the mandible teeth relative the maxillary teeth to produce an adjusted pose that is as close to maximal ICP as possible before dynamic simulation.

Finally, we use the left lateral excursion motion captured from the iPhone® tracking application in the previous section. The initial pose of the maxillary teeth was adjusted with the collision detection method keeping and the final pose remained the same as in the kinematic simulation. The initial and final poses were set in the adapted occlusal contact visualization module in ArtiSynth and motion was simulated by translating the mandibular teeth from its set initial pose at maximal ICP to its final pose. During the motion, the dynamic simulation calculates the reactionary forces applied to the mandibular teeth and they slide along the surface of the maxillary teeth, varying in 6 DoF instead of having the meshes interpenetrate as in the kinematic simulation.

Once complete, a qualitative comparison of the contact pattern resulting from the dynamic and kinematic simulation of occlusal contacts was performed. We aimed to identify similarities and differences between these two methods used within industry, academia, and clinical situations.

Chapter 4

Results

4.1 Benchtop Evaluation of Accuracy

The path of the 3D jaw poses were collected with the iPhone® application and transmitted to the real-time jaw tracking visualization module in ArtiSynth for data recording.

Section 4.1.1 presents the means and standard deviations for the iPhone® application's static accuracy at camera angles $(0°, 30°, 60°)$ and distances (80mm, 100mm, and 120mm) when fixed to a tripod. The goal of this experiment was to determine if the camera angle and distance had an impact on the iPhone® tracking application's static accuracy and to identify what camera angle and position yielded the best static accuracy. The static accuracy was measured by taking the difference $(X_{err}, Y_{err}, Z_{err}, \phi_{err}, \theta_{err}, \psi_{err})$ between the intra-oral scanned mandible's registered tracking harness dodecahedron and the iPhone® application's estimated pose of the registered tracking harness dodecahedron.

Section 4.1.2 presents the means and standard deviations of the static accuracy $(X_{err}, Y_{err}, Z_{err}, \phi_{err}, \theta_{err}, \psi_{err})$ at camera angles $(0°, 30°, 60°)$ and distances (80mm, 100mm, and 120mm) when the iPhone® was held by hand. The goal of this experiment was to evaluate if adding noise from the natural vibrations of the hand would impact accuracy results.

By introducing noise we can better understand how robust the iPhone® application is at tracking jaw motion.

Section 4.1.3 presents the linear regression models and their corresponding statistical measures of 30 open-close cycles at increasing opening distances (10, 20, 30, and 40mm). The goal of this experiment was to determine if the iPhone® application could repeatably and accurately track the path of the mandible and maxilla dodecahedrons on a known arced path. The repeatability was determined by the quality of linear regression fit and the dynamic accuracy is estimated with the standard error.

4.1.1 Experiment 1

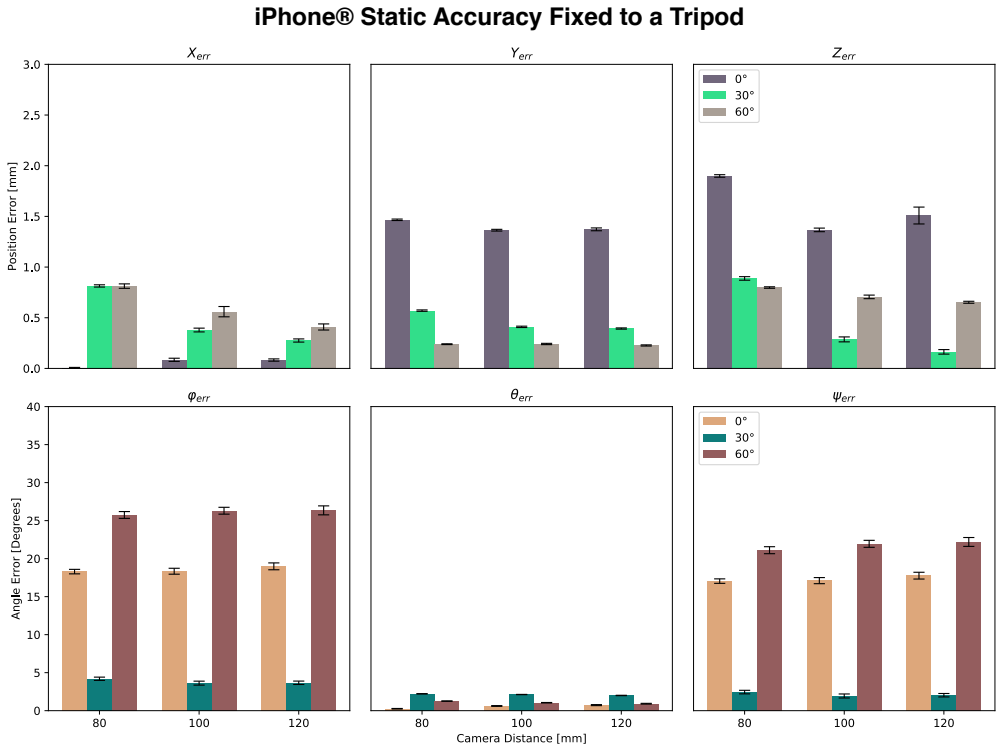

Figure 4.1: The mean error and standard deviation pose error (static accuracy) of the mandible dodecahedron w.r.t. {DMax} at camera distances 80mm, 100mm, and 120mm and camera angles 0°, 30°, and 60° fixed by a tripod. The X-axis is along the medio-lateral direction, the Y-axis is along the superior-inferior direction, and the Z-axis is along the posterior-anterior direction.

Figure 4.1 shows the mean (M) and standard deviation (SD) error bars of the iPhone® static accuracy measures ($X_{err}, Y_{err}, Z_{err}, \phi_{err}, \theta_{err}, \psi_{err}$) at increasing angle and distance when the iPhone® is fixed with a tripod. The exact values of the error bars in Figure 4.1 are reported in Tables 4.1,4.2, and 4.3.

At 80, 100, and 120mm the X_{err} (medio-lateral axis) increases with increasing angle, the Y_{err} (superior-inferior axis) decreases with increasing angle, and the Z_{err} (posterior-anterior axis) decreases with increasing angle. The X_{err}, Y_{err}, and Z_{err} are all under 1mm, except at a camera angle of 0° the Y_{err} and Z_{err} is over 1mm. The angles errors ($\phi_{err}, \theta_{err}, \psi_{err}$) are $< 5°$at a camera angle of 30° compared to camera angles 0° and 60° the errors are $> 15°$. The first observation is that the pose error of mandible dodecahedron was heavily impacted by angle and less by the distance. The second observation is that the static accuracy is best at a camera angle 30° and distances of 100mm and 120mm.

Table 4.1: iPhone® static accuracy at a camera angle of 0° (tripod).

Error	**80 [mm]**		**100 [mm]**		**120 [mm]**	
	M	SD	M	SD	M	SD
X_{err}	0.003	0.007	0.085	0.016	0.083	0.011
Y_{err}	1.466	0.007	1.364	0.009	1.372	0.014
Z_{err}	1.899	0.013	1.367	0.018	1.509	0.083
ϕ_{err}	18.294	0.296	18.343	0.390	18.987	0.452
θ_{err}	0.255	0.034	0.617	0.050	0.732	0.068
ψ_{err}	17.044	0.295	17.107	0.401	17.761	0.446

Table 4.2: iPhone® static accuracy at a camera angle of 30° (tripod).

Error	**80 [mm]**		**100 [mm]**		**120 [mm]**	
	M	SD	M	SD	M	SD
X_{err}	0.814	0.011	0.379	0.019	0.275	0.016
Y_{err}	0.570	0.007	0.410	0.007	0.394	0.006
Z_{err}	0.888	0.018	0.287	0.024	0.164	0.022
ϕ_{err}	4.198	0.214	3.623	0.260	3.670	0.223
θ_{err}	2.221	0.020	2.123	0.018	2.001	0.025
ψ_{err}	2.446	0.234	1.932	0.265	2.034	0.226

Table 4.3: iPhone® static accuracy at a camera angle of 60° (tripod).

Error	**80 [mm]**		**100 [mm]**		**120 [mm]**	
	M	SD	M	SD	M	SD
X_{err}	0.085	0.016	0.560	0.051	0.409	0.030
Y_{err}	1.364	0.009	0.241	0.006	0.227	0.006
Z_{err}	1.367	0.018	0.706	0.018	0.653	0.010
ϕ_{err}	18.343	0.390	26.302	0.451	26.350	0.590
θ_{err}	0.617	0.050	1.047	0.029	0.916	0.048
ψ_{err}	17.107	0.401	21.948	0.460	22.194	0.584

4.1.2 Experiment 2

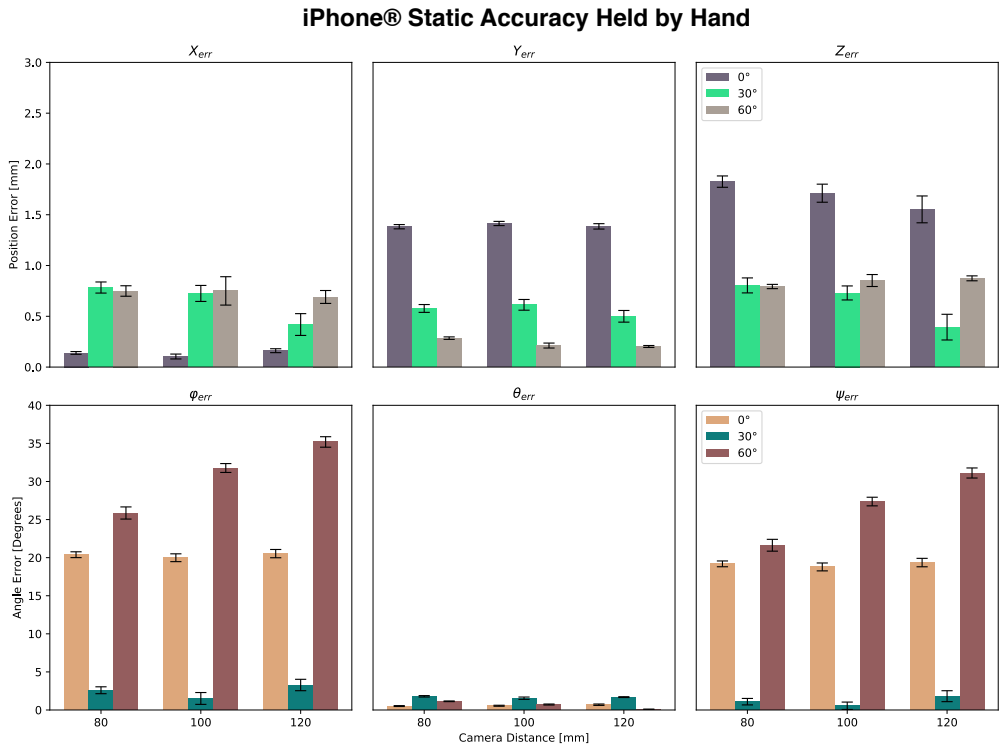

Figure 4.2: The mean error and standard deviation pose error (static accuracy) of the mandible dodecahedron w.r.t. {DMax} at camera distances 80mm, 100mm, and 120mm and camera angles 0°, 30°, and 60° held by a hand. The X-axis is along the medio-lateral direction, the Y-axis is along the superior-inferior direction, and the Z-axis is along the posterior-anterior direction.

Figure 4.2 shows the mean (M) and standard deviation (SD) error bars of the static accuracy measures $(X_{err}, Y_{err}, Z_{err}, \phi_{err}, \theta_{err}, \psi_{err})$ at increasing angle and distance when the iPhone® is held by hand. The exact values of the error bars in Figure 4.2 are reported in Tables 4.4, 4.5, and 4.6.

At 80, 100, and 120mm the $(X_{err}, Y_{err}, Z_{err})$ did increase compared to when the iPhone® was fixed to the tripod. For instance the X_{err} mean and standard deviation at 30° and 100mm increased from 0.379 ± 0.019mm to 0.725 ± 0.079mm, the Y_{err} increased from 0.410 ± 0.007mm to 0.613 ± 0.053mm, and the Z_{err} increased from 0.287 ± 0.024mm to 0.730 ± 0.069mm. The mean ϕ_{err}, θ_{err}, and ψ_{err} actually decreased from (3.623, 2.123, 1.932)mm to (1.515, 1.547, 0.553)mm and the standard deviations increased from (0.260, 0.018, 0.265)mm to (0.777, 0.153, 0.553)mm. This is an expected result because the orientation error of the mandible dodecahedron is more sensitive to the noise created by the natural vibrations of the hand. Overall, the only really significant difference when the iPhone® was held by the tripod and when it was held by hand was the general increase in the means of $(X_{err}, Y_{err}, Z_{err})$ and a noticeable increase of the ϕ_{err} and ψ_{err} at a camera angle of 60°.

The first observation is that the natural vibrations of holding the iPhone® by hand did not drastically change the impact of camera angle and distance on static accuracy compared to when the iPhone® was held by the tripod. The second observation is that the added noise did not change the 30° camera angle at distances of 100mm and 120mm from yielding the best static accuracy.

Table 4.4: iPhone® static accuracy at a camera angle of 0° (hand).

Error	**80 [mm]**		**100 [mm]**		**120 [mm]**	
	M	SD	M	SD	M	SD
X_{err}	0.139	0.013	0.104	0.024	0.161	0.019
Y_{err}	1.382	0.021	1.414	0.021	1.385	0.027
Z_{err}	1.826	0.056	1.712	0.089	1.553	0.132
ϕ_{err}	20.388	0.383	19.990	0.514	20.531	0.543
θ_{err}	0.517	0.058	0.557	0.065	0.694	0.092
ψ_{err}	19.186	0.380	18.783	0.518	19.355	0.554

Table 4.5: iPhone® static accuracy at a camera angle of 30° (hand).

Error	**80 [mm]**		**100 [mm]**		**120 [mm]**	
	M	SD	M	SD	M	SD
X_{err}	0.783	0.055	0.725	0.079	0.419	0.107
Y_{err}	0.577	0.039	0.613	0.053	0.500	0.057
Z_{err}	0.804	0.074	0.730	0.069	0.393	0.127
ϕ_{err}	2.592	0.453	1.515	0.777	3.281	0.748
θ_{err}	1.796	0.093	1.547	0.153	1.691	0.055
ψ_{err}	1.092	0.425	0.553	0.486	1.813	0.718

Table 4.6: iPhone® static accuracy at a camera angle of 60° (hand).

Error	**80 [mm]**		**100 [mm]**		**120 [mm]**	
	M	SD	M	SD	M	SD
X_{err}	0.104	0.024	0.750	0.140	0.690	0.064
Y_{err}	1.414	0.021	0.212	0.024	0.203	0.010
Z_{err}	1.712	0.089	0.852	0.059	0.874	0.024
ϕ_{err}	19.990	0.514	31.770	0.583	35.190	0.688
θ_{err}	0.557	0.065	0.719	0.066	0.070	0.049
ψ_{err}	18.783	0.518	27.367	0.566	31.115	0.661

4.1.3 Experiment 3

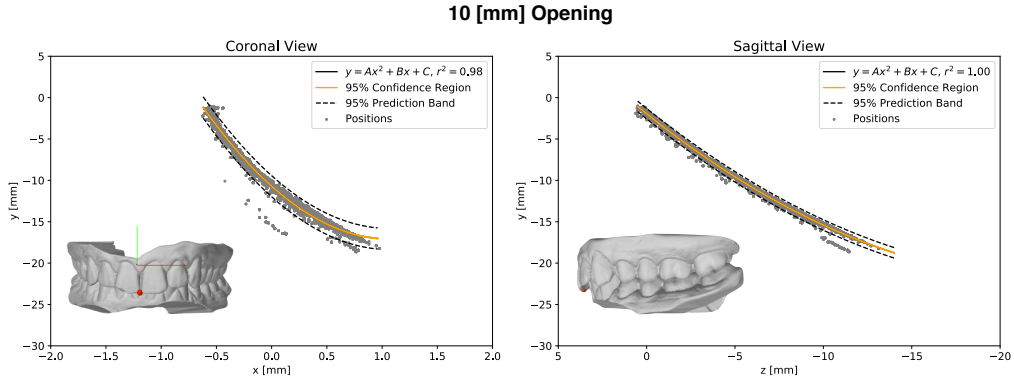

Figure 4.3: The coronal and sagittal view of the lower middle incisor trajectory at 10mm of opening during 30 open and close cycles.

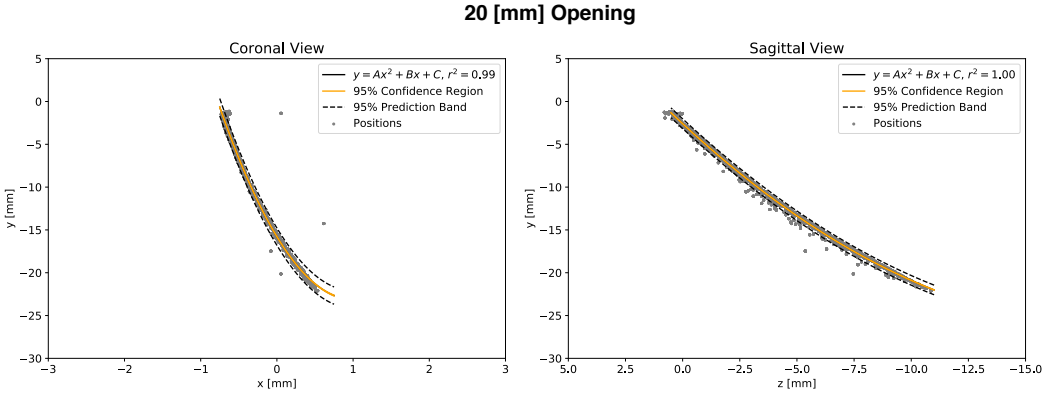

Figure 4.4: The coronal and sagittal view of the lower middle incisor trajectory at 20mm of opening during 30 open and close cycles.

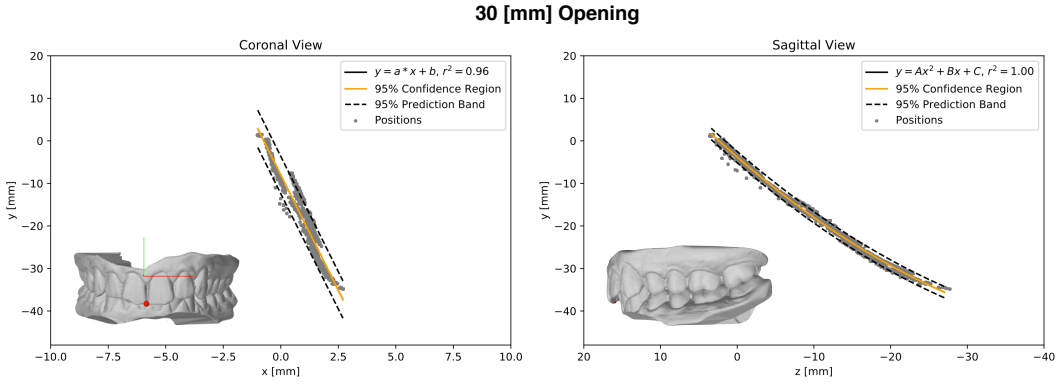

Figure 4.5: The coronal and sagittal view of the lower middle incisor trajectory at 30mm of opening during 30 open and close cycles.

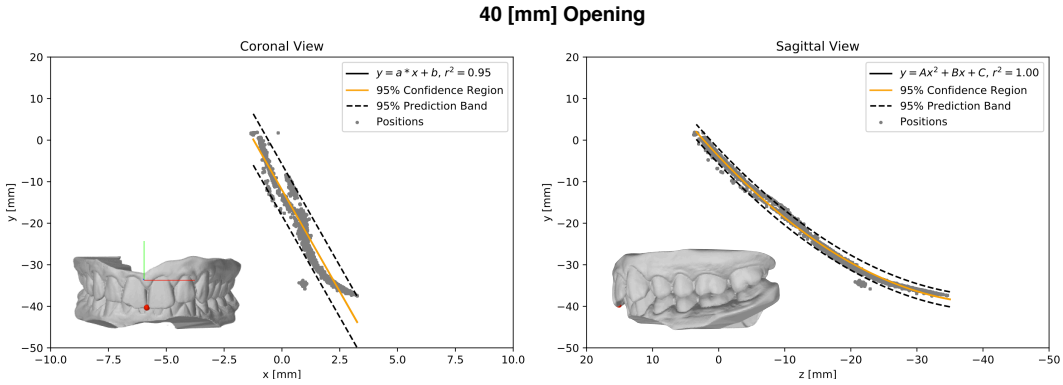

Figure 4.6: The coronal and sagittal view of the lower middle incisor trajectory at 40mm of opening during 30 open and close cycles.

For 10mm of opening, the coefficient of determination (r^2) was 0.98 and 1.00 on the coronal and sagittal planes respectively (Figure 4.3). A quadratic fit resulted in a high r^2 on the coronal plane and the deviation in X (medio-lateral) was 1.5mm. At 20mm of opening, the r^2 values were 0.99 and 1.00 on the coronal and sagittal planes (Figure 4.4). The X deviation of the lower middle incisor on the coronal plane was within 2mm. At 30mm of opening, the coronal X deviation increased to approximately 3mm and the r^2 on the coronal plane was 0.96 and 1.00 on the sagittal plane. At 40mm of opening, (Figure 4.5) the X deviation on the coronal plane was again approximately 3mm and from a Y range (-20mm,-40mm) the trajectory points deviate in the positive X direction. At 40mm of opening, (Figure 4.6) the r^2 values were 0.95 and 1.00 on the coronal and sagittal planes respectively. The X deviation on the coronal plane is just over 3mm with some outliers at Y < -35mm. Additionally, there is a significant curve shape that develops over 35mm of opening. The standard error (SE) at 10, 20, 30, and 40mm of opening are reported in Table 4.7 below.

Table 4.7: The iPhone® dynamic tracking accuracy (SE) at 10, 20, and 30mm of jaw opening.

Plane	**10 [mm]**	**20 [mm]**	**30 [mm]**	**40 [mm]**
Coronal	0.6502	0.5139	2.2365	3.1518
Sagittal	0.3225	0.2870	0.6771	0.9196

At 10mm and 20mm of opening the standard errors are 0.6502mm and 0.5139mm on the coronal plane, and 0.3225mm and 0.2870mm on the sagittal plane. At 30mm and 40mm the standard errors are 2.2365mm and 3.1518mm on the coronal plane, and 0.6771mm and 0.9196mm on the sagittal plane. For all opening distances, the standard error was lower on the sagittal plane suggesting better dynamic accuracy of the iPhone® on this plane. The standard error is $<$ 1mm on the coronal plane at 10mm and 20mm, but $>$ 2mm at 30mm and 40mm.

The key observation from this experiment is that the iPhone® dynamic tracking accuracy is approximately 1mm at 10mm and 20mm, and the accuracy deteriorates past 30mm of opening.

4.2 Virtual Simulation of Occlusal Interactions

Section 4.2.1 presents the contact pattern results of using the iPhone® tracking application to drive the motion for the simulated left, right, and protrusive excursions. We show the resulting mandible displacements of each excursion Figure 4.7 and the regions of tooth contact at their initial pose (maximal ICP) and final positions in Figures 4.8,4.9, and 4.10. We analyze the characteristics of the mandible trajectories and use inferences about the characteristics to help us to understand how realistic the created contact patterns are.

Section 4.2.2 presents the contact pattern trajectories of the left lateral excursion generated with the kinematic and dynamic simulations. We compare the initial and final pose contact patterns to determine if the presence of occlusal contact forces in the dynamic simulation changes the result.

4.2.1 Kinematic Simulation

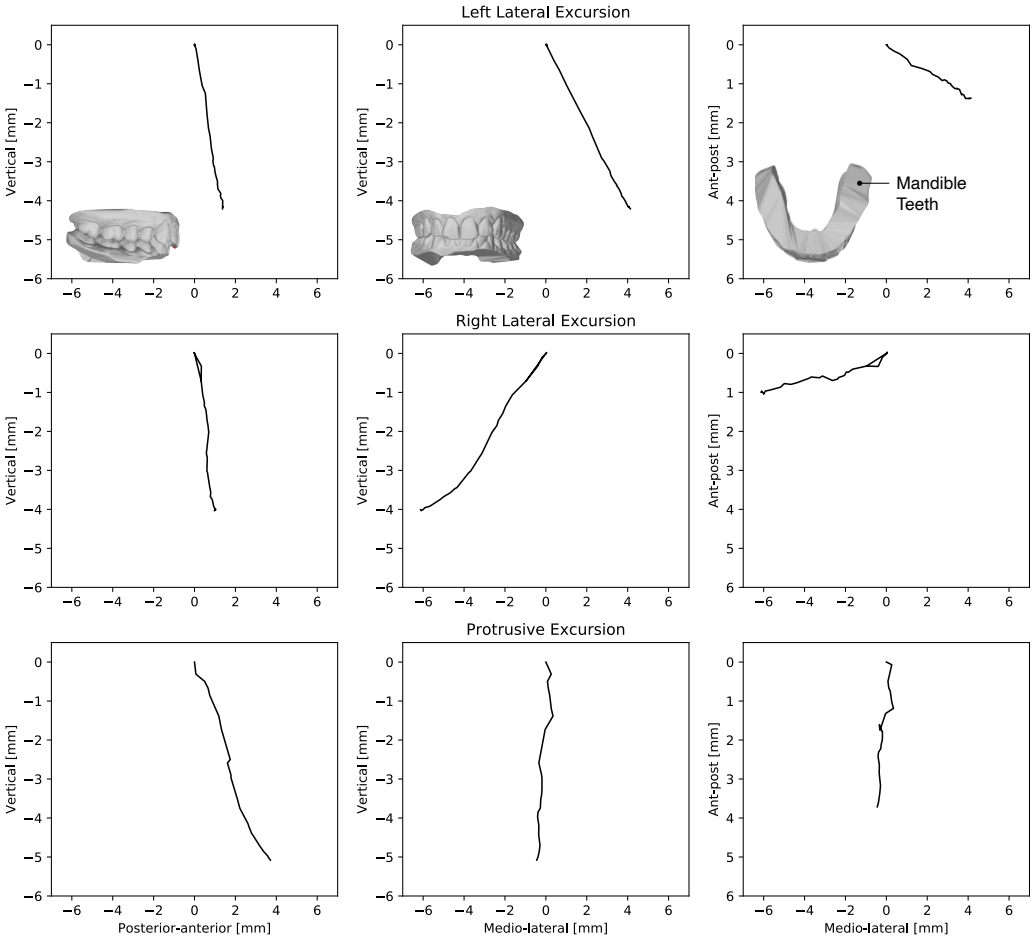

Figure 4.7: Kinematic (no occlusal forces) based excursion displacements of the lower middle incisor from maximal ICP to, left, protrusive, and right movement endpoints.

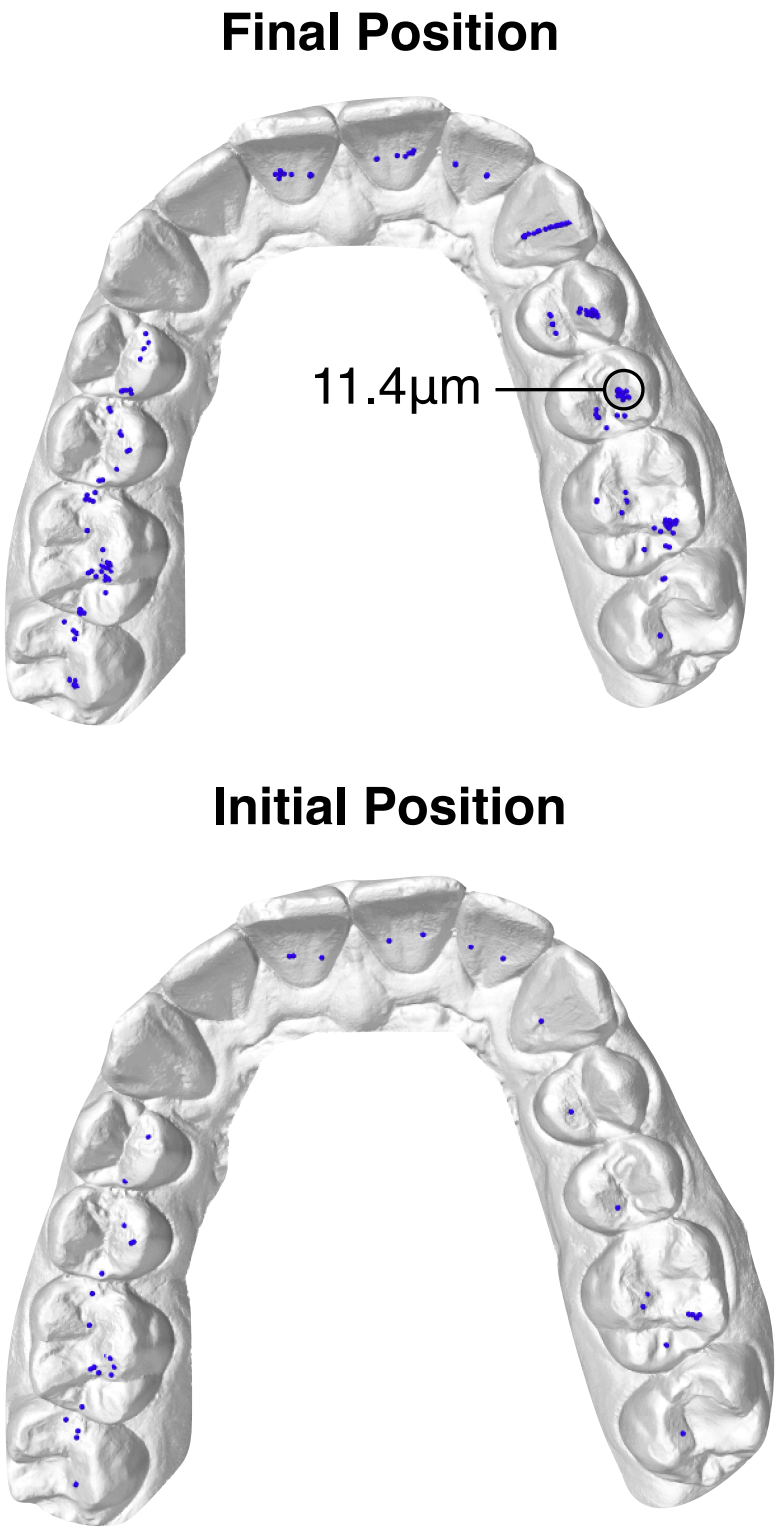

Figure 4.8: Left lateral excursion contact patterns on the maxilla virtual teeth at its initial pose (bottom) and final pose (top).

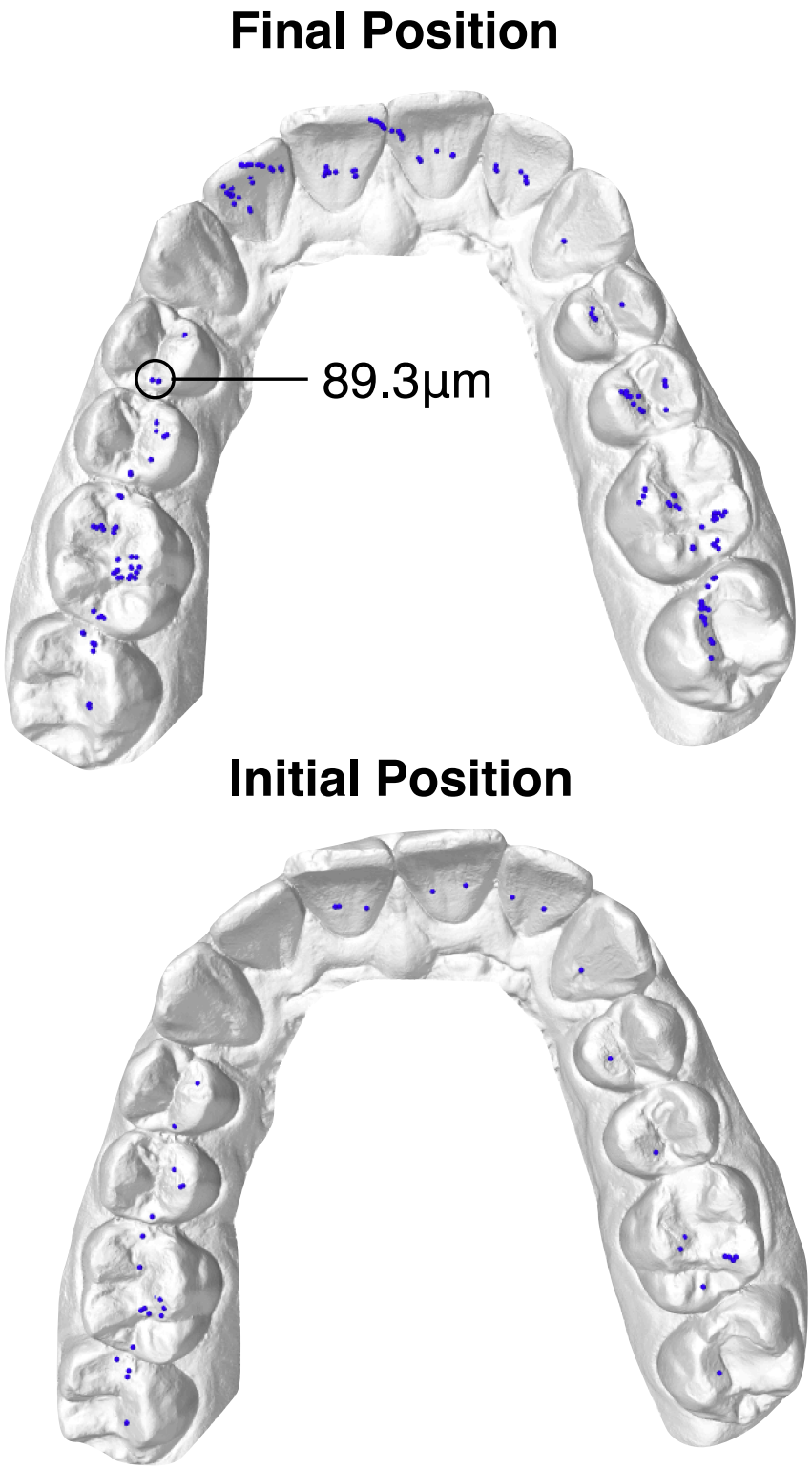

Figure 4.9: Right lateral excursion contact patterns on the maxilla virtual teeth at its initial pose (bottom) and its final pose (top).

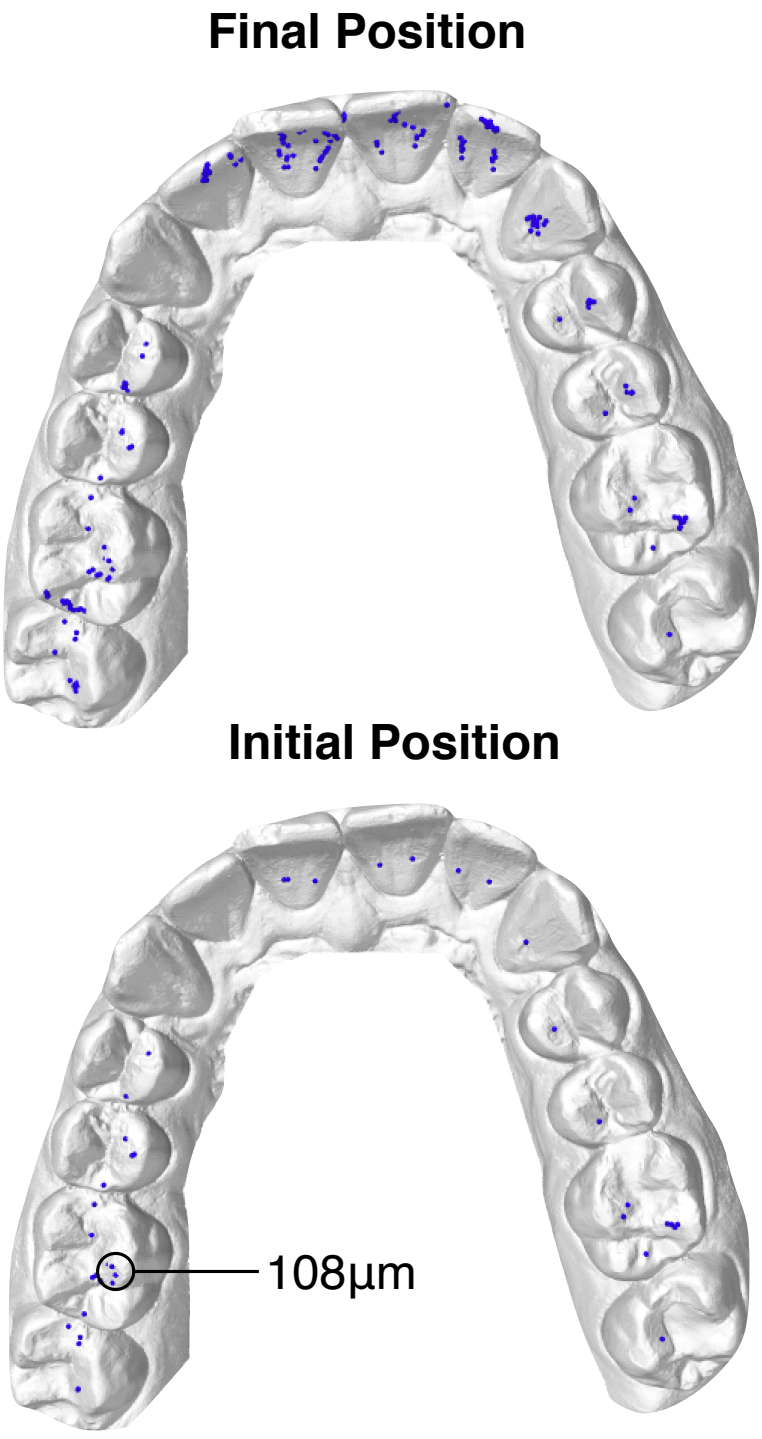

Figure 4.10: Protrusive excursion contact patterns on the maxilla virtual teeth at its initial pose (bottom) and its final pose (top).

The length of the left lateral excursion was approximately 4mm in the left lateral direction, in the superior-inferior plane, 4mm lateral and inferior in the coronal plane, approximately 4.3mm vertically, and 1.8mm posterior as show in Figure 4.7. The displacement path has some noticeable noise in the sagittal and coronal plane. The noise is considerably noticeable on the transverse plane. The right lateral excursion shows similar results to the left lateral excursion, but in the opposite direction and the final pose is 6mm medial, 4.3mm inferior, and 1mm anterior. The most prominent noise in the displacement plots is on the transverse plane. The protrusive excursion advances anterior 4mm and descends 5.2mm inferior, while deviating slightly medially 0.8mm from the midline.

The locations of tooth contacts in their initial and final positions are shown on the maxillary cast for the left, right, and protrusive excursions in Figures 4.8, 4.9, and 4.10. The points represent the centroid of the mesh interpenetration regions marked with a blue point. The interpenetration depth can be measured at each contact region and reported in real-time. An example is provided in Figures 4.8, 4.9, and 4.10. The initial pose of maximal ICP contact patterns on the maxillary cast is almost the same indicating that the iPhone® tracking application was capable of repeatedly capturing this pose. The final pose of the left lateral excursion (Figure 4.8) shows contact trajectories that slide along the left canine in the left lateral direction. The final pose of the right lateral excursion (Figure 4.9) shows a contact trajectory along the most anterior incisor in the right lateral excursion. The protrusive excursion shows a contact trajectory anteriorly on the 4 incisors with slight lateral deviation.

The first observation from this demonstration is that the plotted trajectories of each excursion do represent realistic jaw motion. The second observation is that the noise within the trajectories is prominent, and it may have a significant impact on reproducing reliable contact patterns. This is most likely due to the dynamic tracking error of the iPhone® application.

4.2.2 Dynamic Simulation

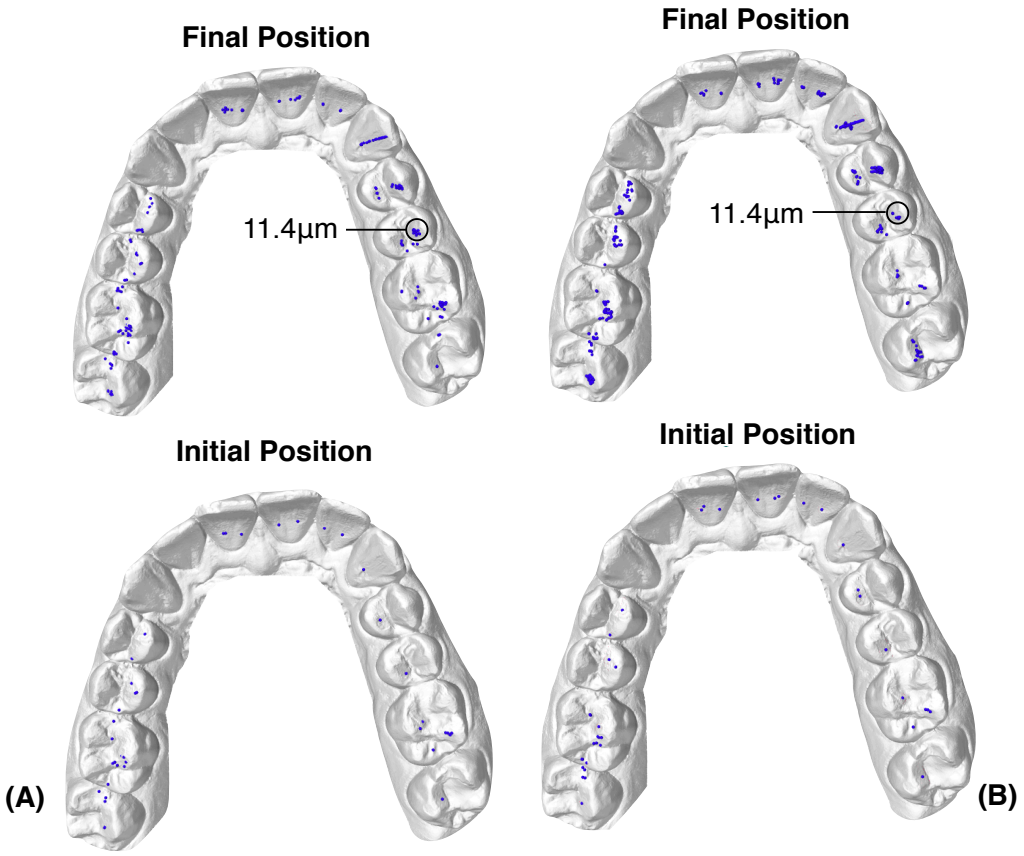

Figure 4.11: Left lateral excursion contact pattern on the maxilla virtual teeth at its initial pose (bottom) and its final pose (top) dynamically (B) and kinematically (A).

Figure 4.11 shows the difference between simulating occlusal contacts dynamically (occlusal forces) in Figure 4.11B, and kinematically (no occlusal forces) in Figure 4.11A.

The initial pose (maximal ICP) contact patterns are the same in the kinematic and dynamic contact simulations. The contact patterns at the final mandible pose are very similar between the two simulation methods, with the main difference being the contact trajectory seen for example on the left canine. In the kinematic simulation, the contact trajectory is close to a straight line, wherein the dynamic simulation some contact points deviate anterior and posterior of the contact trajectory. The cause for this is that occlusal forces applied to the mandibular teeth move it slightly during the excursion in the dynamic simulation. The final pose is the same in the kinematic and dynamic simulation indicating that the contact method did not drastically change resulting from the contact pattern.

The key observation from this demonstration is that the dynamic simulation of occlusal contact was able to adjust the mandible's trajectory to take the same path as the tracked result in the kinematic simulation while accounting for the tooth collisions to occur along the way.

Chapter 5

Discussion

5.1 Benchtop Evaluation Accuracy

In this section, we discuss the results from experiment 1, 2, and 3. The results are interpreted, the cause for the error is investigated, and a recommendation for the optimal conditions and settings for the iPhone® tracking system is given. Finally, we compare the optimal camera angle and distance tracking results to other commercial and fiducial marker mandible tracking systems.

5.1.1 Experiment 1

From Figure 4.1 the rotation and translation of the mandible dodecahedron compared to ${}^{DMax}_{DMand}\mathbf{T}'$ is significantly impacted by the angle of the camera. Theoretically, if at least 3 AprilTags were detected at all three angles we would have expected the static accuracy to be worse. This is because the iPhone® tracking application has trouble detecting AprilTags at sharp angles. Additionally, we would have expected the static accuracy to be worse as a function of camera distance. At increasing angle and distance, the static accuracy did not deteriorate. Instead, the static accuracy was best at the specific angle of 30° and distance of 100mm.

The position $(X_{err}, Y_{err}, Z_{err})$ and rotation $(\phi_{err}, \theta_{err}, \psi_{err})$ are lowest at 30° because the camera was able to identify more AprilTags on the upper and

lower dodecahedron compared to camera angles 0° and 60°. This trend was also observed when then the camera was moved further away from the dodecahedrons. At 100mm the most AprilTags were visible to the camera compared to 80mm and 120mm. For example, 4 AprilTags were visible on the maxillary dodecahedron and 5 AprilTags were visible on the mandibular dodecahedron at 30° and 100mm. Whereas, at 30° and 80mm only 3 AprilTags were visible on the maxillary and mandibular dodecahedrons. Another contributing factor to the best static accuracy being at 30° and 100mm was that the iPhone® camera was within its optimal focus range. When the iPhone® camera is too close or far from the dodecahedrons the quality of the captured images is lower and thus the detection of the AprilTags corners and centre points are less accurate.

When the same AprilTags were not continuously detected frame to frame, the standard deviation of the static accuracy increased because the ApriTag detection was not stable. This is a common problem with photometrically tracking binary fiducial markers. One way to solve this problem is to use a multi-camera capture system to ensure that all points on a 3D model are always visible to the camera. The downside of a multi-capture system is that it reduces the portability and affordability of the tracking system and increases the complexity of setup. Several algorithm improvements could be made to help address the stable tag detection issue and are discussed in Section 5.4.

5.1.2 Experiment 2

In this experiment, noise is added into the system by holding the iPhone® at the same angles and distances from experiment 1 (Figure 4.2). The goal was to evaluate the impact of the noise on the iPhone® 's ability to predict the pose of the mandible w.r.t. to maxilla dodecahedron. The outcome showed a slight increase in mean and standard deviation on the static accuracy of pose

estimation. Comparing the error when the camera was fixed to the tripod and when it was held by hand, the Z_{err} at 30° and 100mm increased from 0.287 ± 0.024mm to 0.730 ± 0.069mm (Table 4.2 and 4.5). This is a significant increase in pose estimation error and suggests that the added noise did have an impact on static accuracy. In a more realistic scenario, the iPhone® would most likely be fixed to a tripod when tracking a person's jaw motion which would most likely improve static accuracy. However, with the tracking harnesses fixed to the maxilla and mandible, some noise would be expected from the natural vibration of the head. This means that the static accuracy of the system would most likely fall closer to the results when the camera was held by hand.

From the results in experiment 1 and 2, it is reasonable to claim the tracking system is capable of achieving a static accuracy of $<$ 1mm and $<$ 5° error. This holds true when at least 4 AprilTags are detected on each dodecahedron and all 4 tags are detected frame to frame. Therefore, the recommended angle and distance to place the iPhone® to achieve the best static accuracy is at 30° and 100mm.

5.1.3 Experiment 3

The results from this experiment showed that the iPhone® jaw tracking application is capable of collecting repeatable trajectory data at all 4 opening distances (10, 20, 30, and 40mm). The linear regression of each open-close cycle had a $r^2 > 0.95$ on the coronal and sagittal planes, indicating the motions were repeatable with 95% confidence. When increasing opening distance, more variability began to surface. For example, from 20mm to 30mm the standard error increased more than 4 times from 0.5139mm to 2.2365mm on the coronal plane (Table 4.7). On the sagittal plane, the standard error more than doubled from 0.2870mm 0.6771mm. More specifically, the region where the most variability existed was from 20mm to 30mm of opening. This variability is most

likely caused by loss of AprilTag detection at points where the camera cannot see them or another AprilTag is detected in that region influencing the pose estimation. Past 30mm of opening AprilTag detection becomes stable again because the camera can see the same AprilTags frame to frame. Therefore, less error is observed and the pose estimation becomes more consistent.

The dynamic tracking of the iPhone® system performs best at 10-20mm of opening, which is within a suitable range for applications in prosthesis design. The repeatability and error becomes difficult to trust past 30mm of opening, most likely due to loss of AprilTag detection frame to frame. Additionally, during each open-close cycle, any fast movements of the mandible were difficult for the tracking system to identify and accuracy was most likely lost. Therefore, during the open-close cycles, the operator attempted to open and close the articulator with control to achieve stable tag detection. This is a present limitation of the system in all experiments and should be addressed for the tracking system to be more robust and reliable.

From the results in this experiment, it reasonable to claim that the iPhone® tracking application can repeatably capture motion on an arced path best from 0mm to 20mm with a standard error $<$ 1mm on both coronal and sagittal planes. Past 30mm of opening the dynamic tracking becomes unreliable and the error large on both the coronal and sagittal planes.

As an aside, it should be mentioned the jaw trajectories generated in this experiment do not represent true jaw opening biomechanics past 15-20mm due to the limitations of the articulator. A person's jaw ends its rotational opening phase around 15-20mm, and past this it begins to translate and rotate about the medio-lateral axis in the inferior direction. However, to evaluate the repeatability of the jaw tracking system a purely rotational motion was suitable for performing a linear regression analysis.

5.1.4 Comparison to Other Tracking System

Mostashiri *et al.* [78] present a planar fiducial marker system that uses two generic webcams fixed to a tripod and a custom dental appliance with a different type of binary fiducial marker called ArUco. Each tag is positioned 320mm perpendicular to each webcam. The ArUco tags had retroreflective markers affixed to their corners to compare tracking accuracy of their system to the commercial motion capture system Vicon (Oxford, United Kingdom). The reported static accuracy and dynamic error of the Vicon system is 0.15 ± 0.025mm and < 2mm respectively [92]. Mostashiri *et al.* performed 10 open-close cycles and the (X, Y, Z) position deviated slightly on the order of microns almost aligning perfectly. Therefore, demonstrating that they could achieve sub-millimetre static accuracy and < 2mm dynamic error.

Zoss *et al.* [15] also used ArUco markers, but attach them to the six faces of a 3D printed cube (similar to our dodecahedron). They fixed two cubes to the upper and lower surfaces of the teeth with small steel posts. They capture jaw motion with 8 *Xinea CB120MG* monochrome machine vision cameras capable of 4K imagery at 24 FPS. The system reports sub-millimetre accuracy at each node of a full mandible CT scan and mesh reconstruction over 9000 frames. They re-target their tracking data to a virtual jaw model that is constrained by captured motion. This means that from 30 points on each of the 4 cubes they are capable of estimating mesh vertices on the mandible within 1mm.

The Jaw Motion Analyzer (JMA-Zebris Medizintechnik, Isny/Allgäu, Germany) is specifically designed for tracking jaw motion for dentistry applications. It uses an ultrasonic method to track the pose of the mandible relative to the maxilla and is introduced in Section 2.3. The JMA system uses large headgear on the skull and transmitting probes on the mandible to track jaw motion.

It has a reported static and dynamic tracking error of less than 1mm [56], [93], [94].

Compared to the tracking systems above, the iPhone® tracking application is also able to achieve a static accuracy of < 1mm and $< 5°$. The dynamic standard error is < 1mm at 10mm to 20mm of the maximum opening but does not compete past 30mm of opening. Despite poor accuracy past 30mm of opening, the iPhone® tracking application static and dynamic accuracy is comparable to the other mentioned tracking systems. The iPhone® tracking application shows promise and we believe that it has the following advantages:

1. The iPhone® tracking system does not require multiple cameras to achieve sub-millimetre accuracy.

2. Other fiducial based systems require a camera calibration to determine its intrinsics, while the iPhone® is capable of accessing the camera intrinsics directly.

3. The tracking harness design can be customized to different types of oral anatomy and the fixation method does not interfere with the teeth during occlusion.

4. Being built on a mobile platform, the system is accessible to those that may not be able to afford expensive capture systems or do not have the equipment to implement other tracking methods.

5. Given the mobile nature of the iPhone® jaw motion can be captured anywhere.

Furthermore, the tracking system is not limited to dental applications because the pose of the dodecahedron w.r.t. the iPhone® camera is calculated independently of mandible motion. This means that it could be used as a proxy for tracking other objects in different tracking applications.

5.2 Virtual Simulation of Occlusal Interactions

In this section, we discuss the resulting generated contact patterns created with kinematic and dynamic simulation in ArtiSynth for a left, right, and protrusive excursion. We qualitatively evaluate if the tracked jaw motion aligns with the kinematic contact pattern results, interpret potential causes for noise in the trajectories, and present potential limitation of kinematic simulation. Finally, we compare the contact pattern results from the dynamic simulation with the kinematic one of the left lateral excursion and the advantages that dynamic simulation may have over the kinematic simulation.

5.2.1 Kinematic Simulation

The results demonstrate that it is feasible to recreate the motion (Figure 4.7) and contact patterns (Figures 4.8, 4.9, and 4.10) of a semi-adjustable articulator virtually. The noise presented in Figure 4.7 is most likely a result of temporal jittering. Temporal jittering is a result of intrinsic noise that comes from the dodecahedron tracking algorithm. When fewer points are available to the tracking algorithm more temporal jittering is present. This is a current limitation of using the iPhone® tracking application for kinematically simulating occlusal contacts virtually because it may hinder the resulting contact patterns. However, the resulting displacement traces did represent plausible mandibular motion and in turn, also created plausible contact patterns for each simulated excursion. There are methods to reduce temporal jittering and we discuss them in Section 5.4.

The left lateral excursion (Figure 4.8) contact trajectory pattern shows distinct canine guidance on the maxillary teeth at their final pose. Canine guidance disengages the posterior teeth during lateral excursions. The right lateral excursion (Figure 4.9) contact pattern does not show canine guidance.

Instead, the posterior teeth are disengaged by the right incisors and is often referred to as incisal guidance. In this case, the right mandibular canine has been shaved down by the maxillary incisor allowing it to pass by it during the right excursion without contact. In this case, if the excursion was more lateral than anterior we would expect contact to exist on the maxillary canine. The protrusive excursion in Figure 4.10 shows most contact on the incisors and the left canine. From the excursion trajectories captured with the iPhone® application, we know that the mandibular teeth deviated slightly in the left lateral direction. This is a likely explanation for why we see contact on the left canine and incisors.

At maximal ICP, the contact patterns for the left, right, and protrusive excursions are almost the same. This indicates that iPhone® jaw tracking application can accurately and repeatably capture maximal ICP and in turn allow it to be visualized virtually.

The limitation of the kinematic method is that due to tracking and measurement error occlusal surface of the teeth my interpenetrate too much and contacts between the teeth will be falsely identified. This becomes a large problem for prosthesis design because false identification of occlusal contact could yield a poor function dental prosthesis.

5.2.2 Dynamic Simulation

The dynamic simulation identifies interpenetration between the teeth and corrects the pose of the mandibular teeth by applying virtual forces to it with ArtiSynth's collision detection tool. Effectively, the dynamic simulation of occlusal contacts was able to reproduce the contact patterns of the left lateral excursion simulated kinematically. The initial pose (maximal ICP) had almost the same contact pattern. The only difference is that the dynamic simulation detected a few more points of contact on the anterior incisors. This most likely

was because in the kinematic simulation those contact points were too deep and not identified. Whereas, in the dynamic simulation the mandible pose was adjusted to correct for the deep interpenetration.

In the kinematic simulation, mandible motion is driven by the jaw motion captured by the iPhone® tracking application, while the dynamic simulation only used the initial and final pose to interpolate the trajectory. The interesting point here is that even though the dynamic simulation had less information about the exact trajectory between the initial and final pose it almost produced the same contact patterns. This suggests that the occlusal forces applied to the mandibular teeth almost produced the same mandibular trajectory. This of course depends on the patient specific anatomy and degree of deficit or deformity.

From the qualitative analysis, it is difficult to state if the dynamic simulation produces better results than the kinematic simulation mainly because the interpenetration adjustment may deviate from the true mandible trajectory. However, the dynamic simulation more accurately models tooth collision physics compared to the kinematic simulation. Additionally, the dynamic simulation may be favoured over the kinematic simulation because only the initial and final pose of the mandible is required for simulation. Finally, one advantage of using the iPhone® to determine the initial and final pose of the mandible for dynamic simulation is that it records patient specific poses compared to the semi-adjustable articulator.

5.3 Rehabilitation Applications

There are several applications for an iPhone® jaw tracking application with rehabilitation medicine. First, the motivation of this development is geared towards prosthesis planning for jaw reconstruction and more generally prosthodontics. The demonstration of using the jaw tracking application for kinematic

and dynamic contact simulations shows that both methods may be feasible to use in virtual prosthesis design. The articulator is limited in its capability to capture complex jaw motion and does not support an environment for integrating the system into a virtual prosthesis design workflow, whereas the iPhone® application does.

For example, in the case of a partial mandible restoration and fixed prosthesis treatment, one could collect pre-operative tracking data with the iPhone® application. With this data, a virtual prosthesis could be designed and optimized by simulating occlusal contact either kinematically or dynamically with the use of ArtiSynth. The prosthesis designer would have the flexibility to make adjustments to tooth position and orientation to refine the contact patterns the prosthesis design generates virtually and thus optimize its function.

Another application of the tracking system would be for functional simulation of jaw biomechanics. A growing field with the advancement of computer graphics, processing, and machine learning investigation of the mastication system is important in medical and neuromuscular control research. Software packages such as ArtiSynth have been used to demonstrate the capability of simulating the jaw musculoskeletal system with success. The simulations have even been able to incorporate the contributions of the tongue and skin soft tissue on oral function [95]–[97]. One method for reproducing dynamic chewing motion involves motion capture, and the iPhone® tracking application provides an affordable alternative to more expensive motion capture systems. This is valuable because it may enable some to investigate and implement function jaw biomechanical modelling when motion capture systems are not always considered fundamental equipment. Functional simulation of chewing, swallowing, and speech is the direction that surgical design and simulation is headed.

Therefore, an accurate and affordable jaw tracking system is a valuable contribution to the field and may encourage further research.

Since the tracking system is mobile, this brings forth an interesting opportunity for home monitoring of chewing, swallowing, and speech rehabilitation progress. A scenario could be envisioned where a clinician could work with a patient on specific exercises that would help them regain chewing capability. Exercises could be monitored remotely and real-time feedback provided to patients. The application of home monitoring is of interest to the rehabilitation community because quantitative measures of improved function may help increase patient self confidence and motivation, impact lifestyle choices, and may positively influence quality of life [98]–[100].

Extending past jaw reconstruction and oral rehabilitation applications, the tracking system also could be used as an affordable AR and Virtual Reality (VR) application for tracking real world objects by attaching the dodecahedron to them. The all in one nature of the iPhone® application may provide a quick method of evaluating tracking applications without complicated setup. Mobile phone AR and tracking applications are emerging quickly, some applications include, writing and drawing in 2D and 3D [13], human body positioning [101], and even image based dietary assessment [102]. We feel that the iPhone® tracking application is a valuable contribution to AR and VR research because of its ability to accurately track the complex motion of the mandible as well other aspects of the anatomy.

5.4 Limitations and Future Work

We structure the limitations and suggestions for future work in order of importance based on what we believe will improve the performance and robustness of the jaw tracking application. Implementing these suggestions for future would take the iPhone® one step closer to being used clinically for functional assessment a dental prosthesis.

Bad Tag Detection

During tracking, there often is noise introduced into the system that will result in tags to flicker at high frequency. This impacts the accuracy of the tracking system and should be addressed to improve the reliability of the system. One approach would be to sample previous frames and detect which ones are detected the most frequently to remove flickering AprilTags. Another approach would be to measure the Euclidean distance of each AprilTag centre point to its corresponding corner points. With this measure, points that are too close to each other could be excluded from the pose estimation algorithm.

The other instance when poor detection directly impacts the stability and accuracy of tracking is when the AprilTag detection algorithm estimates the incorrect direction of the Z-axis relative to the camera. This is an issue with fiducial tag detection and pose estimation [75], [85]. Essentially, an optical illusion is presented where the camera cannot determine the correct orientation of the tag. If this happens, the detected corner points will not correspond with their 3D points and generate an error in the pose estimation. One know method for solving this ambiguity problem is the use of an RGB-D or depth camera to correctly determine the orientation of the Z-axis [103]. Another method is to use a multi-capture system so that the tag can be seen from two preservatives and the case where the Z-axis is aligned with the 3D model can be selected.

Finally, loss of tag detection during fast movements of the object being tracked is a limitation of the current tracking system and should be addressed to extend its application. The most notable algorithm used to solve this problem is called Lucas-Kanade optical flow. It estimates the position of key points in an image frame by calculating the velocity of the points from previous frames [104]. This algorithm is common in computer vision applications and it should be noted that VISP provides software and examples to help implement the concept [14].

Dodecahedron Calibration

The tracking system does not include any calibration steps which impacts the performance of the iPhone® tracking application. The tracking algorithm is adapted from Wu *et al.* [13] and they do include a dodecahedron calibration to account for error of placing the fiducial markers on each face of the dodecahedron. This improved the accuracy of the tracking substantially. The calibration requires several images captured from the camera to perform a bundle adjustment procedure.

Given a set of measured image feature locations and corresponding 3D world features, the goal of a bundle adjustment is to find the 3D point positions and camera parameters that minimize the reprojection error similar to the pose estimation in Section 3.8. The difference is that there is more data and a better determination of the dodecahedron pose can be calculated. Once calculated, the pose of one AprilTag is fixed, and the rest of the AprilTags on the dodecahedron are adjusted until the error between the dodecahedron pose and each AprilTag is as small as possible. The bundle adjustment would update the positions of the AprilTags on the 3D model to account for 3D printer and AprilTag placement error.

Dense Pose Refinement

The dodecahedron pose detection algorithm works well by solving the PnP problem. However, there is a visible temporal jitter that exists when the pose of the mandible is visualized in ArtiSynth. A method for removing this temporal jitter, is to use the dense information or gray scale values of the observed AprilTags. The gray scale values of the AprilTag collected by the camera could be compared to their expected values on the 3D model. For example, a set of 100 points could be sampled on the 3D model to get their position relative the the dodecahedron ${}^{J}\mathbf{x}_i$ along with their associated colors c_i. With the 3D points ${}^{J}\mathbf{x}_i$ in the jaw frame $\{\mathrm{J}\}$ and the corresponding projected points on the image plane $\{\mathcal{I}_C\}$, a non-linear least squares problem is formulated as:

$$E_r({}^{\mathbf{C}}_{\mathbf{J_t}}\mathbf{T}) = \sum_i \left\| \mathbf{c}_i - \mathcal{I}_C \left(Proj \left({}^{\mathbf{C}}_{\mathbf{J_t}}\hat{\mathbf{T}} \cdot {}^{J}\mathbf{x}_i \right) \right) \right\|_2^2 \tag{5.1}$$

where $Proj\,(\cdot)$ represents the camera projection of the jaw frame $\{\mathrm{J}\}$ points onto the image plane via the prospective project camera model. The dodecahedron pose then could be refined by minimizing the difference between grayscale values with the initial pose estimation ${}^{\mathbf{C}}_{\mathbf{J_t}}\hat{\mathbf{T}}$ from Section 3.8. This method has been shown to remove most jitter from the pose estimation and would improve the stability of tracking [13], [15].

Utilizing Mobile Phone Resources

Ideally, to get the best estimation of the AprilTag corners and centre points the resolution of the camera should be at its highest performance settings. In this case, the iPhone® X is capable of 4K resolution at 30 FPS. Unfortunately, due to the processing power required for AprilTag detection, and solving the pose estimation problem, the CPU cannot meet these demands. The iPhone® did produce very accurate results at 4K resolution, but it could only capture at about 4 FPS with an AprilTag decimation of 4. This is not feasible for

tracking jaw motion because the frame rate is too slow and the camera would not be able to capture the fast motions of the mandible.

To improve the capture precision it is recommended that the capture frames are cropped to the target to reduce the search region and detection time. Once the initial pose of the dodecahedron is estimated, its position on the image plane could be calculated and then the incoming frames cropped to narrow the search region for AprilTag detection. Once detected, the pose could then be estimated by solving the PnP problem and rendered onto the iPhone® screen.

The second recommendation to increase speed is to do image pre-processing on the iPhone® Graphics Processing Unit (GPU) instead of the CPU. Image processing on the GPU would significantly speed up the frame rate because it is faster at doing processes such as grayscale conversion, image segmentation, gradient calculation, and rendering. Image processing on the GPU is faster because image data is represented as a texture that contains points and lines that the GPU can apply mathematical operations to simultaneously instead of pixel by pixel like the CPU.

The last recommendation is to use the TrueDepth® , camera to get a better estimation of the AprilTag corner and centre distance from the camera. The TrueDepth® camera can only be enabled in an ARFaceTracking configuration and was not used for tag detection. Theoretically possible, the TrueDepth® camera was not used because an issue was faced with correctly processing the frame data into the correct format required by VISP.

Tracking Harness Registration

The tracking harness registration is important for the tracking algorithm to approximate the pose of the dodecahedrons. Therefore, the tracking harness must be securely fixed to the mandible and maxilla to get the best results.

An improvement that could be made would be to use of the iPhone's® face tracking technology and a CT scan of the skull and mandible. With this data, a relationship between the skull and the dodecahedrons could be made and the position and orientation of the dodecahedrons adjusted on the 3D model to more closely align with 3D printed tracking harness.

Chapter 6

Conclusion

In this thesis, the development of a mobile jaw tracking application is presented to track the 6 DoF position and orientation of the mandible w.r.t. the maxilla. In Chapter 1 the motivation for the development of the mobile tracking system is identified and its application contextualized with the effort to change the prosthesis planning workflow to become more digital. In Chapter 2, the state-of-the-art in the restoration of chewing function after head and neck cancer is reviewed, the use articulators in restorative dentistry are reviewed, mandibular motion tracking systems reviewed, and techniques for computation modelling and simulation of occlusal dynamics reviewed. Next, in Chapter 3 the specifics of the jaw tracking application development are described, the method for evaluating the static accuracy and dynamic repeatability are defined, and the method used for demonstrating how the jaw tracking application can be used to simulation occlusal interactions kinematically (without forces) and dynamically (with forces). Chapter 4 presents the results of the static accuracy, dynamic repeatability, and the contact patterns of three mandible tooth excursions. Finally, Chapter 5 interprets the results of the static and dynamic analysis and of how the dynamic simulation results could be used for virtual prosthesis design. Rehabilitation applications are discussed and the limitations of the system are identified with recommendations for future work

and improvements to the iPhone application. The key contributions of this thesis are:

- We developed an accurate and low cost mobile mandibular jaw tracking application that has the potential to reliably achieve sub-millimetre tracking accuracy.
- We developed an all in one 6 DoF tracking application that does not require specialized equipment or expertise to record mandibular motion.
- We developed a real-time mandibular tracking visualization application that can accept mandible trajectory information over a local WiFi network from the iPhone® application.
- We developed a low cost, 3D printed, and patient specific mandible and maxilla tracking harness for tracking mandible pose.
- We demonstrated that the iPhone® tracking application can be used to recreate realistic occlusal contacts kinematically and dynamically.

The work in this thesis presents the first developments of a mobile smartphone application for tracking mandibular motion that can achieve sub-millimetre accuracy at a camera angle of 30°. The mobile smartphone tracking application addresses the issue of recording patient specific mandibular motion and has the potential to be used by a broader population. In addition, the iPhone® application was able to be used for driving kinematic and dynamic simulation of occlusal interactions virtually. There are still limitations to overcome; (1) optimization of mobile phone resources, (2) implementation of a dodecahedron calibration, (3) improvement of tracking harness registration, (4) reduction of temporal jittering, (5) and identification of bad AprilTag detection. In the future, the hope of this development is that it continues and careful assessment

of how the iPhone® tracking application and virtual occlusal contact simulation could best assist prosthesis design and potentially more broadly and in other domains within medicine and rehabilitative science.

References

[1] L. Infante, B. Yilmaz, E. McGlumphy, and I. Finger, "Fabricating complete dentures with cad/cam technology," *The Journal of prosthetic dentistry*, vol. 111, no. 5, pp. 351–355, 2014. 1

[2] M. S. Bilgin, A. Erdem, O. S. Aglarci, and E. Dilber, "Fabricating complete dentures with cad/cam and rp technologies," *Journal of Prosthodontics*, vol. 24, no. 7, pp. 576–579, 2015. 1

[3] E. Solaberrieta, O. Etxaniz, R. Minguez, J. Muniozguren, and A. Arias, "Design of a virtual articulator for the simulation and analysis of mandibular movements in dental cad/cam," in *Proceedings of the 19th CIRP Design Conference–Competitive Design*, Cranfield University Press, 2009. 1

[4] A. Dawood, B. M. Marti, V. Sauret-Jackson, and A. Darwood, "3d printing in dentistry," *British dental journal*, vol. 219, no. 11, pp. 521–529, 2015. 1

[5] M. T. Kattadiyil, Z. Mursic, H. AlRumaih, and C. J. Goodacre, "Intraoral scanning of hard and soft tissues for partial removable dental prosthesis fabrication," *The Journal of prosthetic dentistry*, vol. 112, no. 3, pp. 444–448, 2014. 1

[6] J. R. Strub, E. D. Rekow, and S. Witkowski, "Computer-aided design and fabrication of dental restorations: Current systems and future possibilities," *The Journal of the American Dental Association*, vol. 137, no. 9, pp. 1289–1296, 2006. 1

[7] M. Raja'a and F. Farid, "Computer-based technologies in dentistry: Types and applications," *Journal of dentistry (Tehran, Iran)*, vol. 13, no. 3, p. 215, 2016. 1

[8] R. Bhambhani, J. Bhattacharya, and S. K. Sen, "Digitization and its futuristic approach in prosthodontics," *The Journal of Indian Prosthodontic Society*, vol. 13, no. 3, pp. 165–174, 2013. 1

[9] A. Bisler, U. Bockholt, B. Kordass, M. Suchan, and G. Voss, "The virtual articulator.," *International journal of computerized dentistry*, vol. 5, no. 2-3, pp. 101–106, 2002. 2, 15

[10] J. H. Kwon, S. Im, M. Chang, J.-E. Kim, and J.-S. Shim, "A digital approach to dynamic jaw tracking using a target tracking system and a structured-light three-dimensional scanner," *Journal of prosthodontic research*, vol. 63, no. 1, pp. 115–119, 2019. 2, 18

[11] I. Stavness, A. Hannam, D. Tobias, and X. Zhang, "Simulation of dental collisions and occlusal dynamics in the virtual environment," *Journal of oral rehabilitation*, vol. 43, no. 4, pp. 269–278, 2016. 2, 21, 42, 52, 54

[12] B. Kordaß and C. Gärtner, "The virtual articulator—concept and development of vr-tools to analyse the dysfunction of dental occlusion," in *International Congress Series*, Elsevier, vol. 1230, 2001, pp. 689–694. 2, 14

[13] P.-C. Wu, R. Wang, K. Kin, C. Twigg, S. Han, M.-H. Yang, and S.-Y. Chien, "Dodecapen: Accurate 6dof tracking of a passive stylus," in *Proceedings of the 30th Annual ACM Symposium on User Interface Software and Technology*, 2017, pp. 365–374. 3, 30, 33, 81, 83, 84

[14] E. Marchand, H. Uchiyama, and F. Spindler, "Pose estimation for augmented reality: A hands-on survey," *IEEE transactions on visualization and computer graphics*, vol. 22, no. 12, pp. 2633–2651, 2015. 3, 83

[15] G. Zoss, D. Bradley, P. Bérard, and T. Beeler, "An empirical rig for jaw animation," *ACM Transactions on Graphics (TOG)*, vol. 37, no. 4, pp. 1–12, 2018. 3, 19, 30, 75, 84

[16] J. E. Lloyd, I. Stavness, and S. Fels, "Artisynth: A fast interactive biomechanical modeling toolkit combining multibody and finite element simulation," in *Soft tissue biomechanical modeling for computer assisted surgery*, Springer, 2012, pp. 355–394. 3

[17] C. S. of Otolaryngology - Head and N. Surgery. (). Head and neck cancer, [Online]. Available: `https://www.entcanada.org/education/general-public/public-information-sheets-2/head-neck/head-neck-cancer/`. 7

[18] K. S. Chua, S. K. Reddy, M.-C. Lee, and R. B. Patt, "Pain and loss of function in head and neck cancer survivors," *Journal of pain and symptom management*, vol. 18, no. 3, pp. 193–202, 1999. 7

[19] P. Ravasco, I. Monteiro-Grillo, P. M. Vidal, and M. Camilo, "Nutritional deterioration in cancer: The role of disease and diet," *Clinical oncology*, vol. 15, no. 8, pp. 443–450, 2003. 7

[20] U. Tschiesner, S. Rogers, U. Harreus, A. Berghaus, and A. Cieza, "Content comparison of quality of life questionnaires used in head and neck cancer based on the international classification of functioning, disability and health: A systematic review," *European Archives of Oto-Rhino-Laryngology*, vol. 265, no. 6, pp. 627–637, 2008. 7

[21] D. A. Hidalgo, "Fibula free flap: A new method of mandible reconstruction," *Plastic and reconstructive surgery*, vol. 84, no. 1, pp. 71–79, 1989. 7

[22] ——, "Aesthetic improvements in free-flap mandible reconstruction," *Plast Reconstr Surg*, vol. 88, no. 4, pp. 574–585, 1991. 7

[23] M. L. Urken, D. Buchbinder, P. D. Costantino, U. Sinha, D. Okay, W. Lawson, and H. F. Biller, "Oromandibular reconstruction using microvascular composite flaps: Report of 210 cases," *Archives of otolaryngology–head & neck surgery*, vol. 124, no. 1, pp. 46–55, 1998. 7

[24] G. Kokosis, R. Schmitz, D. B. Powers, and D. Erdmann, "Mandibular reconstruction using the free vascularized fibula graft: An overview of different modifications," *Archives of plastic surgery*, vol. 43, no. 1, p. 3, 2016. 7, 17

[25] R. W. Gilbert, "Reconstruction of the oral cavity; past, present and future," *Oral Oncology*, vol. 108, p. 104 683, 2020. 8

[26] J. A. L. Tang, J. M. Rieger, and J. F. Wolfaardt, "A review of functional outcomes related to prosthetic treatment after maxillary and mandibular reconstruction in patients with head and neck cancer.," *International Journal of Prosthodontics*, vol. 21, no. 4, 2008. 8, 11

[27] K. Fueki, K. Kimoto, T. Ogawa, and N. R. Garrett, "Effect of implant-supported or retained dentures on masticatory performance: A systematic review," *Journal of Prosthetic Dentistry*, vol. 98, no. 6, pp. 470–477, 2007. 8

[28] M. Rana, R. Warraich, H. Kokemüller, J. Lemound, H. Essig, F. Tavassol, A. Eckardt, and N.-C. Gellrich, "Reconstruction of mandibular defects-clinical retrospective research over a 10-year period," *Head & neck oncology*, vol. 3, no. 1, p. 23, 2011. 8

[29] P.-I. Branemark, "Osseointegration and its experimental background," *J prosthet Dent*, vol. 50, pp. 399–410, 1983. 8

[30] I. M. Zlotolow, J. M. Huryn, J. D. Piro, E. Lenchewski, and D. A. Hidalgo, "Osseointegrated implants and functional prosthetic rehabilitation in microvascular fibula free flap reconstructed mandibles," *The American journal of surgery*, vol. 164, no. 6, pp. 677–681, 1992. 8

[31] M. M. Hanasono and R. J. Skoracki, "Computer-assisted design and rapid prototype modeling in microvascular mandible reconstruction," *The Laryngoscope*, vol. 123, no. 3, pp. 597–604, 2013. 8

[32] H. Logan, J. Wolfaardt, P. Boulanger, B. Hodgetts, and H. Seikaly, "Exploratory benchtop study evaluating the use of surgical design and simulation in fibula free flap mandibular reconstruction," *Journal of Otolaryngology-Head & Neck Surgery*, vol. 42, no. 1, p. 42, 2013. 8

[33] Y. Wang, H. Zhang, S. Fan, D. Zhang, Z. Huang, W. Chen, J. Ye, and J. Li, "Mandibular reconstruction with the vascularized fibula flap: Comparison of virtual planning surgery and conventional surgery," *International Journal of Oral and Maxillofacial Surgery*, vol. 45, no. 11, pp. 1400–1405, 2016. 8

[34] M. Qaisi, H. Kolodney, G. Swedenburg, R. Chandran, and R. Caloss, "Fibula jaw in a day: State of the art in maxillofacial reconstruction," *Journal of Oral and Maxillofacial Surgery*, vol. 74, no. 6, 1284–e1, 2016. 8

[35] D. C. Sukato, D. Hammer, W. Wang, T. Shokri, F. Williams, and Y. Ducic, "Experience with "jaw in a day" technique," *Journal of Craniofacial Surgery*, vol. 31, no. 5, pp. 1212–1217, 2020. 8

[36] L. Ciocca, G. Lizio, P. Baldissara, A. Sambuco, R. Scotti, and G. Corinaldesi, "Prosthetically cad-cam–guided bone augmentation of atrophic jaws using customized titanium mesh: Preliminary results of an open prospective study," *Journal of Oral Implantology*, vol. 44, no. 2, pp. 131–137, 2018. 8

[37] H. Seikaly, S. Idris, R. Chuka, C. Jeffery, A. Dzioba, F. Makki, H. Logan, D. A. O'Connell, J. Harris, K. Ansari, *et al.*, "The alberta reconstructive technique: An occlusion-driven and digitally based jaw reconstruction," *The Laryngoscope*, vol. 129, S1–S14, 2019. 9, 10

[38] M. Johal, D. Leinkram, C. Wallace, and J. Clark, "The sydney modified alberta reconstruction technique (sm-art) for dental rehabilitation following mandibulectomy or maxillectomy," *International Journal of Oral and Maxillofacial Surgery*, 2020. 9

[39] J. Ludlow, L. Davies-Ludlow, and S. Brooks, "Dosimetry of two extraoral direct digital imaging devices: Newtom cone beam ct and orthophos plus ds panoramic unit," *Dentomaxillofacial Radiology*, vol. 32, no. 4, pp. 229–234, 2003. 9

[40] J. K. Mah, R. A. Danforth, A. Bumann, and D. Hatcher, "Radiation absorbed in maxillofacial imaging with a new dental computed tomography device," *Oral Surgery, Oral Medicine, Oral Pathology, Oral Radiology, and Endodontology*, vol. 96, no. 4, pp. 508–513, 2003. 9

[41] M. Kumar, M. Shanavas, A. Sidappa, and M. Kiran, "Cone beam computed tomography-know its secrets," *Journal of international oral health: JIOH*, vol. 7, no. 2, p. 64, 2015. 9

[42] F.-S. Yuan, Y.-C. Sun, Y. Wang, and P.-J. Lü, "Accuracy evaluation of a new three-dimensional reproduction method of edentulous dental casts, and wax occlusion rims with jaw relation," *International journal of oral science*, vol. 5, no. 3, pp. 155–161, 2013. 10

[43] R. S. Squier, "Jaw relation records for fixed prosthodontics," *Dental Clinics*, vol. 48, no. 2, pp. 471–486, 2004. 10

[44] K. J. Ferro, S. M. Morgano, C. F. Driscoll, M. A. Freilich, A. D. Guckes, K. L. Knoernschild, T. J. McGarry, and M. Twain, "The glossary of prosthodontic terms," 2018. 11

[45] D. L. Mitchell and N. D. Wilkie, "Articulators through the years. part i. up to 1940," *The Journal of prosthetic dentistry*, vol. 39, no. 3, pp. 330–338, 1978. 12

[46] P. Batra, "Articulator and facebow: Review of literature and history of articulators.," *Journal of Oral Health & Community Dentistry*, vol. 7, no. 1, 2013. 12

[47] R. L. Engelmeier, D. M. Belles, and E. N. Starcke, "The history of articulators: The contributions of rudolph l. hanau and his company—part i," *Journal of Prosthodontics: Implant, Esthetic and Reconstructive Dentistry*, vol. 19, no. 5, pp. 409–418, 2010. 12

[48] G. Bergström, *On the Reproduction of Dental Articulation by Means of Articulators: A Kinematic Investigation*. publisher not identified, 1950. 12

[49] L. A. Weinberg, "An evaluation of basic articulators and their concepts: Part i. basic concepts," *Journal of Prosthetic Dentistry*, vol. 13, no. 4, pp. 622–644, 1963. 12

[50] F. Nesi, L. Nishimori, C. Silva, F. Marson, S. Saabio, and G. Correea, "Semi-adjustable articulators," *J Clin Surg Dent*, vol. 1, pp. 14–21, 2014. 13

[51] W. Sutradhar, S. K. Mishra, R. Chowdhary, *et al.*, "Uses, accuracy and limitations of semiadjustable articulators in dentistry: A systematic review," *Tanta Dental Journal*, vol. 16, no. 3, p. 121, 2019. 14

[52] C. Sadowsky and E. A. BeGole, "Long-term status of temporomandibular joint function and functional occlusion after orthodontic treatment," *American Journal of Orthodontics*, vol. 78, no. 2, pp. 201–212, 1980. 14

[53] L. Maestre-Ferrın, J. Romero-Millán, D. Peñarrocha-Oltra, and M. Peñarrocha-Diago, "Virtual articulator for the analysis of dental occlusion: An update," *Medicina oral, patologia oral y cirugia bucal*, vol. 17, no. 1, e160, 2012. 14, 20

[54] E. Solaberrieta, J. R. Otegi, R. Mınguez, and O. Etxaniz, "Improved digital transfer of the maxillary cast to a virtual articulator," *The Journal of prosthetic dentistry*, vol. 112, no. 4, pp. 921–924, 2014. 14

[55] P. R. Koralakunte and M. Aljanakh, "The role of virtual articulator in prosthetic and restorative dentistry," *Journal of clinical and diagnostic research: JCDR*, vol. 8, no. 7, ZE25, 2014. 14, 15

[56] P. Venezia, T. Joda, and H.-L. Wang, "Virtual articulators and virtual mounting procedures: Where do we stand?," 14, 76

[57] Y. Zhang, I. Sailer, and B. R. Lawn, "Fatigue of dental ceramics," *Journal of dentistry*, vol. 41, no. 12, pp. 1135–1147, 2013. 15

[58] R. A. Delgado-Ruiz, J. L. Calvo-Guirado, and G. E. Romanos, "Effects of occlusal forces on the peri-implant-bone interface stability," *Periodontology 2000*, vol. 81, no. 1, pp. 179–193, 2019. 15

[59] C. E. Luce, "The movements of the lower jaw," *The Boston Medical and Surgical Journal*, vol. 121, no. 1, pp. 8–11, 1889. 15

[60] K. D. Rudd, R. M. Morrow, and M. D. Jendresen, "Fluorescent photoanthropometry: A method for analyzing mandibular motion," *Journal of Prosthetic Dentistry*, vol. 21, no. 5, pp. 495–505, 1969. 15

[61] A. H. Abdi, A. G. Hannam, I. K. Stavness, and S. Fels, "Minimizing fiducial localization error using sphere-based registration in jaw tracking," *Journal of biomechanics*, vol. 68, pp. 120–125, 2018. 16

[62] Y. Tanaka, T. Yamada, Y. Maeda, and K. Ikebe, "Markerless three-dimensional tracking of masticatory movement," *Journal of biomechanics*, vol. 49, no. 3, pp. 442–449, 2016. 16, 19

[63] S. Madhavan, M. Dhanraj, and A. R. Jain, "Methods of recording mandibular movements—a review," *Drug Invent. Today*, vol. 10, p. 1259, 2018. 17

[64] R. Enciso, A. Memon, D. Fidaleo, U. Neumann, and J. Mah, "The virtual craniofacial patient: 3d jaw modeling and animation," *Studies in health technology and informatics*, vol. 94, pp. 65–71, Feb. 2003. DOI: 10.3233/978-1-60750-938-7-65. 17

[65] U. Soboļeva, L. Lauriņa, and A. Slaidiņa, "Jaw tracking devices—historical review of methods development. part i," *Stomatologija*, vol. 7, no. 3, pp. 67–71, 2005. 17

[66] P. Tsolka and H. Preiskel, "Kinesiographic and electromyographic assessment of the effects of occlusal adjustment therapy on craniomandibular disorders by a double-blind method," *The Journal of prosthetic dentistry*, vol. 69, no. 1, pp. 85–92, 1993. 17

[67] E. Kazazoglu, M. R. Heath, A. M. Ferman, and G. A. Davis, "Recording mandibular movement: Technical and clinical limitations of the sirognathograph.," *Journal of orofacial pain*, vol. 8, no. 2, 1994. 17

[68] C. Chen, C. Lin, Y. Chen, S. Hong, and T. Lu, "A method for measuring three-dimensional mandibular kinematics in vivo using single-plane fluoroscopy," *Dentomaxillofacial Radiology*, vol. 42, no. 1, pp. 95 958 184–95 958 184, 2013. 17

[69] P. Howell, S. Ellis, C. Johnson, I. Watson, and I. Klineberg, "The recording and analysis of emg and jaw tracking. ii. reproducibility of jaw tracking," *Journal of Oral Rehabilitation*, vol. 20, no. 1, pp. 33–43, 1993. 18

[70] H. Kato and M. Billinghurst, "Marker tracking and hmd calibration for a video-based augmented reality conferencing system," in *Proceedings 2nd IEEE and ACM International Workshop on Augmented Reality (IWAR'99)*, IEEE, 1999, pp. 85–94. 18

[71] M. Fiala, "Artag, a fiducial marker system using digital techniques," in *2005 IEEE Computer Society Conference on Computer Vision and Pattern Recognition (CVPR'05)*, IEEE, vol. 2, 2005, pp. 590–596. 18

[72] H. Lim and Y. S. Lee, "Real-time single camera slam using fiducial markers," in *2009 ICCAS-SICE*, IEEE, 2009, pp. 177–182. 18

[73] R. Muñoz-Salinas, M. J. Marın-Jimenez, E. Yeguas-Bolivar, and R. Medina-Carnicer, "Mapping and localization from planar markers," *Pattern Recognition*, vol. 73, pp. 158–171, 2018. 18

[74] A. Sagitov, K. Shabalina, R. Lavrenov, and E. Magid, "Comparing fiducial marker systems in the presence of occlusion," in *2017 International Conference on Mechanical, System and Control Engineering (ICMSC)*, IEEE, 2017, pp. 377–382. 18

[75] A. Sagitov, K. Shabalina, L. Sabirova, H. Li, and E. Magid, "Artag, apriltag and caltag fiducial marker systems: Comparison in a presence of partial marker occlusion and rotation.," in *ICINCO (2)*, 2017, pp. 182–191. 18, 82

[76] T. Petersen, "A comparison of 2d-3d pose estimation methods," *Aalborg University-Institute for Media Technology Computer vision and graphics. Aalborg University*, 2008. 18

[77] T. Tang, M. Zhu, C. Chen, and Y. Xu, "A design of mandibular motion tracking system based on video processing," in *2019 IEEE 4th Advanced Information Technology, Electronic and Automation Control Conference (IAEAC)*, IEEE, vol. 1, 2019, pp. 1370–1374. 18

[78] N. Mostashiri, J. S. Dhupia, A. W. Verl, and W. Xu, "A novel spatial mandibular motion-capture system based on planar fiducial markers," *IEEE Sensors Journal*, vol. 18, no. 24, pp. 10 096–10 104, 2018. 18, 75

[79] G. Zoss, T. Beeler, M. Gross, and D. Bradley, "Accurate markerless jaw tracking for facial performance capture," *ACM Transactions on Graphics (TOG)*, vol. 38, no. 4, pp. 1–8, 2019. 19

[80] W. Yang, N. Marshak, D. Skora, S. Ramalingam, and L. Kavan, "Building anatomically realistic jaw kinematics model from data," *The Visual Computer*, vol. 35, no. 6-8, pp. 1105–1118, 2019. 19

[81] S. Reicha, T. Vollbornb, A. Mehlc, and M. Zimmermannd, "Intraoral optical impression systems–an overview intraorale optische abformsysteme–eine übersicht," *International journal of computerized dentistry*, vol. 16, pp. 143–162, 2013. 20

[82] F. Zhang, C. C. Peck, and A. G. Hannam, "Mass properties of the human mandible," *Journal of biomechanics*, vol. 35, no. 7, pp. 975–978, 2002. 20

[83] S. Benazzi, H. N. Nguyen, O. Kullmer, and K. Kupczik, "Dynamic modelling of tooth deformation using occlusal kinematics and finite element analysis," *PloS one*, vol. 11, no. 3, e0152663, 2016. 22

[84] G. Nagy, "A review of the "pugh" methodology for design concept selection," SAE Technical Paper, Tech. Rep., 1994. 25

[85] E. Marchand, F. Spindler, and F. Chaumette, "Visp for visual servoing: A generic software platform with a wide class of robot control skills," *IEEE Robotics and Automation Magazine*, vol. 12, no. 4, pp. 40–52, Dec. 2005. 26, 45, 82

[86] G. Bradski, "The OpenCV Library," *Dr. Dobb's Journal of Software Tools*, 2000. 26

[87] J. Wang and E. Olson, "AprilTag 2: Efficient and robust fiducial detection," in *Proceedings of the IEEE/RSJ International Conference on Intelligent Robots and Systems (IROS)*, Oct. 2016. 36

[88] A. Trachtenbert, "Computational methods in coding theory," Master's thesis, University of Illinois at Urbana-Champaign, 1996. 37

[89] E. Olson, "Apriltag: A robust and flexible visual fiducial system," in *2011 IEEE International Conference on Robotics and Automation*, IEEE, 2011, pp. 3400–3407. 38

[90] C. Chow and T. Kaneko, "Automatic boundary detection of the left ventricle from cineangiograms," *Computers and biomedical research*, vol. 5, no. 4, pp. 388–410, 1972. 38

[91] T. H. Cormen, C. E. Leiserson, R. L. Rivest, and C. Stein, *Introduction to algorithms*. MIT press, 2009. 38

[92] P. Merriaux, Y. Dupuis, R. Boutteau, P. Vasseur, and X. Savatier, "A study of vicon system positioning performance," *Sensors*, vol. 17, no. 7, p. 1591, 2017. 75

[93] M. O. Mazzetto, M. A. Anacleto, C. A. Rodrigues, R. M. F. Bragança, G. Paiva, and L. Valencise Magri, "Comparison of mandibular movements in tmd by means of a 3d ultrasonic system and digital caliper rule," *CRANIO®*, vol. 35, no. 1, pp. 46–51, 2017. 76

[94] M. Ernst, A. E. Schenkenberger, M. Domin, B. Kordass, and M. Lotze, "Effects of centric mandibular splint therapy on orofacial pain and cerebral activation patterns," *Clinical Oral Investigations*, pp. 1–9, 2019. 76

[95] B. Sagl, M. Schmid-Schwap, E. Piehslinger, M. Kundi, and I. Stavness, "A dynamic jaw model with a finite-element temporomandibular joint," *Frontiers in Physiology*, vol. 10, p. 1156, 2019. 80

[96] I. Stavness, A. G. Hannam, J. E. Lloyd, and S. Fels, "Towards predicting biomechanical consequences of jaw reconstruction," in *Conf Proc IEEE Eng Med Biol Soc*, vol. 2008, 2008, 4567_4570. 80

[97] A. G. Hannam, I. Stavness, J. E. Lloyd, and S. Fels, "A dynamic model of jaw and hyoid biomechanics during chewing," *Journal of Biomechanics*, vol. 41, no. 5, pp. 1069–1076, 2008. 80

[98] G. Constantinescu, K. Kuffel, D. Aalto, W. Hodgetts, and J. Rieger, "Evaluation of an automated swallow-detection algorithm using visual biofeedback in healthy adults and head and neck cancer survivors," *Dysphagia*, vol. 33, no. 3, pp. 345–357, 2018. 81

[99] R. Debon, J. D. Coleone, E. A. Bellei, and A. C. B. De Marchi, "Mobile health applications for chronic diseases: A systematic review of features for lifestyle improvement," *Diabetes & Metabolic Syndrome: Clinical Research & Reviews*, vol. 13, no. 4, pp. 2507–2512, 2019. 81

[100] J.-A. Lee, M. Choi, S. A. Lee, and N. Jiang, "Effective behavioral intervention strategies using mobile health applications for chronic disease management: A systematic review," *BMC medical informatics and decision making*, vol. 18, no. 1, p. 12, 2018. 81

[101] S. Basiratzadeh, E. D. Lemaire, and N. Baddour, "Augmented reality approach for marker-based posture measurement on smartphones," in *2020 42nd Annual International Conference of the IEEE Engineering in Medicine & Biology Society (EMBC)*, IEEE, 2020, pp. 4612–4615. 81

[102] Z. Ahmad, N. Khanna, D. A. Kerr, C. J. Boushey, and E. J. Delp, "A mobile phone user interface for image-based dietary assessment," in *Mobile Devices and Multimedia: Enabling Technologies, Algorithms, and Applications 2014*, International Society for Optics and Photonics, vol. 9030, 2014, p. 903 007. 81

[103] P. Jin, P. Matikainen, and S. S. Srinivasa, "Sensor fusion for fiducial tags: Highly robust pose estimation from single frame rgbd," in *2017 IEEE/RSJ International Conference on Intelligent Robots and Systems (IROS)*, IEEE, 2017, pp. 5770–5776. 82

[104] R. Radkowski and J. Oliver, "A hybrid tracking solution to enhance natural interaction in marker-based augmented reality applications," in *ACHI 2013, The Sixth International Conference on Advances in Computer-Human Interactions*, Citeseer, 2013, pp. 444–453. 83

[105] F. H. Netter, *Atlas of human anatomy, Professional Edition E-Book: including NetterReference. com Access with full downloadable image Bank*. Elsevier Health Sciences, 2014. 119, 120, 126, 127

[106] S. Ingawale and T. Goswami, "Temporomandibular joint: Disorders, treatments, and biomechanics," *Annals of biomedical engineering*, vol. 37, no. 5, pp. 976–996, 2009. 124

[107] M. Gross, "Occlusion in implant dentistry. a review of the literature of prosthetic determinants and current concepts," *Australian dental journal*, vol. 53, S60–S68, 2008. 127

[108] R. A. Sheridan, A. M. Decker, A. B. Plonka, and H.-L. Wang, "The role of occlusion in implant therapy: A comprehensive updated review," *Implant dentistry*, vol. 25, no. 6, pp. 829–838, 2016. 127

[109] U. Posselt, "Movement areas of the mandible," *The Journal of Prosthetic Dentistry*, vol. 7, no. 3, pp. 375–385, 1957. 128

[110] J. N. Palaskar, R. Murali, and S. Bansal, "Centric relation definition: A historical and contemporary prosthodontic perspective," *The Journal of Indian Prosthodontic Society*, vol. 13, no. 3, pp. 149–154, 2013. 128

[111] J. P. Wiens, G. R. Goldstein, M. Andrawis, M. Choi, and J. W. Priebe, "Defining centric relation," *The Journal of prosthetic dentistry*, vol. 120, no. 1, pp. 114–122, 2018. 128

[112] U. Posselt, "Studies in mobility of the human mandible," *Acta. Odontol. Scand.*, vol. 10, pp. 1–160, 1952. 130

[113] S. Mohamed and L. Christensen, "Mandibular reference positions," *Journal of Oral Rehabilitation*, vol. 12, no. 4, pp. 355–367, 1985. 130

[114] J. J. Craig, *Introduction to robotics: mechanics and control, 3/E*. Pearson Education India, 2009. 131, 134

Appendix A

Raw Pose and Angle Error Distribution Results

A.1 Experiment 1

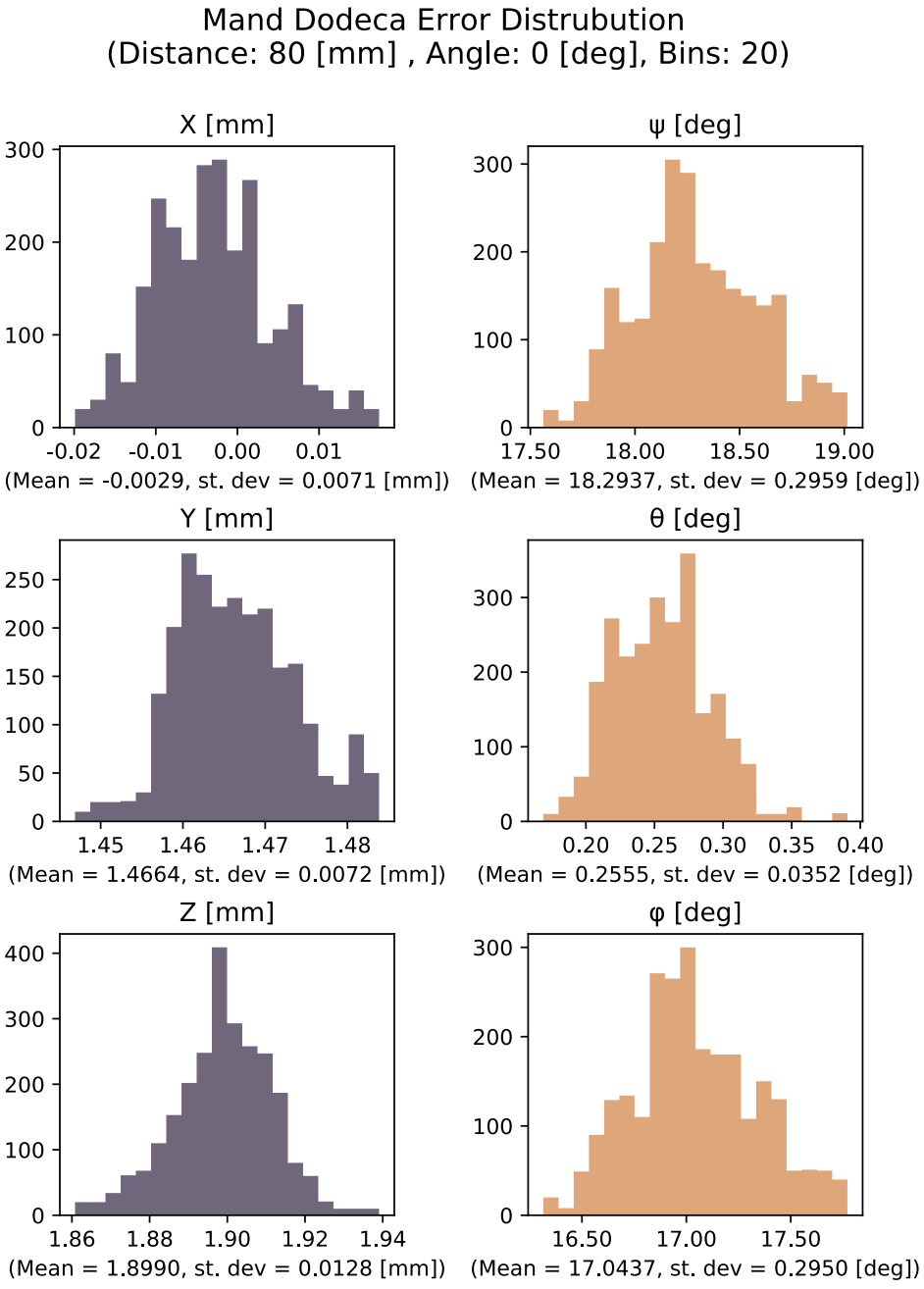

Figure A.1: Pose estimation error distribution at 80mm and 0° (tripod).

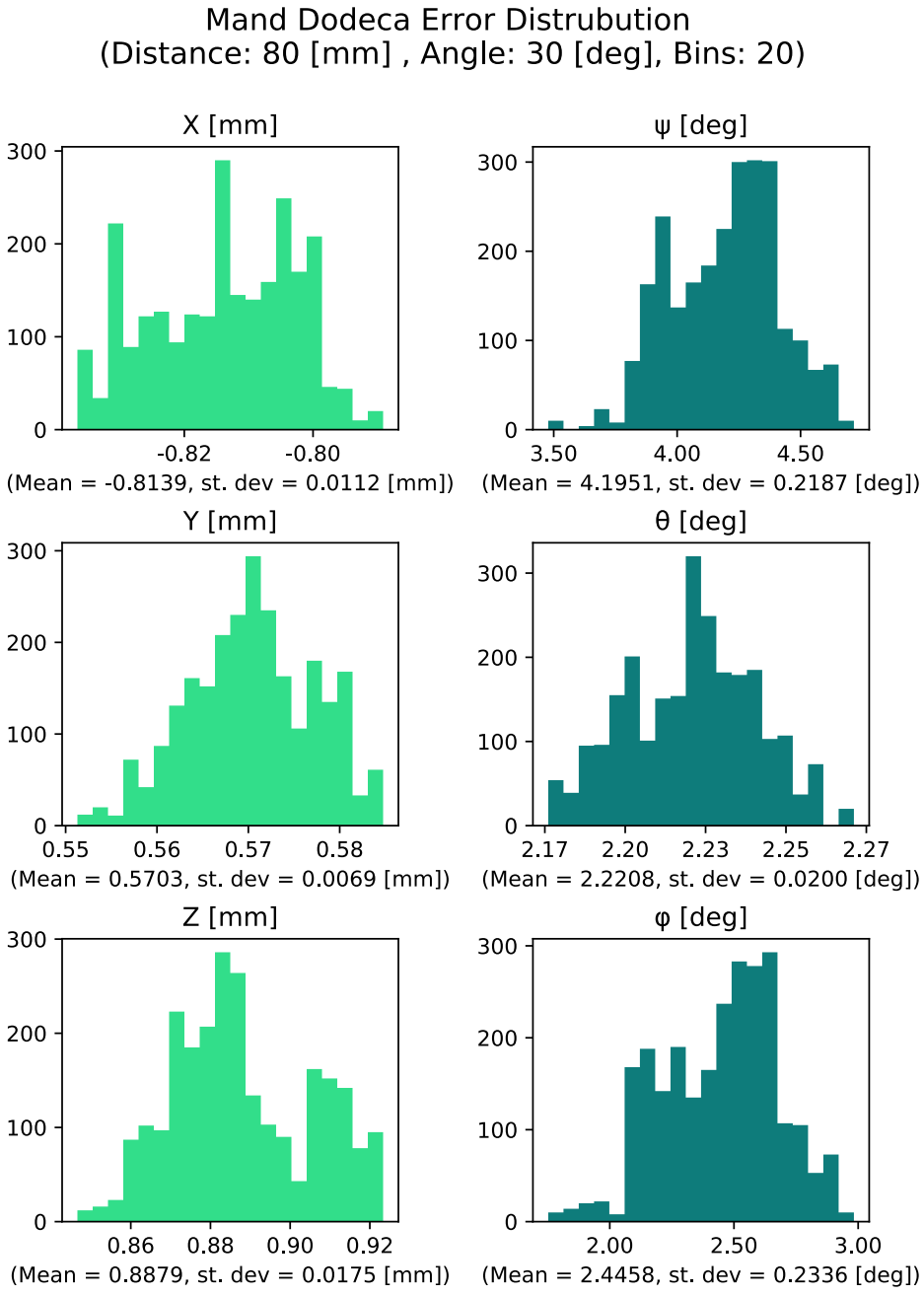

Figure A.2: Pose estimation error distribution at 80mm and 30° (tripod).

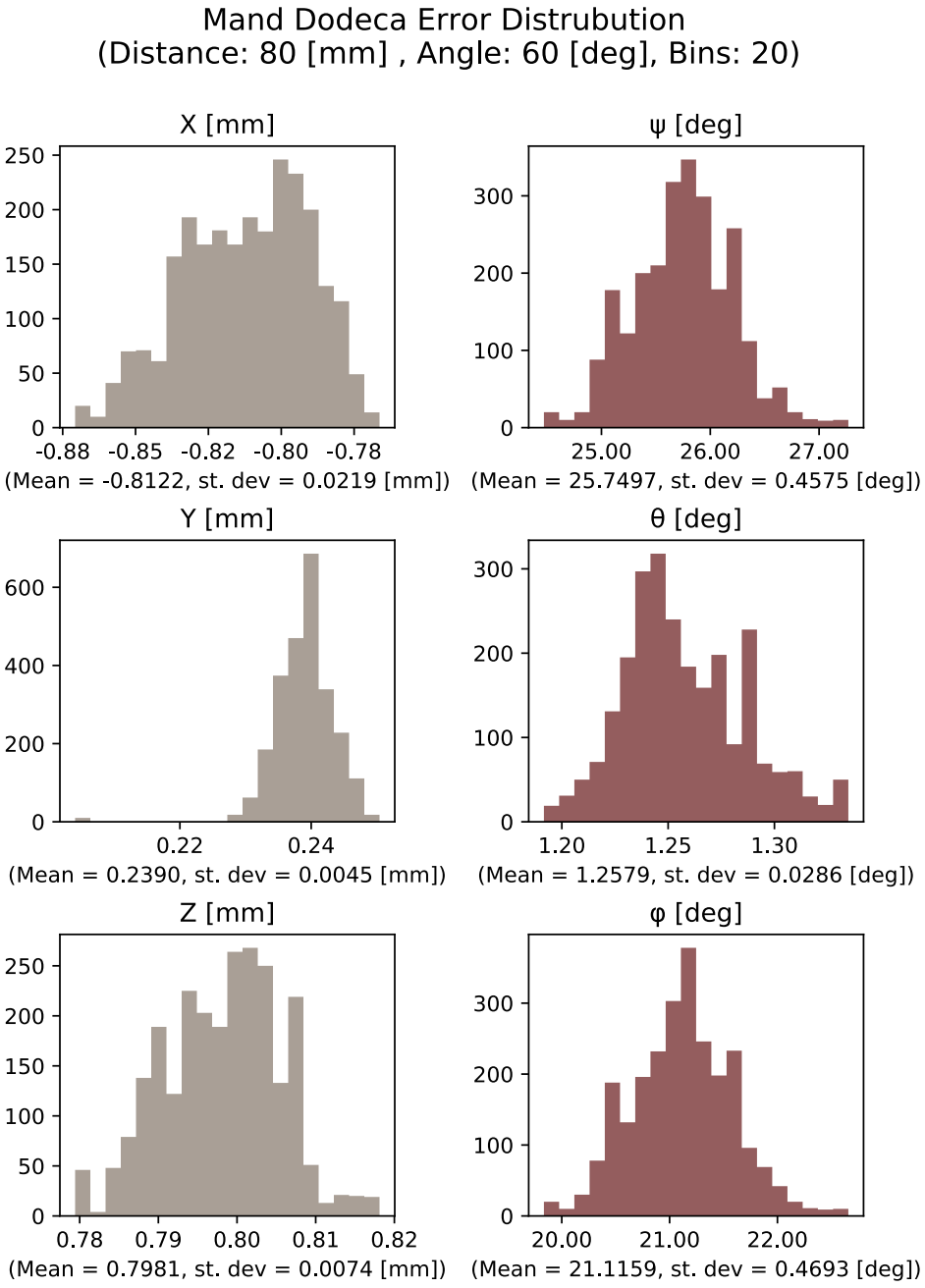

Figure A.3: Pose estimation error distribution at 80mm and 60° (tripod).

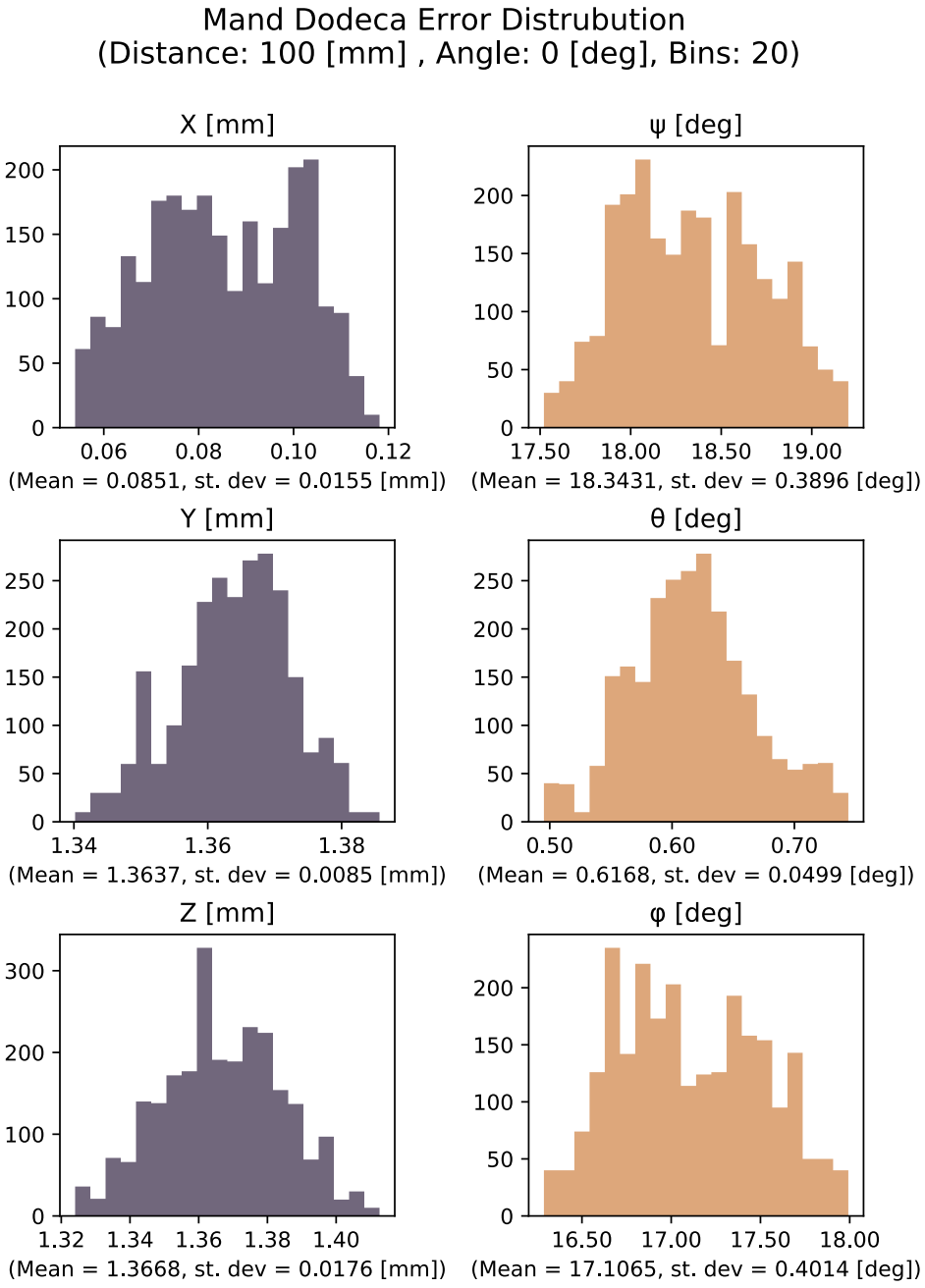

Figure A.4: Pose estimation error distribution at 100mm and 0° (tripod).

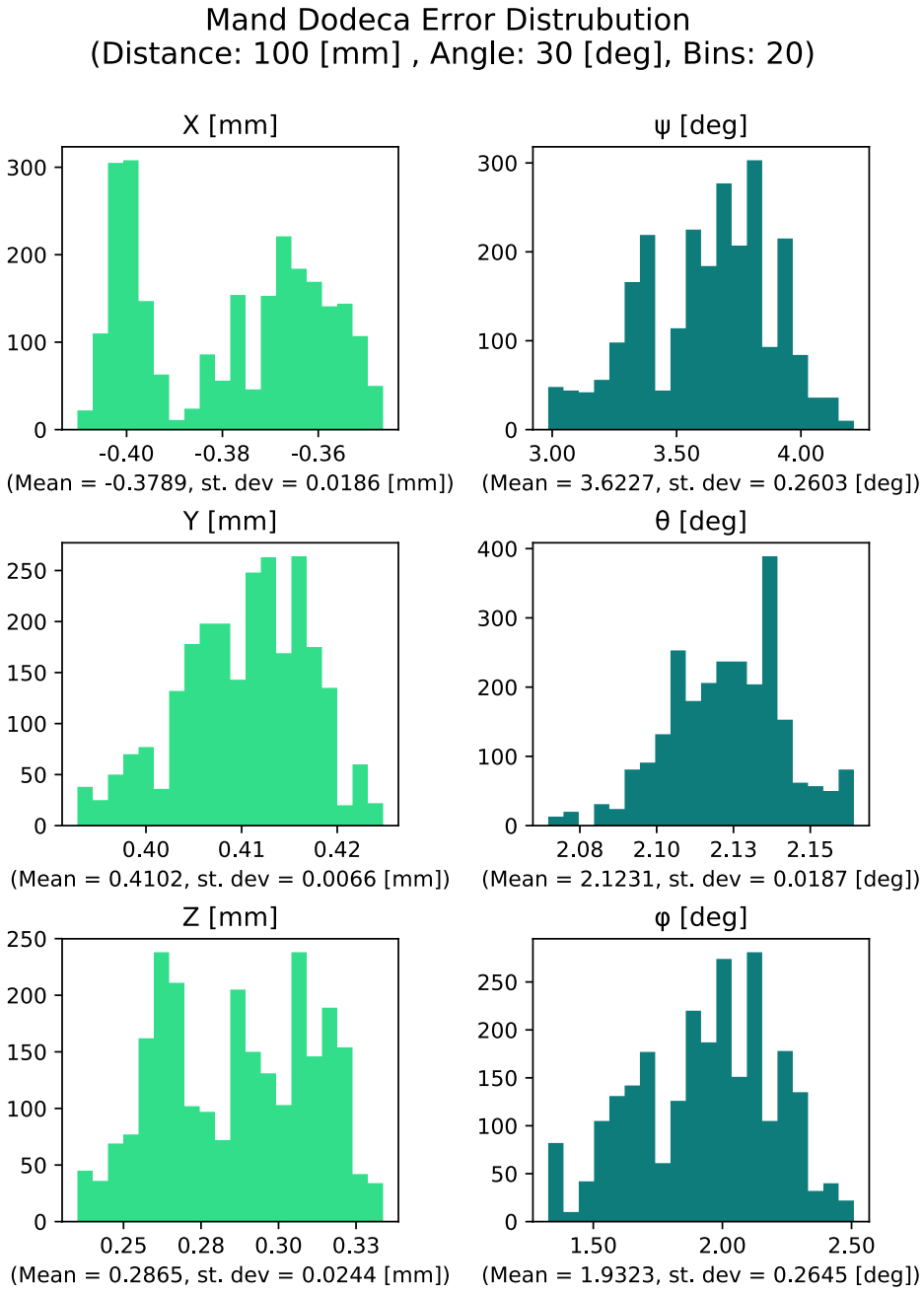

Figure A.5: Pose estimation error distribution at 100mm and 30° (tripod).

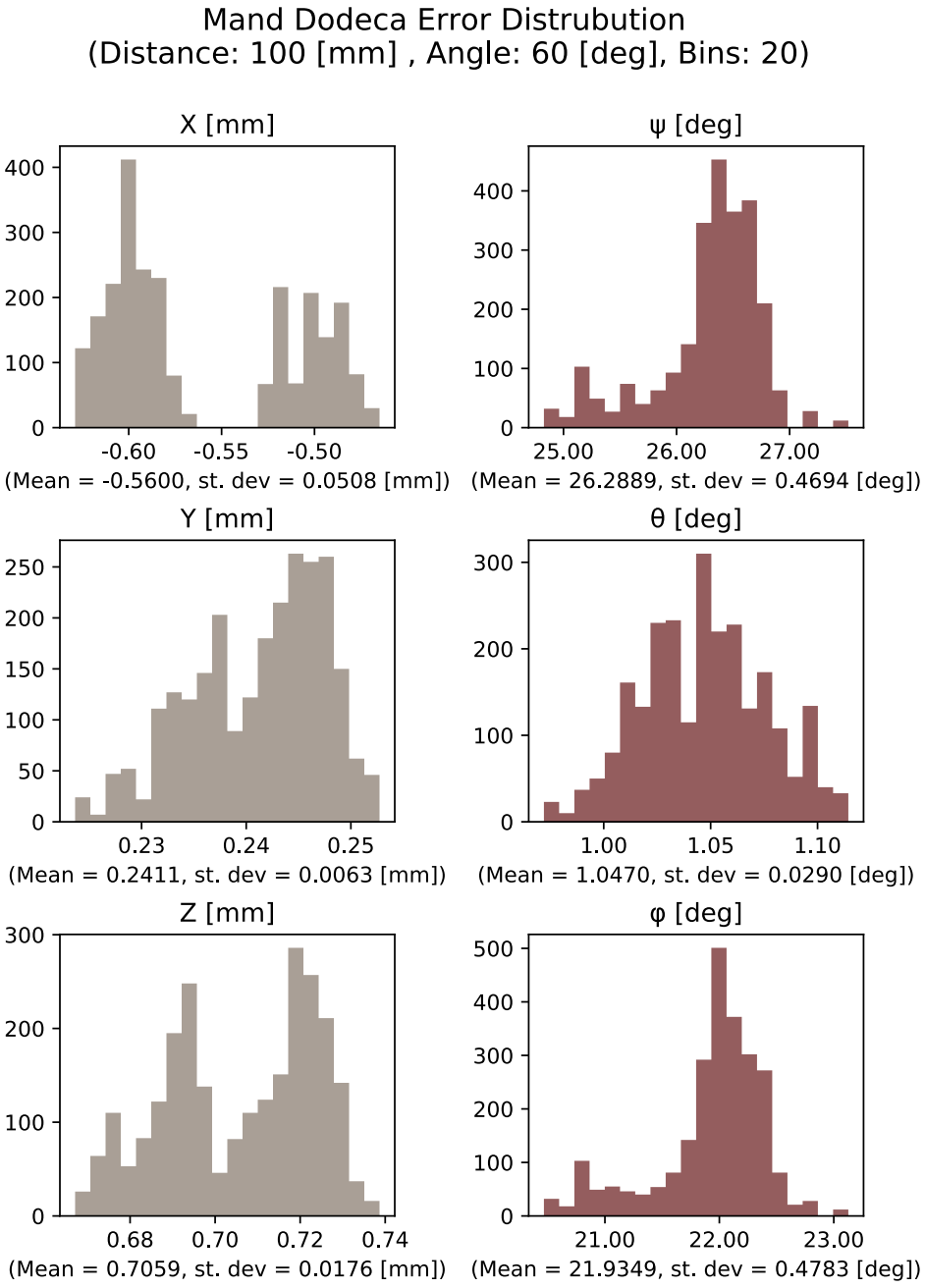

Figure A.6: Pose estimation error distribution at 100mm and 60° (tripod).

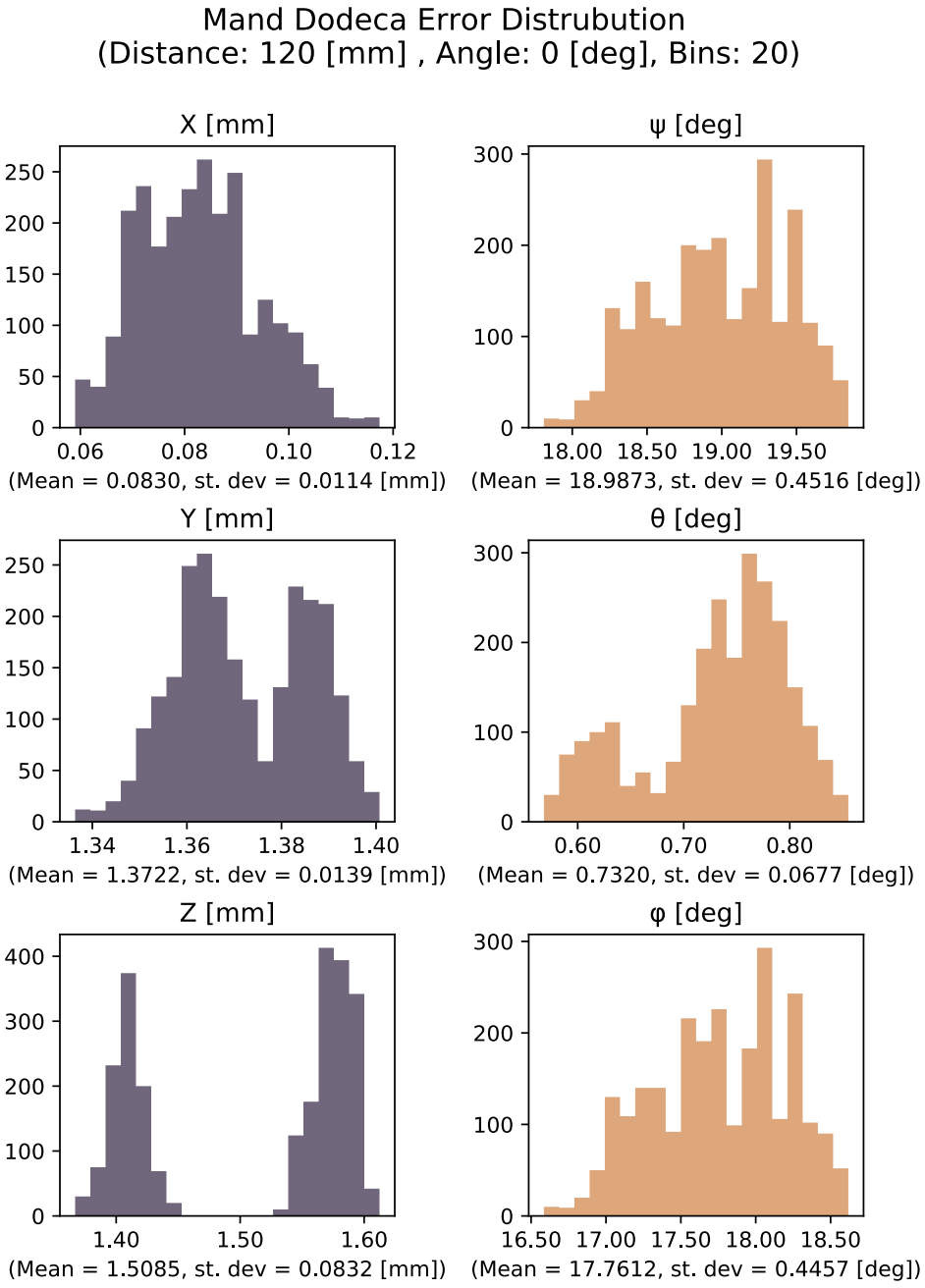

Figure A.7: Pose estimation error distribution at 120mm and 0° (tripod).

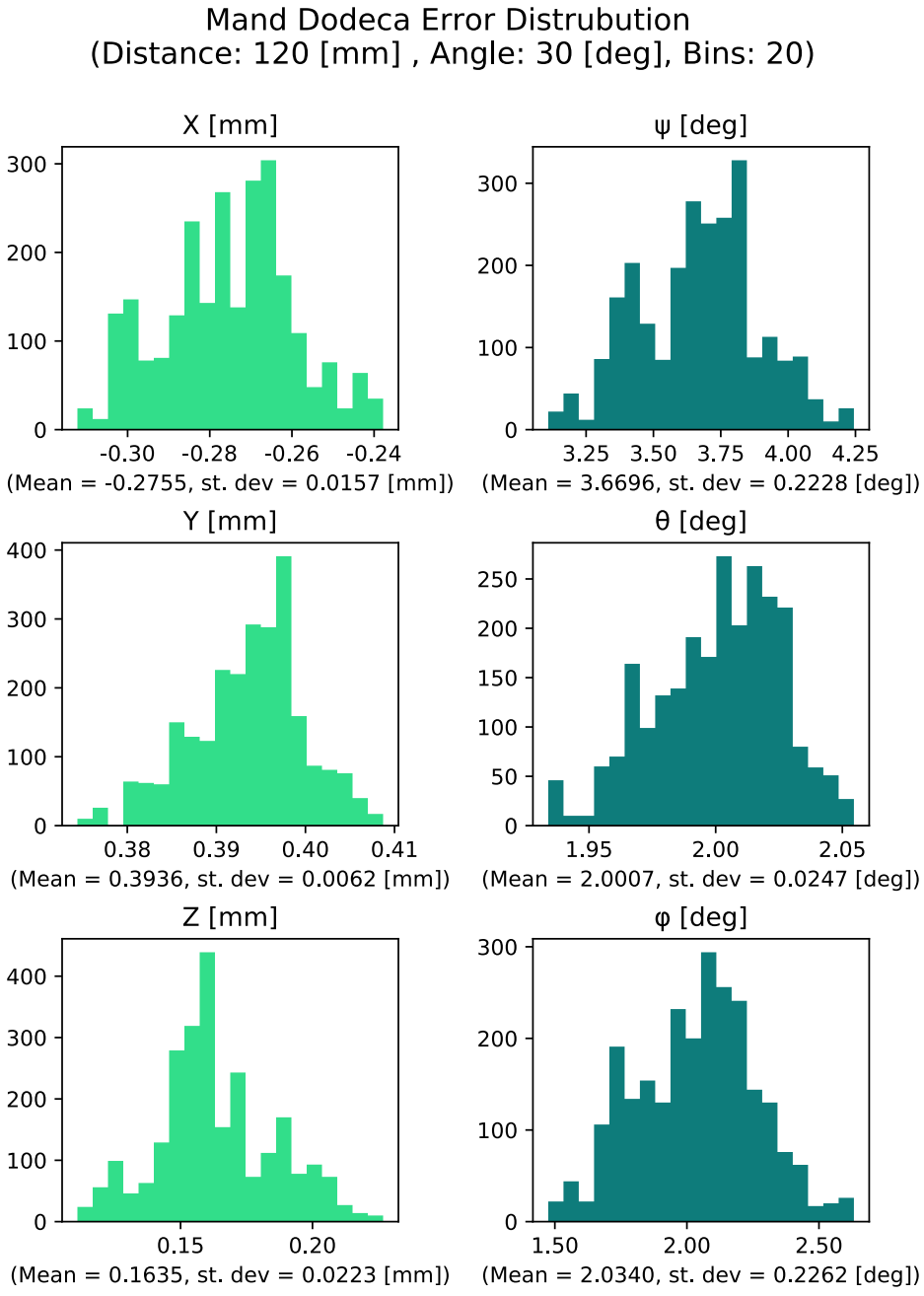

Figure A.8: Pose estimation error distribution at 120mm and 30° (tripod).

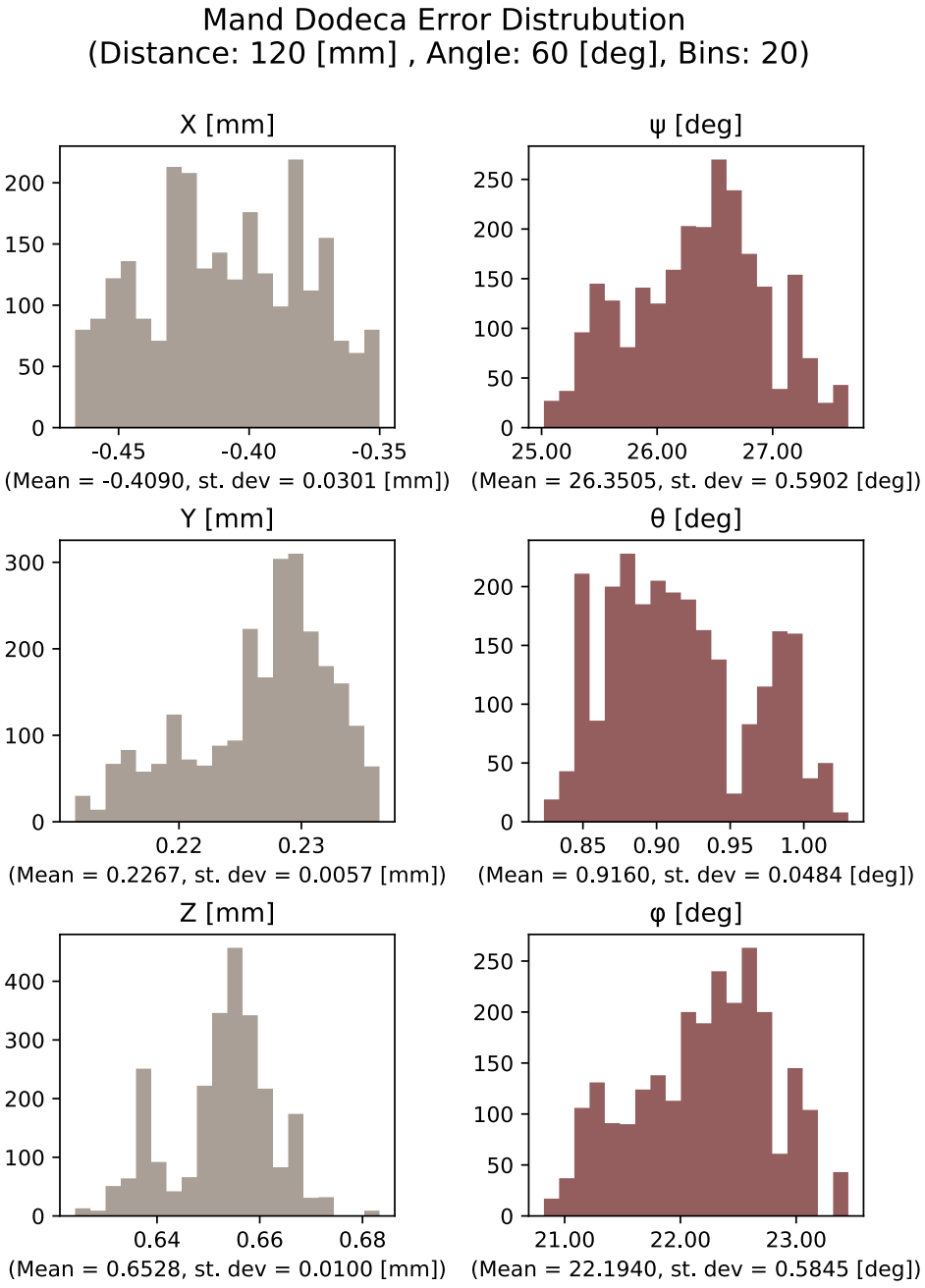

Figure A.9: Pose estimation error distribution at 120mm and 60° (tripod).

A.2 Experiment 2

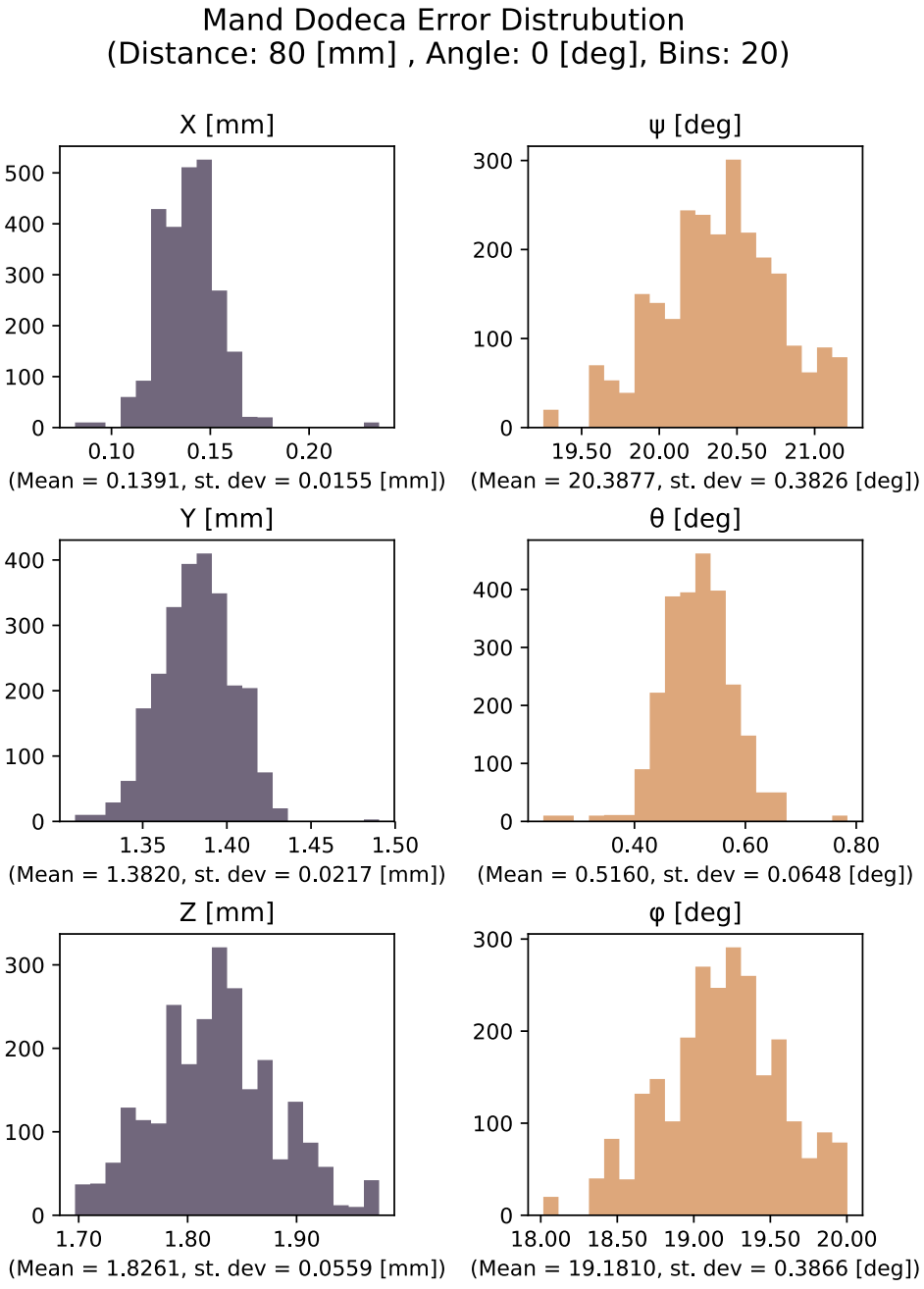

Figure A.10: Pose estimation error distribution at 80mm and 0° (hand).

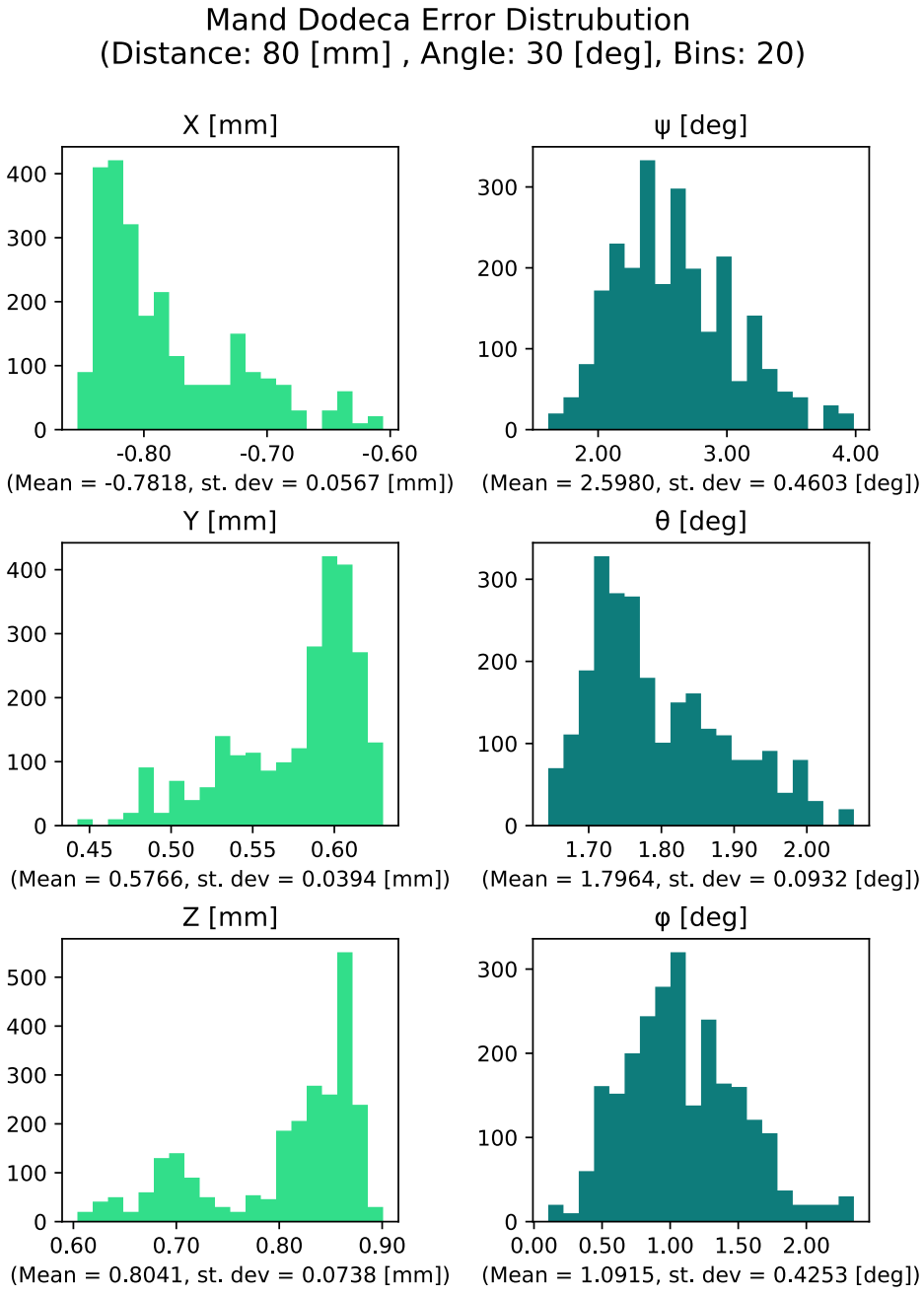

Figure A.11: Pose estimation error distribution at 80mm and 30° (hand).

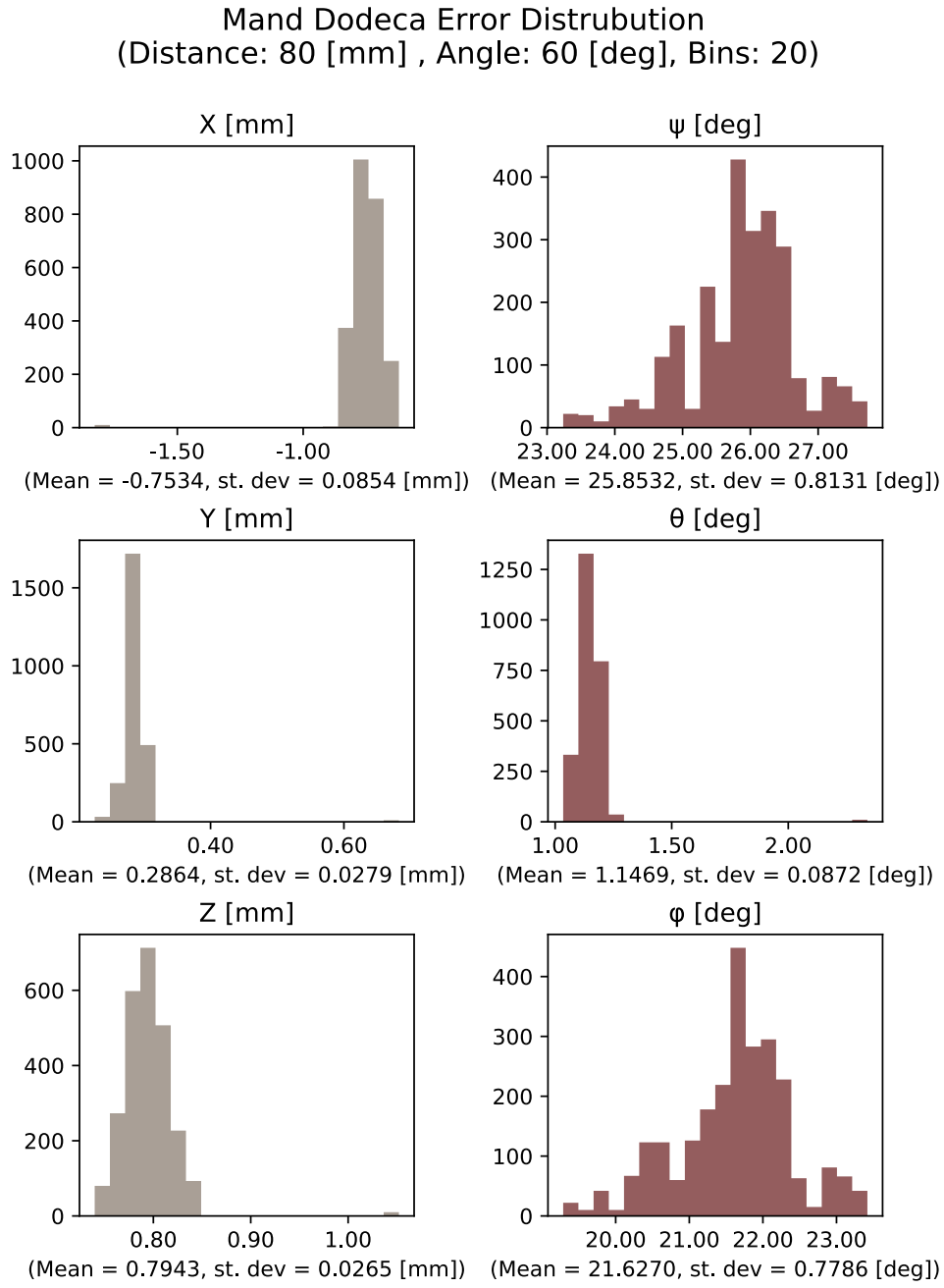

Figure A.12: Pose estimation error distribution at 80mm and 60° (hand).

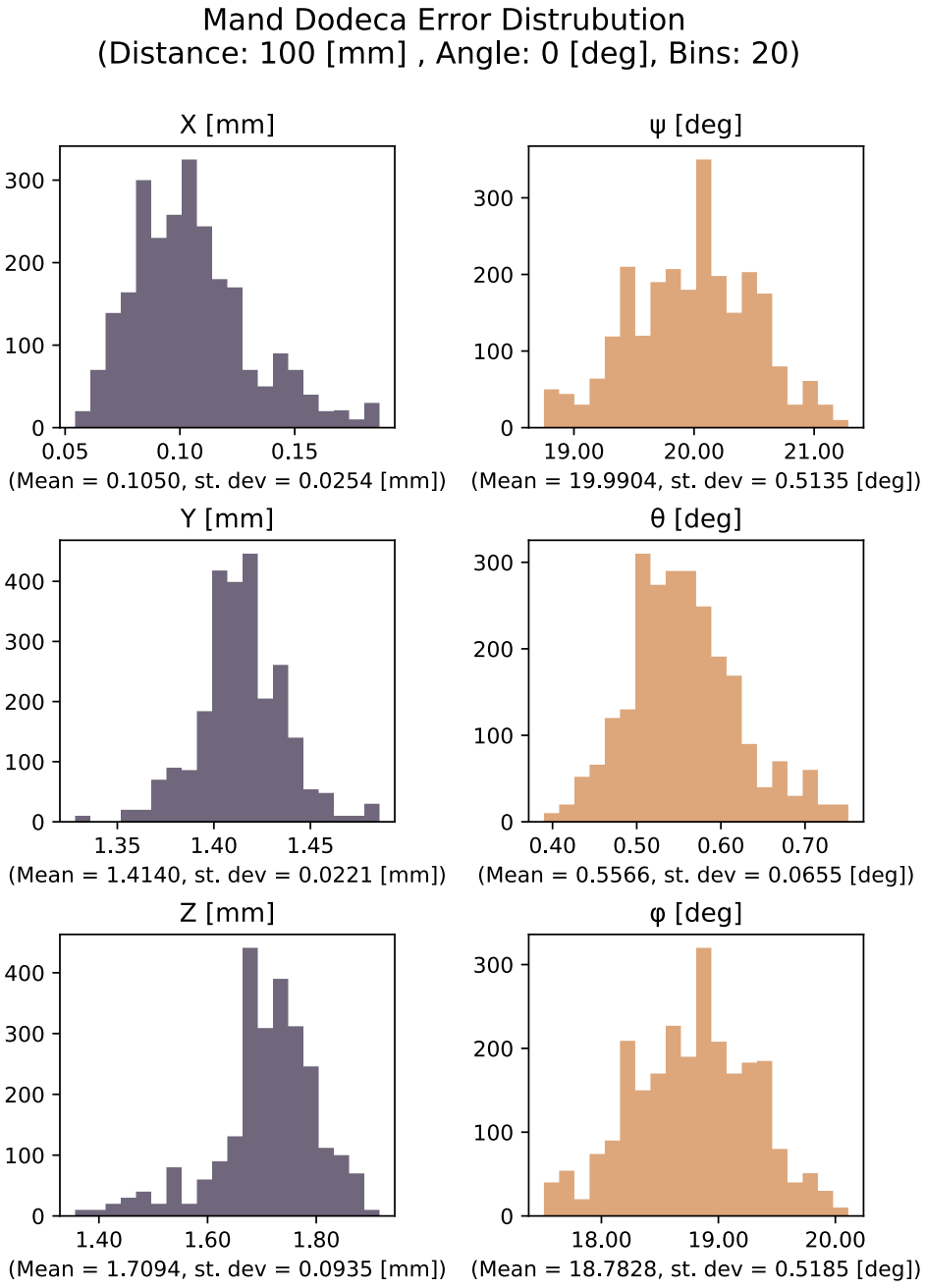

Figure A.13: Pose estimation error distribution at 100mm and 0° (hand).

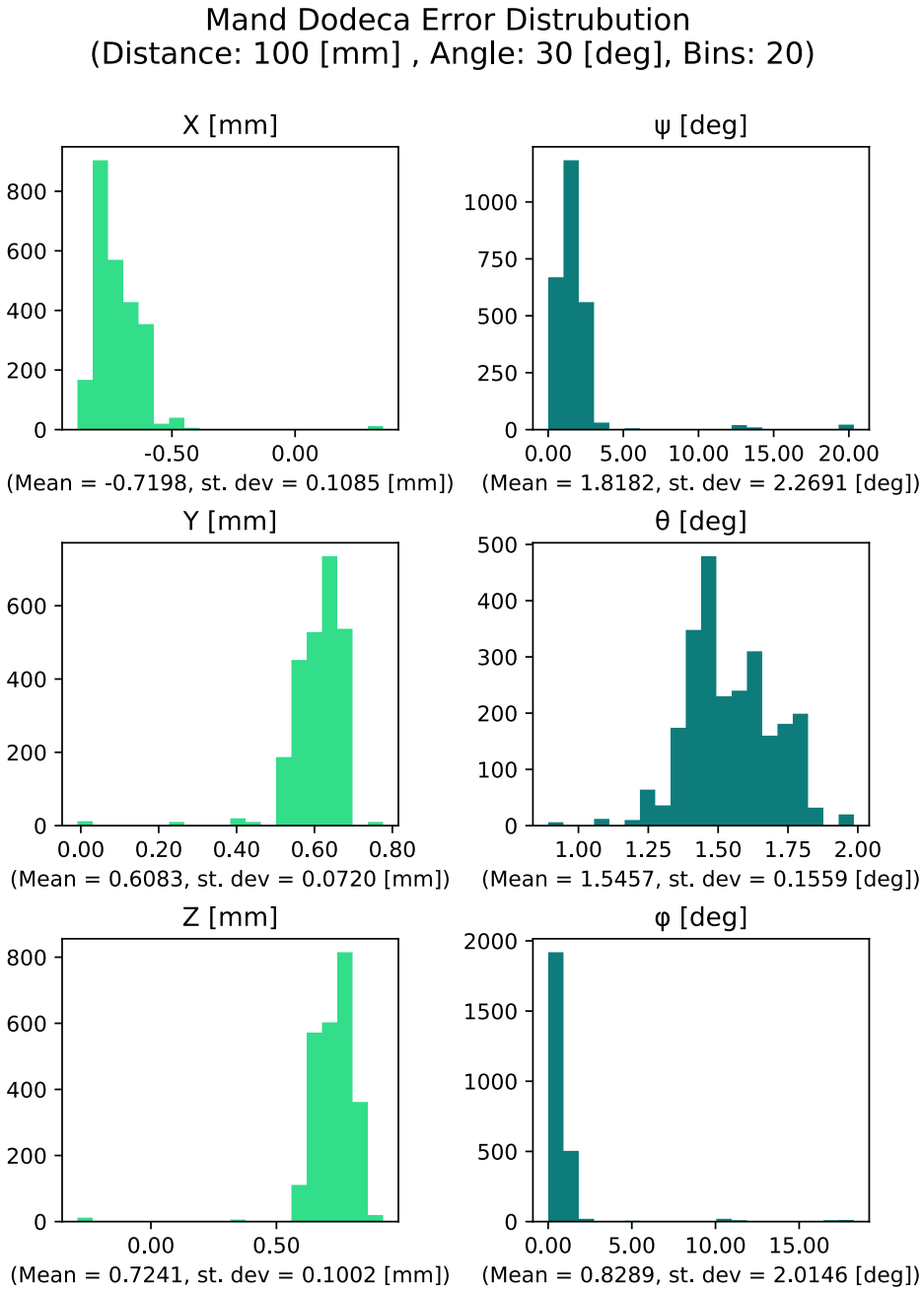

Figure A.14: Pose estimation error distribution at 100mm and 30° (hand).

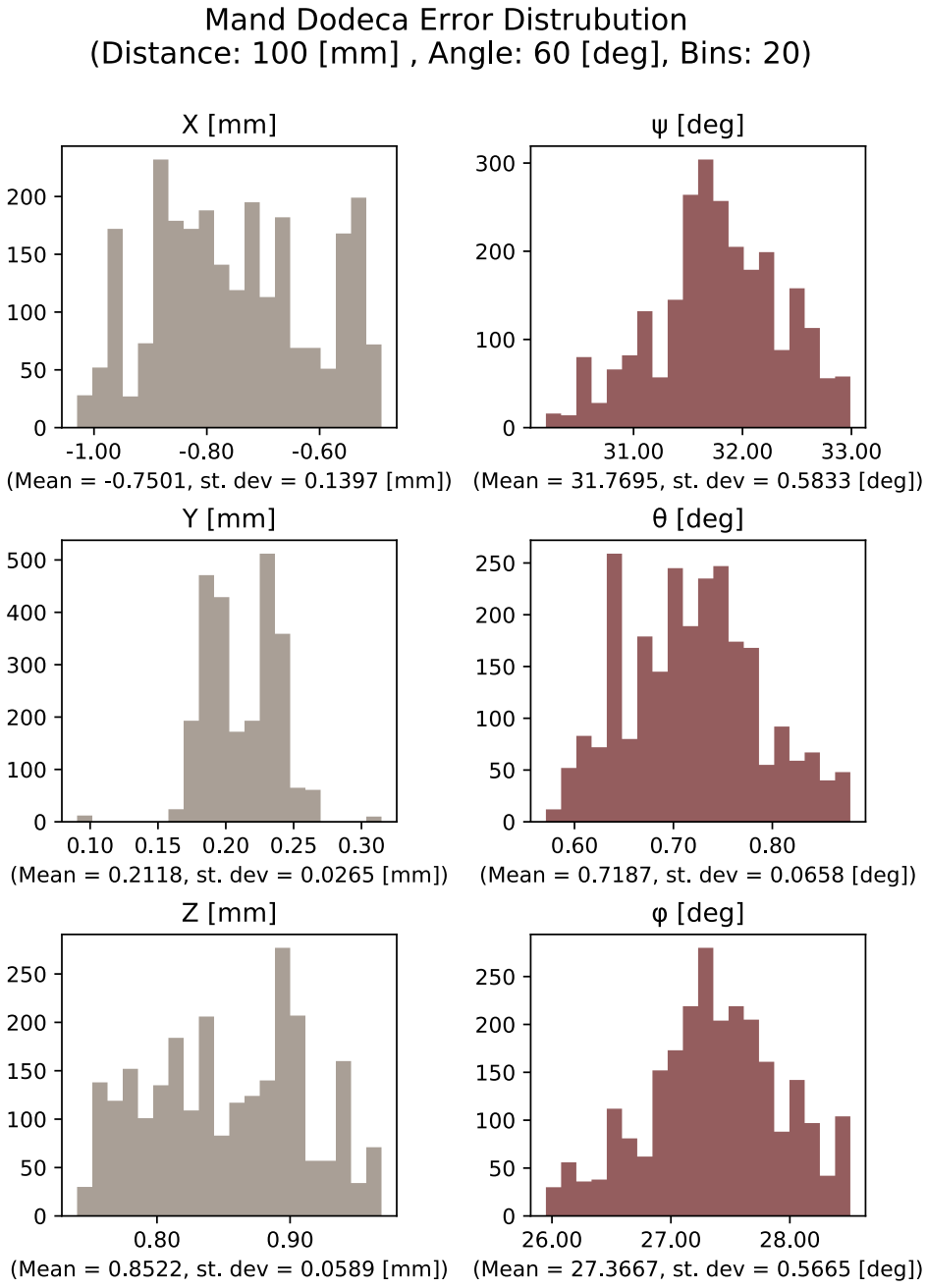

Figure A.15: Pose estimation error distribution at 100mm and 60° (hand).

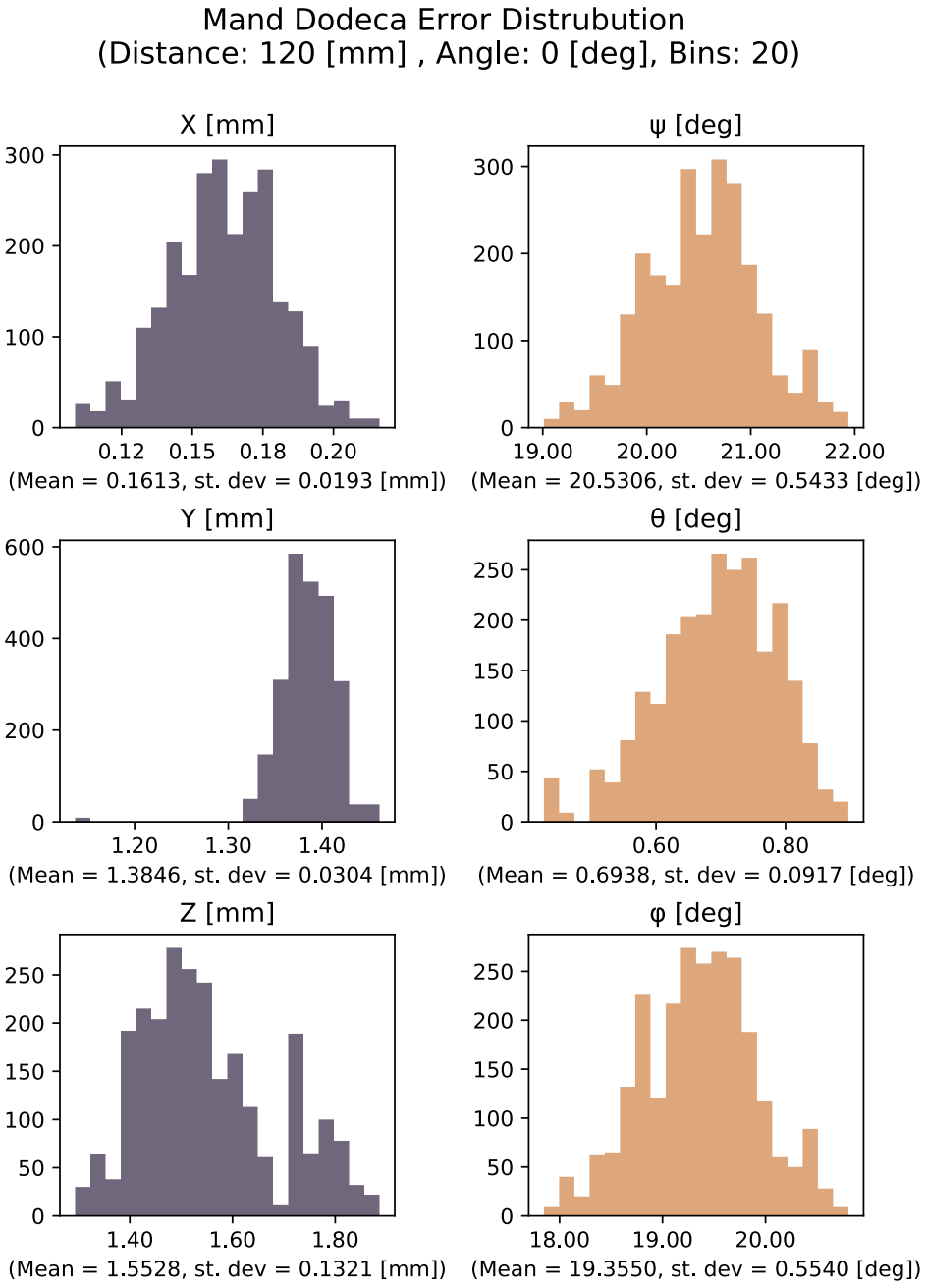

Figure A.16: Pose estimation error distribution at 1200mm and 0° (hand).

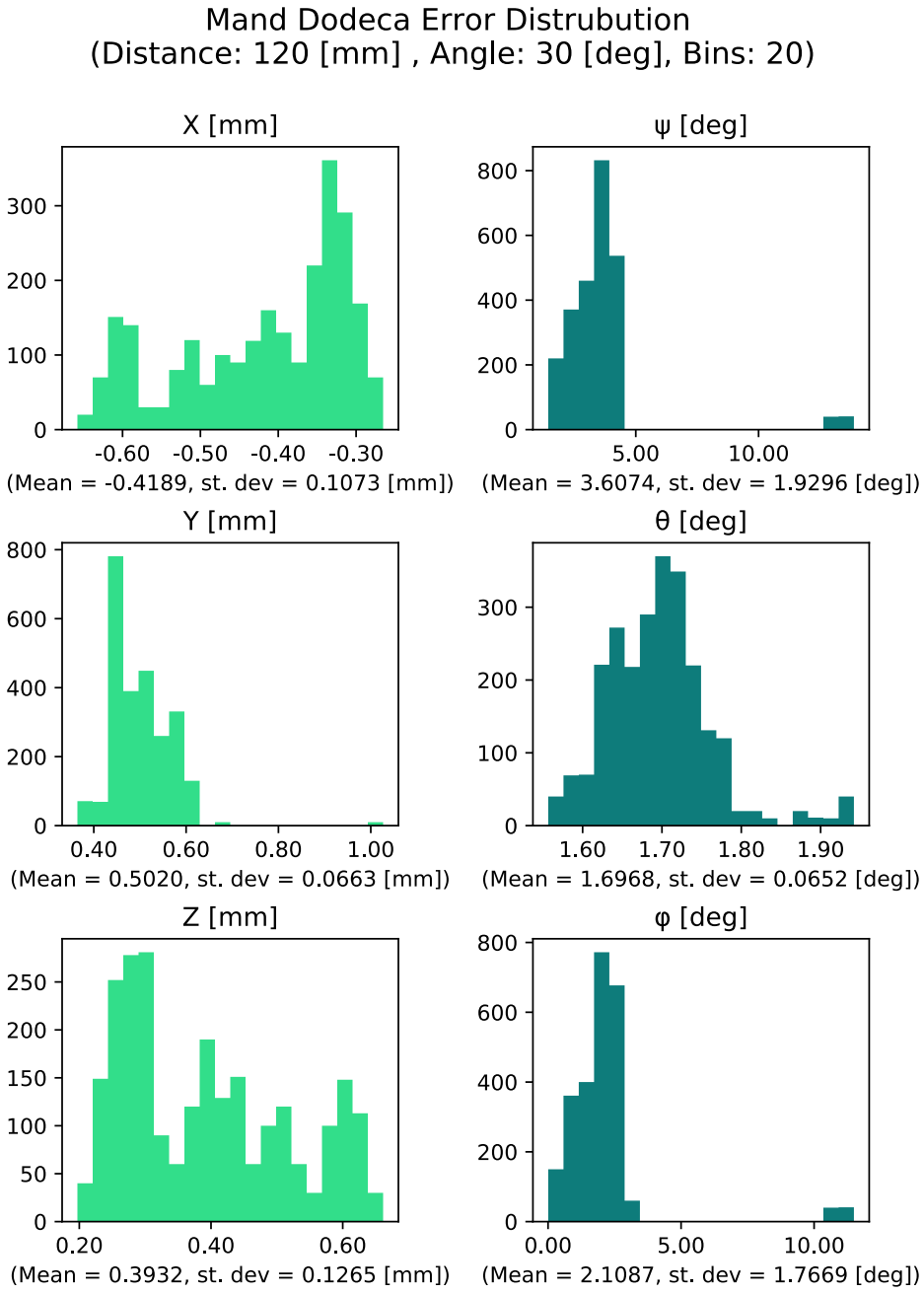

Figure A.17: Pose estimation error distribution at 120mm and 30° (hand).

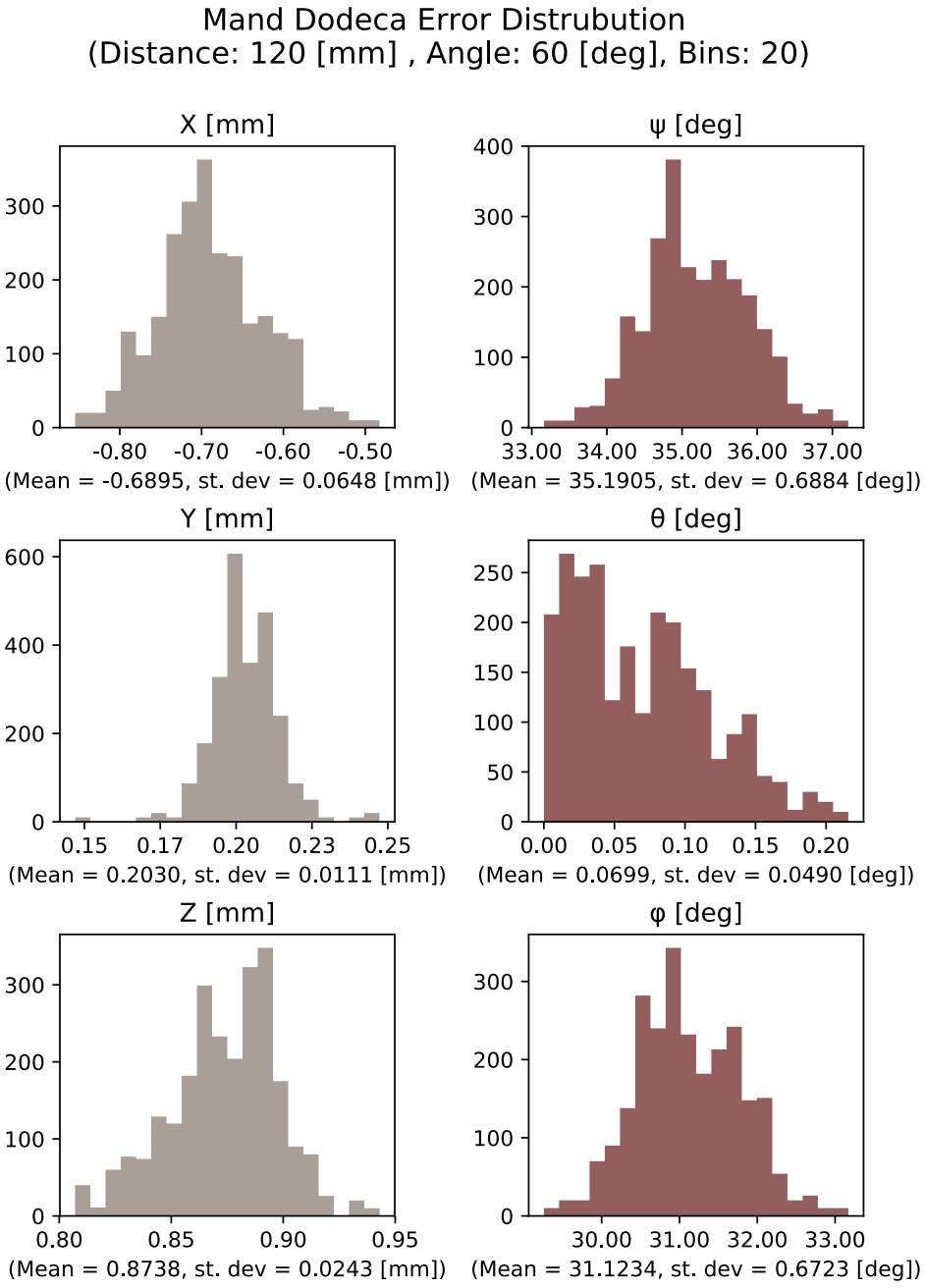

Figure A.18: Pose estimation error distribution at 120mm and 60° (hand).

Appendix B

Relevant Head & Neck Anatomy

This appendix provides an overview of relative head and neck anatomy for the contents of this thesis and we use *Netter: Atlas of Human Anatomy, 5th edition* for reference [105].

B.1 Jaw

In humans, the jaw consists of a pair of bones that define the framework of the oral cavity containing teeth, a movable lower jaw (mandible) and fixed, relative to the skull, upper jaw (maxilla). The jaws function by moving in opposition to one another and are used for biting, chewing, speaking, and swallowing. The lower set of teeth are secured to the mandible and the upper set of teeth are secured to the maxilla via the periodontal ligament.

To move the lower and upper jaw in opposition to one another four muscles groups connect the maxilla and cranium to the mandible. These muscles include; the masseter, temporalis, medial pterygoid, and lateral pterygoid which are grouped in pairs on either side of the skull. They work in combination with each other to move the mandible in the medio-lateral, posterior-anterior, and superior-inferior directions.

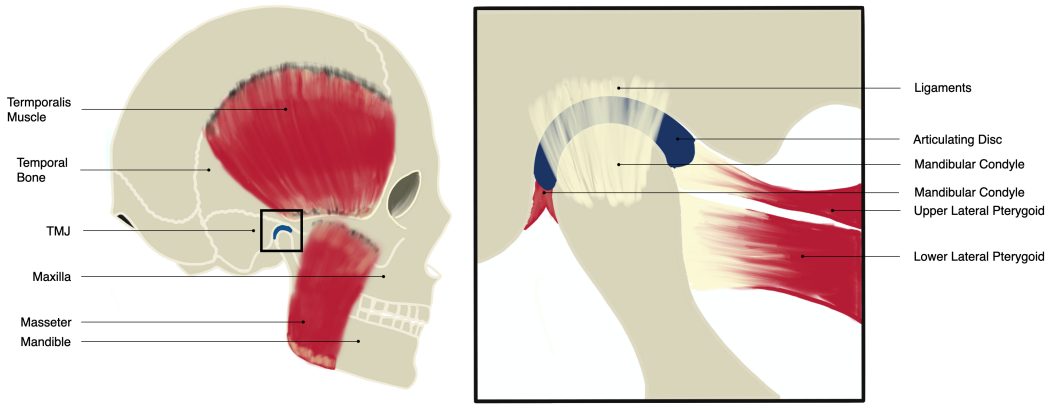

Figure B.1: The mandible articulates with the maxilla through the TMJ. The TMJ is stabilized by a capsule of ligaments and can rotate and translate in 6 DoF once the mandibular condyle leaves the squamous part of the temporal bone. To avoid grinding of bones fibrocartilage articulating disc separates mandibular condyle and squamous part of the temporal bone, it changes shape to accommodate for the sliding nature of the joint. The temporalis, masseter, and pterygoid are of the major muscle groups that move the mandible when contracted and relaxed.

B.2 Hyoid

The hyoid is a U-shaped bone with an anterior body, posterior lesser horns, and greater horns. The hyoid is located at the root of the tongue, anterior to the third cervical vertebra, and between the mandible and the thyroid cartilage of the larynx. The hyoid serves as an attachment point for mastication and tongue muscles. It helps increase the range of the tongue, pharyngeal and laryngeal movements to facilitate speech, chewing, and swallowing.

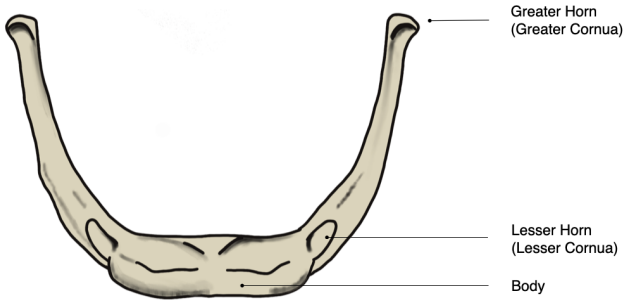

Figure B.2: Hyoid bone anatomy from the anterosuperior view. Adapted from [105].

B.3 Mastication Muscles

The mastication muscles provide the forces required to move the mandible and facilitate chewing. The four major muscles groups are, the masseter, temporalis, medial pterygoid, and lateral pterygoid. The secondary muscles associated with mastication are the geniohyoid, mylohyoid, and the digastricus which is located inferior to the mandible.

The detailed lists of the muscles that follow can be left out since these details are not crucial to the present thesis. Ideally, you should include everything that a computer scientist would need to know about jaw function and mastication to be able to follow the thesis (key concepts and definitions). The images are excellent and communicate the necessary structures.

B.3.1 Primary Mastication Muscles

- **Masseter:** The main masticatory muscle that actuates mandibular elevation, protrusion, and lateral movements. The insertion area is at the inferior border of the anterior part of the zygomatic arch and its origin is on the mandibular ramus.

- **Temporalis:** The temporalis elevates and retrudes the mandible and assists the pterygoid muscle during lateral motions. Its origin is on the inferior temporal line and its insertion on the coronoid process of the mandible.

- **Lateral Pterygoid:** The lateral pterygoid depresses and protrudes the mandible and moves it laterally. It also consists of a superior and inferior head originating from the infratemporal crest on the sphenoid bone and its insertion is on the pterygoid fovea on the condylar neck of the mandible.

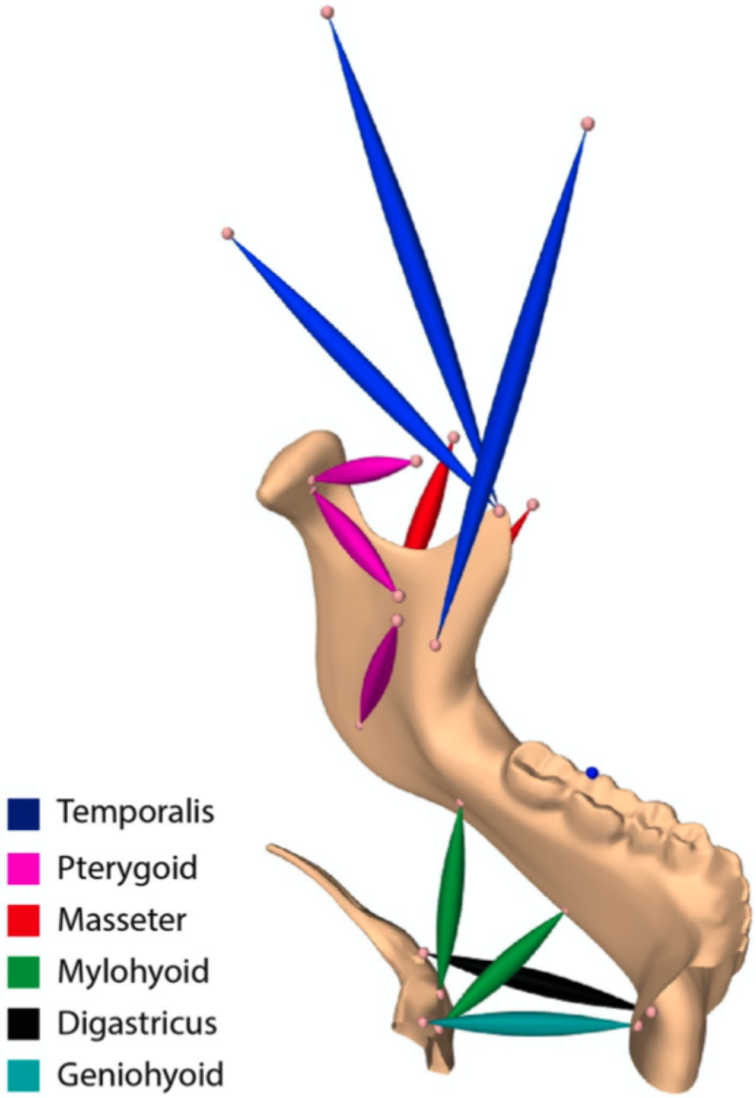

Figure B.3: Point to point representation of mastication muscle anatomy. However, in reality, they are constructed of muscle fibres and surrounded by tissue. The mastication muscles can be separated into jaw elevators and depressors. The jaw depressor group includes the left and right anterior digastricus, geniohyoid, and the superior and inferior mylohyoid. The jaw elevator group includes, the left and right anterior and posterior temporalis, left and right superficial and deep masseter, and left and right medial pterygoid and lateral pterygoid.

- **Medial Pterygoid:** The medial pterygoid elevates, protrudes and actuates lateral excursions of the mandible. This muscle has a deep and superficial head that originates from the medial surface of the pterygoid

plate. Its insertion is on the pterygoid tubercles on the surface of the mandibular ramus.

B.3.2 Secondary Mastication Muscles

- **Geniohyoid:** The geniohyoid is a paired muscle that is part of the suprahyoid muscle group of the neck. It originates on the inferior mental spine and its insertion is on the body of the hyoid bone. Its main function is to control movement on the floor of the oral cavity facilitating swallowing, speech, and mastication.

- **Mylohyoid:** The mylohyoid is also part of the suprahyoid muscle ground. It originates on the mylohyoid line of the mandible and inserts on the mylohyoid raphe on the body of the hyoid. It facilitates speech and deglutition by elevating the floor of the mouth and depressing the mandible.

- **Digastricus:** The digastricus is the other key muscle in the suprahyoid muscle group. It originates from the anterior belly of the fossa on the mandible and the posterior belly of the mastoid notch of the temporal bone. Its insertion is at the body of the hyoid bone. The digastricus depresses the mandible and elevates the hyoid bone during chewing and swallowing.

B.4 Temporomandibular Joint

The TMJ is the joint between the mandible and the temporal bone of the cranium, its function is to articulate motion between the maxilla and the mandible. Each TMJ contains two joint spaces that are separated by fibrocartilage articular discs. The TMJ consists of articulations between the surfaces the mandibular fossa, the squamous part of the temporal bone, and the head of the mandible. The TMJ is a compound joint that is capable of hinge type

and sliding motion making it one of the most complex joints in the human body.

From a biomechanical perspective, the motion of the mandible can be described to take place within the $\mathbb{R}^6$. There are many methods and devices used within restorative dentistry that attempt to represent the TMJ and its complexity [106]. Fundamentally, the ideal goal is to have a patient specific model that includes the spatial relationship between the mandible and the maxilla, the position of the maximum intercuspation between the teeth, and a representative model of occlusal dynamics constrained by their contact and the TMJ. These key aspects help in diagnosis and treatment planning from small crowns to large jaw reconstructions.

B.5 Dentition

The dentition is at the core of human chewing function because its main function is the grind and emulsify food. The upper dental arch is part of the premaxilla while the lower dental arch is which is fused on the midline of the mandible in humans. The shape of the dental arch is generally semi-circular but can vary somewhat from males and females. The upper and lower dentition is usually described by the upper (maxilla) and lower (mandible) quadrants and right and left respectively. In a full dentition, these quadrants house 32 teeth and the teeth are separated by each quadrant into groups of 8. Each group of teeth have a specific function for mastication. There are four different types of teeth, the molars, the incisors, the canines, and the wisdom teeth. Their general function within the mastication system are listed below:

- **Incisors:** There are 8 incisors within the oral cavity and they are located at the anterior part of the mandible and maxilla dentition and are separated at the midline of the mandible. They are used to bite and cut

food that needs to be torn or broken down before it is ground down.

- **Canines:** There are 4 canines in the oral cavity and are the sharpest teeth humans have. There are two on the maxillary arch and two on the mandibular arch. They are used to tear and pierce food apart.

- **Molars:** There are 16 molars in the oral cavity and are separated into premolar and molars. There are 8 on the left and right side of the maxillary and mandibular arch. They are located posterior of the canines and are the most anterior teeth that humans have. The function of the molars is to grind and break down food so that it is small enough to swallow.

- **Wisdom teeth:** Adults can anywhere from 0 to 4 wisdom teeth. They are technically the third type of molar and were used by human ancestors as additional grinding teeth. Typically they erupt in people's teens and twenties and are removed because they create complications within the oral cavity and are not essential for mastication in humans today.

The teeth are composed of four dental tissues, enamel, dentin, cementum, and pulp. The enamel, dentin, and cementum are all hard tissue while the pulp is soft tissue. Enamel cover the tooth and interfaces with food, dentin is the hard tissue underneath the enamel, cementum covers the root, and pulp is the chamber inside the tooth that houses nerves and blood vessels. The periodontal ligament is the sensory information component of the tooth and separates the alveolar bone (jawbone) from the cementum. It supports the teeth, guides tooth eruption, and creates a feedback loop to send force information to the brain so that bite force and mastication can be controlled. This feedback is lost with reconstructive surgery, thus increasing the importance of having well planned restoration that takes into account well distributed forces

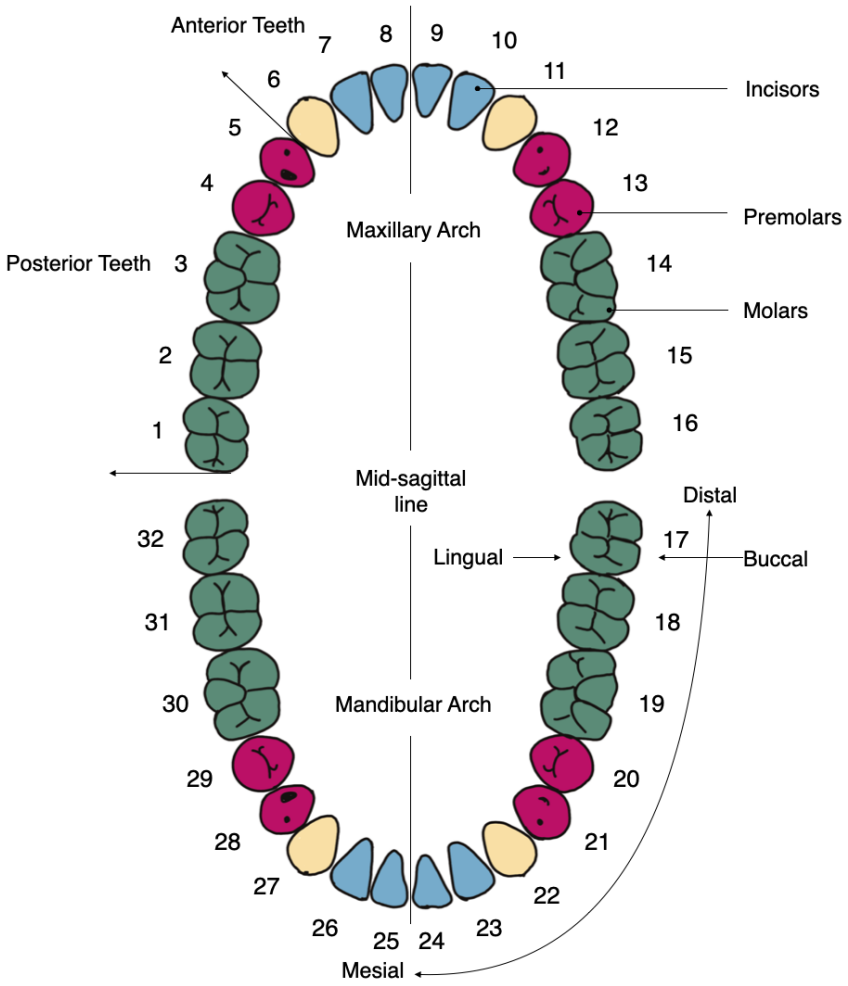

Figure B.4: Occlusal view of a permanent dentition. The upper arch and the lower arch. Adapted from [105].

on a dental prosthesis during mastication to minimize premature prosthetic breakdown.

B.6 Occlusion

Occlusion simply means the contact between the opposing jaws that exists when the teeth are together. The teeth can occlude in many positions, but when the teeth are making the most contact with each other it is referred to as maximum intercuspation. Occlusion is measured at maximum intercuspation when a person is clenching their teeth together. The exact position of

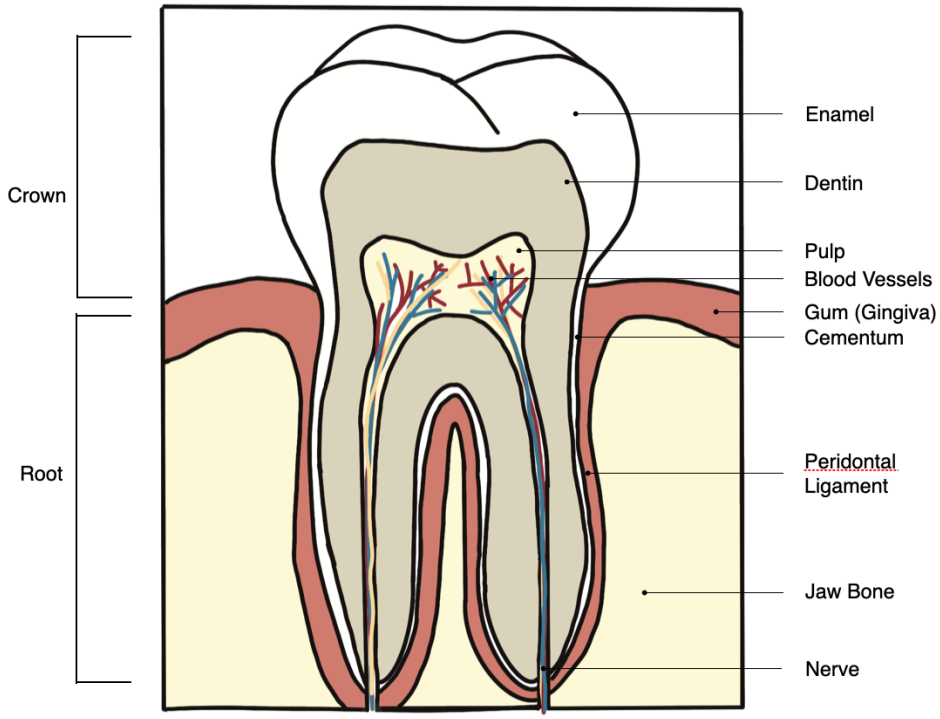

Figure B.5: Molar tooth located within the gingiva and periodontal ligament. Adapted from [105].

maximum intercuspation is different, subjective and specific to a person. This position is important because it defines the spatial relationship between the mandible and the maxilla in the superior-inferior, anterior-posterior and lateral direction. It is the only jaw posture that can be reproduced because it is constrained by the intercuspation of the teeth and is essential for the assessment of mastication and design of a dental prosthesis [107]. In the case of a partial dentition, it becomes more difficult to define this posture and requires the use of a measuring tool, known as a facebow, to record the spatial relationship between the maxilla and the mandible. During mastication, occlusion can be defined as dynamic and the teeth become dampers when they are grinding together. This is the core of mastication and dental prosthesis design [108]. Clinicians recreate this condition to evaluate how the teeth interact when they are moving laterally and in the anterior-posterior direction. They can trace

the contact that the teeth make and investigate how different jaw motions impact the function of chewing.

B.7 Mandibular Kinematics

In this section, we briefly discuss the mandibular motion and use it as a framework to describe mandibular positions and limits. The motion of the mandible is constrained by the TMJ and actuated by the forces that the masticatory muscles apply to the mandible to rotate and translate it. In 1952 Ulf Posselt proposed a method to describe the border movements of the mandible the maxilla called Posselt's envelope of motion. Posselt discovered the movements of the mandible in sagittal and horizontal planes were characteristic of an individual but varied person to person. Regardless, the border movement paths were reproducible for each individual [109] making it a good method to describe mandibular movements. The envelope creates a 3D boundary by tracking the position of the lower ICP. Figure B.6 illustrates the envelope in the sagittal, frontal, and horizontal planes.

The envelope can be characterized regarding the posture and positions defined in Table B.1. The main postural positions of the mandible are centric relation, maximum intercuspation, rest position, and retruded contact position.

- **Centric relation** is controversial in medicine and dentistry today and is an evolving topic. It has become confusing because its definition has changed several times over the past and no consensus has been reached on its definition [110]. However, generally, most agree that it is a spatial relationship, clinically determined between the maxilla and the mandible [111]. The discrepancy in its definition is that most definitions are based on the positioning of the condyles and it is extremely difficult to accu-

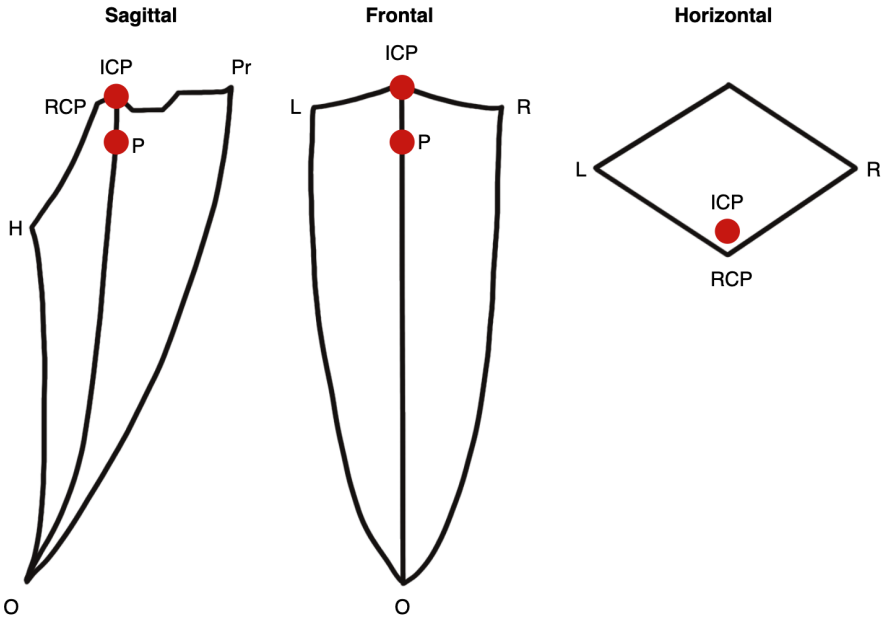

Figure B.6: The sagittal, frontal, and horizontal view of Posselet's envelope of motion.

rately determine their position.

- **Maximum intercuspation** is the jaw posture whereby the teeth of the maxillary and mandibular arch are clenched together and intertwined.

- **Rest position** is the jaw posture that is determined with no muscle activation and the force of gravity. Typically this position creates a 2-3mm space in the incisor canine region.

The mandible is typically capable of opening 50-60mm, moving laterally 10-12mm, protruding 8-10mm, and retruding 1mm. The highest point of the Posselt's envelop in the sagittal plane is maximum ICP. When the mandible is retruded to its maximum position it reaches the RCP which is the most posterior point in the sagittal plane. During the initial phase of opening the mandible purely rotates and opens 20-25mm to point H. As the mandible continues to open to point O it reaches a maximum opening of 50-60mm which is mostly a translational movement. From here, the mandible closes along the

Point acronym	Description
ICP	Intercuspal position
RCP	Retruded contact position
P	Mandible rest position
Pr	Maximum protrusion
H	Maximal mandibular opening with condyle heads in retruded position
L	Maximal mandibular left lateral position
R	Maximal mandibular right lateral position
O	Maximum mandibular opening with complete anterior-inferior translation of condyle heads

Table B.1: Description of the Posselt's mandibular positions and border movements. Adapted from [112][113].

anterior border of Posselt's envelope to its most protruded position (Pr). The mandible protrudes with tooth contact back to the ICP and relaxes at the rest position P.

On the frontal plane at maximum ICP, the teeth maintain occlusal contact and the mandible can move to its maximum left lateral position (L). On opening the mandible moves to point O or maximum opening in the centre. Next, upon closing the mandible moves to a maximum right lateral position (R) and can slide left, back to maximum ICP.

On the horizontal at maximum ICP, the teeth maintain occlusal contact and the mandible can be retruded to maximum RCP. Moving to the right the mandible moves to the maximum right lateral position (R). Moving forward to point Pr the mandible moves forward to its most protrusive position. Moving left to point L the mandible moves to its most left lateral position, and finally can slide back to its maximum ICP.

Appendix C

Position and Orientation Representation

This appendix defines the notation used for rigid body transformation in this thesis and follows the standard notation in Chapter 2 of *Introduction to Robotics: Mechanics and Control, 3/E* [114].

C.1 Description of Position

The description of the position and orientation of a non-deformable rigid body can be contained within the definition of a coordinate reference frame of a more simple frame. Once a coordinate system of frame {A} is established the 3D position of any point can be defined by a 3×1 position vector

$$ {}^{A}\boldsymbol{P} = \begin{bmatrix} P_x \\ P_y \\ P_z \end{bmatrix}. \tag{C.1} $$

The components of this vector are the Cartesian coordinates of the point ${}^{A}\boldsymbol{P}$ w.r.t. to frame {A}. A translation is a displacement, and in the case of a rigid body, a translation represents all points on a body from an initial position to a final position. It should be noted that a rigid body can have points that are not physically attached to it but are defined to be rigidly attached to its coordinate frame, such as the virtual dodecahedrons used in this work. The position of a rigid body can also be defined by a vector ${}^{A}\boldsymbol{P}_{BORG}$ that originates

from another coordinate system {B} and locates the origin of the bodies own origin or frame {A} as illustrated in Figure C.1.

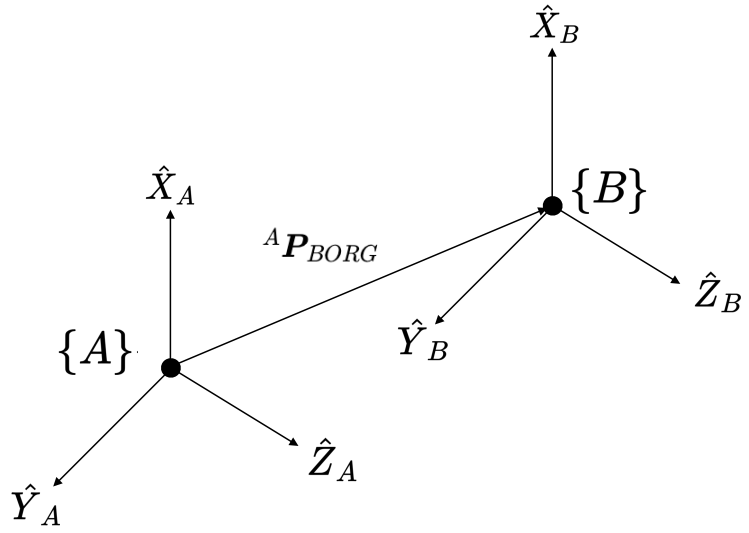

Figure C.1: Locating an object in position and orientation.

C.2 Orientation and Rotation

There are several ways that the orientation and rotation of a rigid body can be expressed. This section defines the 3×3 rotation matrix and the Z-Y-Z Euler angle representation of rigid body orientation.

C.2.1 Rotation Matrices

The orientation of a coordinate frame {B} relative to {A} can be determined by expressing the principle axis unit vector $\left[\hat{\mathbf{X}}_B\ \hat{\mathbf{Y}}_B\ \hat{\mathbf{Z}}_B\right]$ in terms of the basis vector $\left[\hat{\mathbf{X}}_A\ \hat{\mathbf{Y}}_A\ \hat{\mathbf{Z}}_A\right]$ for frame {A}. Multiplying this forms a 3×3 matrix known as the rotation matrix

$$ {}^A_B R = \left[{}^A\hat{\mathbf{X}}_B\ {}^A\hat{\mathbf{Y}}_B\ {}^A\hat{\mathbf{Z}}_B \right] = \begin{bmatrix} \hat{X}_B \cdot \hat{X}_A & \hat{Y}_B \cdot \hat{X}_A & \hat{Z}_B \cdot \hat{X}_A \\ \hat{X}_B \cdot \hat{Y}_A & \hat{Y}_B \cdot \hat{Y}_A & \hat{Z}_B \cdot \hat{Y}_A \\ \hat{X}_B \cdot \hat{Z}_A & \hat{Y}_B \cdot \hat{Z}_A & \hat{Z}_B \cdot \hat{Z}_A \end{bmatrix}. \qquad \text{(C.2)} $$

Since the vectors of each frames principle axis is a unit vector, their dot

product is the cosine of the angle between them and are often referred to as direction cosines. A rotation of frame {A} about the principle axis $\hat{\mathbf{Z}}_B$ through an angle θ is

$$R_Z(\theta) = \begin{bmatrix} \cos\theta & -\sin\theta & 0 \\ \sin\theta & \cos\theta & 0 \\ 0 & 0 & 1 \end{bmatrix}$$

while the same rotation about the $\hat{\mathbf{Y}}_B$ axis is

$$R_Y(\theta) = \begin{bmatrix} \cos\theta & 0 & \sin\theta \\ 0 & 1 & 0 \\ -\sin\theta & 0 & \cos\theta \end{bmatrix}$$

and about the $\hat{\mathbf{X}}_B$ axis is

$$R_X(\theta) = \begin{bmatrix} 1 & 0 & 0 \\ 0 & \cos\theta & -\sin\theta \\ 0 & \sin\theta & \cos\theta \end{bmatrix}$$

The rotation matrix ${}^A_B R$ contains 9 elements, but only 3 parameters are required to define the orientation of a body in space. Since the principle unit vectors of{A} are written in terms of {B} and the description of frame {B} relative to frame {A}, is given by the transpose

$${}^B_A R = {}^A_B R^T. \tag{C.3}$$

This suggests that the inverse of a rotation matrix is equal to its transpose. To verify, the transpose of ${}^A_B R^T$ multiplied by ${}^A_B R$ should equal the identity matrix I_3 and in fact, it does as shown below

$${}^A_B R^T \, {}^A_B R = \begin{bmatrix} {}^A\hat{\mathbf{X}}_B^T \\ {}^A\hat{\mathbf{Y}}_B^T \\ {}^A\hat{\mathbf{Z}}_B^T \end{bmatrix} \begin{bmatrix} {}^A\hat{\mathbf{X}}_B & {}^A\hat{\mathbf{Y}}_B & {}^A\hat{\mathbf{Z}}_B \end{bmatrix} = I_3 \tag{C.4}$$

Therefore,

$${}^A_B R = {}^B_A R^{-1} = {}^B_A R^T. \tag{C.5}$$

C.2.2 Euler Angles

For a minimal representation, the orientation of a coordinate frame {B} relative to {A} can be denoted as a vector of 3 angles $[\phi, \theta, \psi]$. These angles are known as Euler angles where each angle represents a rotation about a principal axis to define a specific orientation. The rotations required to reach an orientation can be achieved with different combinations of rotation matrices. In this work, the Z-Y-Z Euler angle representation is used and other representations such as X-Y-Z and Z-Y-X can be found in Chapter 2 of *Introduction to Robotics: Mechanics and Control, 3/E* [114].

For Z-Y-Z Euler angles the description of frame {B} is assuming that the frames are coincident with {A}, first rotate around $\hat{Z}_B$ about an angle ϕ, followed by a rotation around the current $\hat{Y'}_B$ about an angle θ, and then finally rotate about the current $\hat{Z"}_B$ about an angle ψ. The equivalent rotation matrix is

$$
{}^A_B R_{Z\,Y'\,Z''}(\phi, \theta, \psi) = R_Z(\phi)\; R_{Y''}(\theta)\; R_{Z''}(\psi) \tag{C.6}
$$

$$
= \begin{bmatrix} c_\phi c_\theta c_\psi - s_\phi s_\psi & -c_\phi c_\theta s_\psi - s_\phi c_\psi & c_\phi s_\theta \\ s_\phi c_\theta c_\psi + c_\phi s_\psi & -s_\phi c_\theta s_\psi + c_\phi c_\psi & s_\phi s_\theta \\ -s_\theta c_\psi & s_\theta s_\psi & c_\theta \end{bmatrix}.
$$

To extract the angle vector $[\phi, \theta, \psi]$ from the rotation matrix

$$
{}^A_B R = {}^A_B R_{Z\,Y'\,Z''}(\phi, \theta, \psi) = \begin{bmatrix} r_{11} & r_{12} & r_{13} \\ r_{21} & r_{22} & r_{23} \\ r_{31} & r_{32} & r_{33} \end{bmatrix} \tag{C.7}
$$

if $\sin\theta \neq 0$, it then follows that

$$
\begin{aligned} \theta &= \text{Atan}\,2\left(\sqrt{r_{31}^2 + r_{32}^2}, r_{33}\right) \\ \phi &= \text{Atan}\,2\left(r_{23}/s\theta, r_{13}/s\theta\right) \\ \psi &= \text{Atan}\,2\left(r_{32}/s\theta, -r_{31}/s\theta\right). \end{aligned} \tag{C.8}
$$

In the case where $\theta = 0$ or $180°$, the solution breaks down and only the sum or difference of ϕ and ψ can be computed. One possible convention is to choose

$\phi = 0$ and if $\theta = 0$, then

$$\begin{aligned} \phi &= 0.0 \\ \theta &= 0.0 \\ \psi &= \text{Atan}\,2\left(-r_{12}, r_{11}\right). \end{aligned} \tag{C.9}$$

if $\theta = 180°$, then

$$\begin{aligned} \phi &= 180.0 \\ \theta &= 0.0 \\ \psi &= \text{Atan}\,2\left(r_{12}, -r_{11}\right). \end{aligned} \tag{C.10}$$

C.3 Homogeneous Transformations

To describe the complete position and orientation of rigid body coordinate frame {B} w.r.t. {A}, the 3×3 rotation matrix ${}^{A}_{B}R$ and 3×1 translation vector ${}^{A}\boldsymbol{P}_{BORG}$ into a 4×4 homogeneous transformation matrix

$${}^{A}_{B}T = \left[\begin{array}{ccc|c} & {}^{A}_{B}R & & {}^{A}P_{BORG} \\ \hline 0 & 0 & 0 & 1 \end{array}\right]. \tag{C.11}$$

For this thesis, the 4×4 homogeneous transformation can be regarded as a construction used to compute a rotation and translation of a rigid body with a single matrix form. This compact representation of the rotation and translation is incredibly convenient and is used as an arithmetic tool to compound coordinate frames together.

For example in Figure C.2 we have ${}^{C}P$ and wish to find ${}^{A}P$.

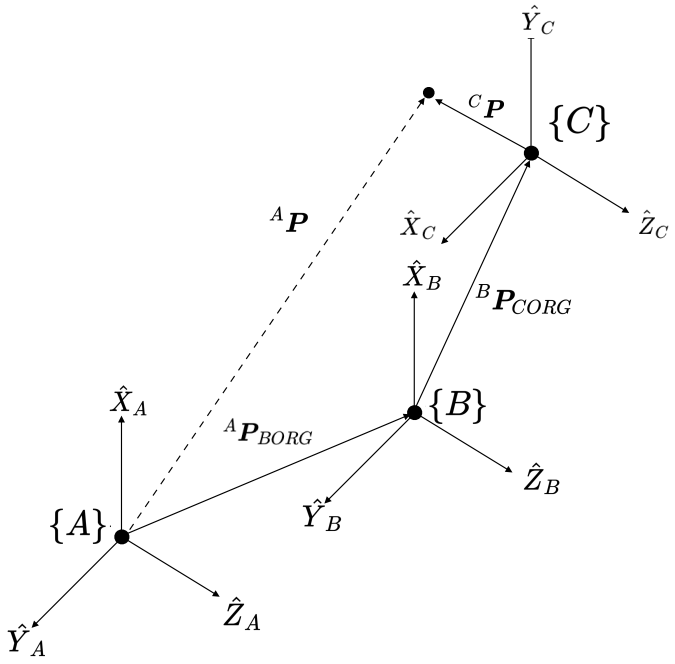

Figure C.2: Compounding frames with the use of the homogenous matrix.

Assuming frame {C}, {B}, and {A} are known relative to one another we can transform ${}^C P$ into frame {A} as,

$$ {}^A P = {}^A_B T \, {}^B_C T \, {}^C P, \tag{C.12}$$

where

$$ {}^A_C T = {}^A_B T \, {}^B_C T. \tag{C.13}$$

Expressed in an homogeneous transformation matrix,

$$ {}^A_C T = \left[\begin{array}{ccc|c} & {}^A_B R \, {}^B_C R & & {}^A_B R \, {}^B P_{CORG} + {}^A P_{BORG} \\ \hline 0 & 0 & 0 & 1 \end{array} \right] \tag{C.14}$$

and

$$ {}^A P = {}^A_C T \, {}^C P. \tag{C.15}$$